

MEDIUM RESOLUTION ATMOSPHERIC PRESSURE IONIZATION  
MASS SPECTROMETERY

Andrew H. Grange  
B.S., Juniata College, 1968

A dissertation submitted to the faculty  
of the Oregon Graduate Center  
in partial fulfillment of the  
requirements for the degree  
Doctor of Philosophy  
in  
Environmental Science and Engineering

February, 1988

The dissertation "Medium Resolution Atmospheric Pressure Ionization Mass Spectrometry" by Andrew H. Grange has been examined and approved by the following Examination Committee:

---

Douglas F. Barofsky, Thesis Advisor  
Professor, Oregon State University

---

Robert J. O'Brien, Thesis Advisor  
Professor, Portland State University

---

James J. Huntzicker, President  
Professor, Oregon Graduate Center

---

David H. Thompson,  
Assistant Professor, Oregon Graduate Center

## Acknowledgements

I thank my advisors, Douglas F. Barofsky and Robert J. O'Brien and Oregon Graduate Center (OGC) for providing me the opportunity and the funding to perform the research described in this dissertation. The problem was interesting, challenging, and practical. I believe use of the instrument described herein will lead to major advances in understanding the chemistry of the atmosphere; this research is not an end, but rather a beginning. I am grateful to both of my advisors for encouraging me to develop a simpler and clearer writing style.

I thank the technical support staff at OGC for their contributions and advice. Specifically: Fred Thone machined the API source body, end plate, and the large Vespel ring which separates them, heli-arc welded the vacuum feedthroughs into the outer flange, and provided advice enabling me to machine the remaining parts; Jerry Boehme modified constant voltage power supplies into constant current supplies and maintained the electronics of the mass spectrometer and flow meters; Dennis Tuuri made purchasing paperwork as easy as possible and ordered supplies promptly; Barbara Ryall drew some of the more complicated figures and provided advice for others; Maureen Sloane provided assistance in the library; and Edie Taylor advised me on proper dissertation format.

I especially thank Lorne Isabelle for his assistance in running the mass spectrometer and its occasionally mysterious software and for making instrument time available when needed.

I appreciate the support and patience of my wife, Maureen Murphy, who asked the question, "When are you going to be done?", less often than expected.

Last, but not least, I thank my parents for financing my undergraduate days and for being tolerant of my unorthodox career path since then.

Table of Contents

Acknowledgements . . . . .	111
Table of Contents . . . . .	v
List of Figures . . . . .	xi
List of Tables . . . . .	xvii
Abstract . . . . .	xviii
Chapter I. A ROLE FOR ATMOSPHERIC PRESSURE IONIZATION MASS . . . . .	1
SPECTROMETRY IN ATMOSPHERIC STUDIES	
I.1. INTRODUCTION . . . . .	1
I.1.a) Developing Models for the Atmosphere . . . . .	1
I.1.b) A Gap in the Photochemical Smog Model . . . . .	1
I.2. LIMITATIONS OF ANALYTICAL TECHNIQUES USED TO STUDY . . . . .	3
ATMOSPHERIC CHEMISTRY	
I.2.a) Analytical Techniques Requiring Sample Concentration . . . . .	3
I.2.b) In Situ Analytical Techniques . . . . .	5
I.3. CRITERIA FOR AN IDEAL ANALYTICAL TECHNIQUE FOR . . . . .	6
ATMOSPHERIC STUDIES	
I.4. ATMOSPHERIC PRESSURE IONIZATION (API) MASS SPECTROMETRY . . . . .	6
I.4.a) Suitability . . . . .	6
I.4.b) Description of API Sources . . . . .	7
I.4.c) Ionization Mechanism . . . . .	9
I.4.d) Coalescing Hydrated and Non-hydrated Analyte Ion . . . . .	11
Peaks	
I.4.e) Interferences . . . . .	12

I.4.f) Resolution Required . . . . .	13
I.5. RESEARCH GOALS . . . . .	14
Chapter II. A MEDIUM RESOLUTION API MASS SPECTROMETER . . . . .	16
II.1. SOURCE DESIGN AND CONSTRUCTION . . . . .	16
II.1.a) Choice of Ionization Method . . . . .	16
II.1.b) Source Block . . . . .	17
II.1.c) Source Support . . . . .	20
II.1.d) Pumping System and Arc Suppression . . . . .	22
II.1.e) Voltage Supplies . . . . .	24
II.2. SOURCE OPERATION AND PERFORMANCE . . . . .	24
II.2.a) General . . . . .	24
II.2.b) Dehydration . . . . .	27
II.2.c) Resolution . . . . .	33
Chapter III. MANIPULATION OF OPERATING CONDITIONS TO SIMPLIFY . . . . .	38
MASS SPECTRA, TO OPTIMIZE SENSITIVITY, AND TO	
DIFFERENTIATE BETWEEN MOLECULAR, HYDRATED, AND	
FRAGMENTED IONS	
III.1. INTRODUCTION . . . . .	38
III.2. EXPERIMENTAL SECTION . . . . .	38
III.2.a) Flow System . . . . .	38
III.2.b) Test Atmospheres . . . . .	41
III.2.c) Determination of the Relative Humidity . . . . .	43
III.2.d) Mass Spectrometer . . . . .	44

III.3.	RESULTS AND DISCUSSION . . . . .	46
III.3.a)	Reproducibility of Mass Spectra . . . . .	46
III.3.b)	Manipulation of the Relative Humidity and the CID Potential . . . . .	47
III.3.c)	Manipulation of the Corona Region Pressure and CID Potential . . . . .	54
III.3.d)	A Contrast Between Toluene and Protonatable Analytes . . . . .	54
III.3.e)	Relative Ion Abundances . . . . .	56
III.3.f)	Hydrated Proton Ion . . . . .	63
III.3.g)	Protonated Molecular Ions . . . . .	65
III.3.h)	Charge Transfer Molecular Ion . . . . .	74
III.3.i)	Fragmented Ion . . . . .	75
III.4.	CONCLUSIONS . . . . .	76
III.4.a)	Oxygenated Analyte Sensitivities . . . . .	76
III.4.b)	Operating Conditions for Studies of Atmospheric Reactions . . . . .	77
Chapter IV.	SUPPRESSION OF SPURIOUS OXIDATION PRODUCTS IN AN ATMOSPHERIC PRESSURE IONIZATION SOURCE . . . . .	79
IV.1.	INTRODUCTION . . . . .	79
IV.2.	EXPERIMENTAL SECTION . . . . .	80
IV.2.a)	Test Atmospheres and Flows . . . . .	80
IV.2.b)	CID Potential and Mass Spectrometer Operation . . . . .	81
IV.3.	RESULTS AND DISCUSSION . . . . .	82
IV.3.a)	Background Mass Spectrum . . . . .	82

IV.3.b)	Mass Spectra Displaying Spurious Products . . . . .	82
IV.3.c)	OH Radical Attack to Produce Spurious Products . . . . .	84
IV.3.d)	Effective Temperature in the Corona Region . . . . .	86
IV.3.e)	Dependence of Spurious Product Yields on the . . . . .	86
	Corona Current	
IV.3.f)	The OH Enriched Region . . . . .	90
IV.3.g)	Necessity for API Source Chemistry Suppression . . . . .	94
IV.3.h)	OH Scavenger Gas Addition . . . . .	95
IV.3.i)	Appearance of True Photooxidation Products from . . . . .	98
	Toluene	
IV.C.j)	Alternate Flow Path for Neutral Species . . . . .	99
IV.3.k)	Chemical Noise Suppression . . . . .	99
IV.3.l)	Photooxidation Products from Toluene with . . . . .	102
	Alternate Flow	
IV.4.	CONCLUSIONS . . . . .	104
Chapter V.	DETECTION LIMIT AND DYNAMIC RANGE DETERMINATIONS . . . . .	106
V.1.	INTRODUCTION . . . . .	106
V.2.	EXPERIMENTAL SECTION . . . . .	106
V.2.a)	Benzaldehyde Addition . . . . .	106
V.2.b)	Mass Spectrometer Operation . . . . .	107
V.3.	RESULTS AND DISCUSSION . . . . .	108
V.3.a)	Response Curve and Detection Limit . . . . .	108
V.3.b)	Xylene Interference . . . . .	110
V.3.c)	Adsorption . . . . .	112
V.3.d)	Operational Solution to Limited Dynamic Range . . . . .	113



V.3.e)	Source Modifications to Increase Dynamic Range . .	114
V.3.f)	Standard Addition . . . . .	116
V.3.g)	Optimal Toluene Concentration . . . . .	117
VI.4.	CONCLUSIONS . . . . .	118
Chapter.VI.	APPLICATION OF MEDIUM RESOLUTION APIMS TO TOLUENE . .	119
PHOTOOXIDATION STUDIES		
VI.1.	INTRODUCTION . . . . .	119
VI.2.	EXPERIMENTAL SECTION . . . . .	120
VI.2.a)	Test Atmosphere and Sample Gas . . . . .	120
VI.2.b)	Mass Spectrometer Operation . . . . .	121
VI.3.	RESULTS AND DISCUSSION . . . . .	124
VI.3.a)	Toluene Photooxidation Products Found in Past . .	124
Studies		
VI.3.b)	Medium Resolution API Mass Spectra of Toluene . .	125
Photooxidation Products		
VI.3.c)	Desorption vs Product Generation . . . . .	129
VI.3.d)	Peak Separation in Kinetic Studies . . . . .	129
VI.3.e)	Identification of Hydrated Ions . . . . .	130
VI.3.f)	Peak Separation in Daughter Ion Studies . . . . .	133
VI.3.g)	Deuterated toluene . . . . .	134
VI.3.h)	Other Possible Product Peaks . . . . .	135
VI.3.i)	Products Not Detected . . . . .	135
VI.3.j)	Adsorption . . . . .	138
VI.3.k)	Differentiating Classes of Photooxidation . . . .	139
Products		

Chapter VII. CONCLUSIONS . . . . .	140
Appendix A. DISCHARGE SUPPRESSION SYSTEM . . . . .	144
Appendix B. DILUTION CORRECTION CALCULATION . . . . .	150
Appendix C. COMMENTS ON THE VOLUME OF AND REACTIONS WITHIN THE . .	152
OH ENRICHED REGION	
C.1. Before Addition of Scavenger Gas . . . . .	152
C.2. After Addition of CO . . . . .	159
C.3. After Enhancement of the Flow . . . . .	162
Appendix D. CALCULATION OF THE BENZALDEHYDE CONCENTRATION . . . . .	167
EXPECTED IN THE RESERVOIR	
AFTER 23.2 HRS OF IRRADIATION	
Bibliography . . . . .	169
Vitae . . . . .	175
Curriculum Vitae . . . . .	177

## List of Figures

- FIGURE I.1. Schematic diagram of an Atmospheric Pressure Ionization source showing the ionization region where ions are produced by either a beta particle emitting foil or a corona discharge. The direction of ion travel through the differentially pumped region into the mass analyzer is noted, as are the approximate pressures in each of the three regions. 8
- FIGURE II.1. Construction details of the API source (non-uniplanar cross section). 18
- FIGURE II.2. Photograph of the API source and the support assembly used to adapt it to the VG 7070E-HF mass spectrometer. 21
- FIGURE II.3. Construction details of the assembly used to isolate the conducting gas exposed to the high source potential from grounded surfaces within the source housing of the mass spectrometer. 23
- FIGURE II.4. Mass spectra for room air at  $40 \pm 15\%$  relative humidity. For the spectrum in a) the CID pressure was 0.4 Torr and the CID potential was 19 V; in b) the CID pressure was 1 Torr and the CID potential was 19 V; and in c) the CID pressure was 1 Torr and the CID potential was 55 V. The peak at  $m/z$  149 is due to protonated phthalic anhydride, a fragmented ion produced from phthalates, which are common components of plasticizers (46). 29
- FIGURE II.5. Ion abundance plots of the first five hydrated protons as a function of CID potential with a CID pressure of 1 Torr. Ion abundances are corrected for ion collection efficiency and normalized to the abundance of the  $m/z$  19 ion with 55 V applied across the CID region. 30
- FIGURE II.6. API mass spectra for a) room air, and b) room air with benzaldehyde vapor added. Both spectra were recorded with a CID potential of 19 V and a CID pressure of 1 Torr. The  $m/z$  107 peak is the protonated benzaldehyde ion; the  $m/z$  125, 143, and 161 peaks are hydrated, protonated benzaldehyde ions; and the  $m/z$  213 peak is protonated benzaldehyde dimer. 32

FIGURE II.7.	API mass spectrum of pinacolone and 2,4-pentanedione showing full resolution ( $R = 2,800$ , $< 0.5\%$ valley) of the protonated molecular ions.	34
FIGURE II.8.	API mass spectrum of the $^{13}\text{C}$ -xylene radical ion and the protonated benzaldehyde ion showing full resolution ( $R = 3,300$ , $< 0.5\%$ valley) of the two peaks.	36
FIGURE III.1.	Diagram of the 12 L reservoir and flow system used to supply sample gas to the API source. The functions of the four flow controllers are described in the text.	39
FIGURE III.2.	Schematic diagram of our API source illustrating the corona and CID regions, the pressures in these regions, and the potential applied across the CID region.	45
FIGURE III.3.a)	A 3x3 array of mass spectra taken from a 5x5 array displaying the dependencies of the spectra on the CID potential along the y axis and of the dilution ratio (relative humidity) along the x axis. The test atmosphere contained 36 ppm of methanol, 190 ppm of toluene, and 1.4 ppm of benzaldehyde.	48
FIGURE III.3.b)	A 5x5 array of mass spectra displaying the dependencies of the spectra on the CID potential along the y axis and of the dilution ratio (relative humidity) along the x axis. The test atmosphere contained 36 ppm of methanol, 190 ppm of toluene, and 1.4 ppm of benzaldehyde.	49
FIGURE III.4.	A 3x4 array of mass spectra displaying the dependencies of the spectra on the CID potential along the y axis and of the corona region pressure along the x axis. The test atmosphere contained 36 ppm of methanol, 190 ppm of toluene, and 1.4 ppm of benzaldehyde.	55

- FIGURE III.5.a) Ion abundance plots of five ions vs the CID potential with a corona region pressure of 1 atm and a relative humidity of 42%. For each ion the abundances are normalized to the largest value obtained for that ion in the data used to plot Figures III.5 through III.7. The ions are: m/z 33, protonated methanol; m/z 55, hydrated proton,  $\text{H}(\text{H}_2\text{O})_3^+$ ; m/z 79, fragmented ion of benzaldehyde; m/z 92, charge transfer ion of toluene; and m/z 107, protonated benzaldehyde. This data was recorded using the more concentrated test atmosphere. 57
- FIGURE III.5.b) Ion abundance plots of five ions vs the CID potential with a corona region pressure of 1 atm and a relative humidity of 6%. For each ion the abundances are normalized to the largest value obtained for that ion in the data used to plot Figures III.5 through III.7. The ions are: m/z 33, protonated methanol; m/z 55, hydrated proton,  $\text{H}(\text{H}_2\text{O})_3^+$ ; m/z 79, fragmented ion of benzaldehyde; m/z 92, charge transfer ion of toluene; and m/z 107, protonated benzaldehyde. This data was recorded using the more concentrated test atmosphere. 58
- FIGURE III.6.a) Plots of the same five normalized ion abundances in Figure III.5 vs the dilution ratio (relative humidity) with a corona region pressure of 1 atm and a CID potential of 28 V. The negative logarithmic scale provides a more even distribution of the points along the x axis. This data was recorded using the more concentrated test atmosphere. 59
- FIGURE III.6.b) Plots of the same five normalized ion abundances in Figure III.5 vs the dilution ratio (relative humidity) with a corona region pressure of 1 atm and a CID potential of 46 V. The negative logarithmic scale provides a more even distribution of the points along the x axis. This data was recorded using the more concentrated test atmosphere. 60
- FIGURE III.7. Plots of the same five normalized ion abundances in Figure III.5 vs the corona region pressure with a relative humidity of ~27% and a CID potential of 28 V. The data was recorded using the more concentrated test atmosphere. 61

- FIGURE III.8.a) Ion abundance plots of four ions vs the CID potential with a corona region pressure of 1 atm and a relative humidity of 49%. For each ion the abundances are normalized to the largest value obtained for that ion in the data used to plot Figures III.8 and III.9. The ions are:  $m/z$  33, protonated methanol;  $m/z$  79, fragmented ion of benzaldehyde;  $m/z$  92, charge transfer ion of toluene; and  $m/z$  107, protonated benzaldehyde. This data was recorded using the less concentrated test atmosphere. 69
- FIGURE III.8.b) Ion abundance plots of four ions vs the CID potential with a corona region pressure of 1 atm and a relative humidity of 6%. For each ion the abundances are normalized to the largest value obtained for that ion in the data used to plot Figures III.8 and III.9. The ions are:  $m/z$  33, protonated methanol;  $m/z$  79, fragmented ion of benzaldehyde;  $m/z$  92, charge transfer ion of toluene; and  $m/z$  107, protonated benzaldehyde. This data was recorded using the less concentrated test atmosphere. 70
- FIGURE III.9.a) Plots of the same four normalized ion abundances in Figure III.8 vs the dilution ratio (relative humidity) with a corona region pressure of 1 atm and a CID potential of 28 V. The negative logarithmic scale provides a more even distribution of the points along the x axis. This data was recorded using the less concentrated test atmosphere. 71
- FIGURE III.9.b) Plots of the same four normalized ion abundances in Figure III.8 vs the dilution ratio (relative humidity) with a corona region pressure of 1 atm and a CID potential of 46 V. The negative logarithmic scale provides a more even distribution of the points along the x axis. This data was recorded using the less concentrated test atmosphere. 73
- FIGURE IV.1. Four scan averages of mass spectra recorded before irradiation. The conditions are: a) background, 1  $\mu$ A corona current; b) after addition of 10 ppm of  $D_3$ -toluene to the reservoir, 0.2  $\mu$ A; c) 1  $\mu$ A; and d) 5  $\mu$ A. 83
- FIGURE IV.2. Ion abundances normalized to the total ion current (arbitrary units) vs the corona current plotted on a logarithmic scale. The  $m/z$  ratios plotted correspond to ions identified in the text. 87

- FIGURE IV.3. Illustration of the directions of ion travel and sample flow in the corona region. The majority of ions sampled by the mass analyzer are formed within a relatively small solid angle centered on the corona tip-to-orifice axis. 91
- FIGURE IV.4. A schematic diagram of the needle tip illustrating regions where different positive ions are presumed to predominate based on the sequence of ion-molecule reactions discussed in Appendix C. The flow direction assumed in Appendix C is also illustrated. The OH enriched volume is larger than the enclosed region due to diffusion of OH away from the tip. 93
- FIGURE IV.5. Four scan averages of mass spectra recorded using a 0.2  $\mu$ A corona current at the lower flow a) before irradiation and without CO addition; b) before irradiation and with 0.8% CO addition; and c) after irradiating the reservoir for 3 hrs and with 0.8% CO addition. Dots mark spurious product and related peaks. Diamonds denote true photooxidation product and related peaks from methyldeuterated toluene. 97
- FIGURE IV.6. Four scan averages of mass spectra recorded using a 0.2  $\mu$ A corona current before irradiation a) without CO addition and with the lower flow; b) without CO addition and with the higher flow; and c) with 0.8% CO added and with the lower flow. Spurious product and related peaks are marked by dots and two types of chemical noise peaks are denoted by triangles (see text). 100
- FIGURE IV.7. Four scan averages of mass spectra obtained after irradiating the reservoir for 3 hrs using a 0.2  $\mu$ A corona current a) with no CO addition and with the enhanced flow and b) with 0.8% CO addition and with the lower flow. 103
- FIGURE V.1. Response curve for benzaldehyde dissolved in xylene: abundance of the m/z 107 ion (arbitrary units) vs concentration of benzaldehyde (ppb) corrected for dilution in the reservoir. 109
- FIGURE VI.1. A mass spectrum comprised of 25 summed scans over a mass range of 89-111 Daltons of toluene photooxidation products (and contaminants) recorded after irradiating the reservoir for 1322 min. The m/z 92 (toluene) and 107 (protonated benzaldehyde) peaks were used for calibration. The m/z 97 and 99 peaks are shown with the time (x) axis expanded. 123

FIGURE VI.2.	Mass spectra recorded at $m/z$ 97 after irradiating the reservoir for a) 0 min, b) 20 min, c) 66 min, d) 91 min, e) 191 min, f) 300 min, g) 1100 min, and h) 1322 min. The CID potential was 28 V for a)-c) and e)-h); 37 V for d).	126
FIGURE VI.3.	Mass spectra recorded at $m/z$ 99 after irradiating the reservoir for a) 0 min, b) 20 min, c) 66 min, d) 91 min, e) 191 min, f) 300 min, g) 1100 min, and h) 1322 min. The CID potential was 28 V for a)-c) and e)-h); 37 V for d).	128
FIGURE VI.4.	Mass spectra recorded at $m/z$ 85 after irradiating the reservoir for a) 0 min, b) 1142 min, c) 1147 min, and d) 1313 min. The CID potential was 28 V for a), c), and d); 19 V for b).	131
FIGURE VI.5.	Mass spectra recorded at $m/z$ 103 after irradiating the reservoir for a) 0 min, b) 20 min, c) 66 min, d) 91 min, e) 191 min, f) 300 min, g) 1100 min, and h) 1322 min. The CID potential was 28 V for a)-c) and e)-h); 37 V for d).	132
FIGURE A.1.	Simplified drawing of the API source illustrating the locations of the corona and collisionally induced dissociation (CID) regions and of the apertures between those regions and the mass analyzer. Typical pressures within each region and typical potentials applied to the aperture electrodes are also indicated.	146
FIGURE A.2.	Schematic diagram of the discharge suppression system. The plots illustrate how the system separates the potential (dashed) and pressure (solid) gradients along the pumping line to achieve discharge suppression.	148



List of Tables

TABLE VI.1.	Observations of peak areas for toluene photo-oxidation products identified by the Shepson, Bandow, and O'Brien groups. The $m/z$ 89 product has not been reported before.	136
TABLE C.1.	Rate constants for OH attack of various compounds at a temperature of 298°K, a temperature not much different from that in the corona region when using a 0.2 $\mu$ A corona current. The concentration of third bodies, [M], is that at atmospheric pressure and is included in the third order rate constants. The factors are the ratio of each competing OH reaction rate constant to that of toluene.	156
TABLE C.2.	Percentages of OH radicals consumed by self-consumption (reactions T1-T4), by toluene (reaction T6), by NO (reaction T5), by NO <sub>2</sub> (reaction T7), by flow of OH out of the enriched volume, and by CO (reaction T10) computed using the model in Appendix C. Percentages are listed with and without addition of 0.8% CO assuming no diffusion and complete diffusion, i.e. diffusion sufficient to yield homogeneous distributions of components within the corona region.	160
TABLE C.3.	Percentages of benzaldehyde consumed by ionization, by OH radical attack, and lost by flow from the OH enriched region for the normal and enhanced flow conditions assuming no diffusion and complete diffusion. The table entries were calculated using equation 29 to estimate [OH] <sub>SS</sub> and equation 41 to determine [benz] <sub>SS</sub> . $1.8 \times 10^{-9}$ cm <sup>3</sup> molecule <sup>-1</sup> sec <sup>-1</sup> , taken from reaction 3, was arbitrarily used for an average $k_{ion}$ , while all of the ions in this region were assumed to be capable of protonating benzaldehyde.	164

## ABSTRACT

Most analytical techniques used to study atmospheric oxidation have lacked the sensitivity necessary to determine oxidation products directly in the gas phase. Loss or alteration of products can occur during concentration or separation steps before analysis.

Atmospheric pressure ionization (API) mass spectrometry is potentially a very powerful technique for such studies. API provides high sensitivity for hydrocarbon oxidation products containing heteroatoms (O and N). An API source for a VG 7070E-HF mass spectrometer was fabricated and successfully operated at an accelerating potential of 6 kV to provide medium resolution (4,800, 10% valley,  $m/z$  92, 1% of the maximum ion signal). This resolution is more than sufficient to separate mass peaks due to oxidized hydrocarbons having the same nominal mass, but differing by  $-\text{CH}_2\text{CH}_2-$  vs  $>\text{C}=\text{O}$  groups.

The mass spectra obtained can contain hydrated, fragmented, and molecular ions; multiple ions from each analyte in a gas mixture complicate spectra and decrease sensitivity. Manipulation of three variables, the relative humidity of the sample gas, the pressure in the corona discharge region, and the potential across the collisionally induced dissociation region, can be used to simplify the mass spectra, to maximize sensitivity for analytes, and to differentiate between hydrated, fragmented, and molecular ions.

Spurious oxidation products formed by free radical reactions with OH radicals generated in the API source interfered with oxidation studies. Strategies for suppressing peaks in the mass spectra due to the interfering chemistry are demonstrated: 1) operating at the lowest sustainable corona discharge current, 2) adding CO to scavenge OH radicals, and 3) modestly increasing the flow of sample gas through the API source.

A dynamic range of two decades and a detection limit of 8 ppb are demonstrated for benzaldehyde, and factors causing nonlinearity in the response curve are discussed.

Several toluene oxidation products, identified after concentration or separation steps in previous studies, were found in our reaction vessel gas. Using medium resolution the mass peaks due to these products were separated from each other and from background peaks. Exact masses were then determined and used to assign molecular formulae to the ions corresponding to the product peaks.

CHAPTER I  
A ROLE FOR ATMOSPHERIC PRESSURE IONIZATION MASS SPECTROMETRY  
IN ATMOSPHERIC STUDIES

I.1. INTRODUCTION

I.1.a) Developing Models for the Atmosphere

To understand humankind's present and future effects on the composition of the atmosphere, determination of trace atmospheric constituents is necessary. Photochemical smog (1), global warming (2), acid rain (3), and depletion of the ozone layer (4) are four problems that are probably exacerbated by anthropogenic emissions of gases into the atmosphere. The chemistry of both clean and polluted air must be understood before remedial legislation, if necessary, can be rationally formulated and enforced to mitigate detrimental atmospheric effects caused by anthropogenic emissions.

Over one hundred reactions (5) involving many chemical species are included in atmospheric models; accurate determinations of these species in the atmosphere or in simulated atmospheres are necessary to develop models that have good predictive value.

I.1.b) A Gap in the Photochemical Smog Model

Although the atmospheric photooxidation of alkanes and alkenes is reasonably well understood (5), that of aromatic compounds is not (6-9).

Aromatic compounds comprise over 40% of gasoline and are common volatile solvents (10). Consequently, nearly one-fourth of the non-methane hydrocarbons in ambient Los Angeles air were found to be aromatics; these aromatics are responsible for over one-third of the total photochemical reactivity (11).

Toluene, comprising about one-third of the aromatic compounds (12), has been the most studied of the group; its atmospheric photooxidation is simulated by irradiating reaction chambers of Pyrex or Teflon film containing clean atmospheres to which toluene and  $\text{NO}_x$  have been added. Past studies sampling irradiated atmospheres have accounted for less than half of the total carbon from reacted toluene (9,10,13-15), even when aerosols, which comprised only 2-6% of the carbon balance in a study by Leone et al. (9), were determined. O'Brien et al. (16), catalytically converted gas phase carbon to  $\text{CO}_2$ , measured the  $\text{CO}_2$  quantitatively by gas chromatography, and determined that as much as 63% of the missing carbon left the gas phase. Yet many products adhering to the walls of the reaction vessel were likely formed in the gas phase and might have been detectable with analytical techniques sensitive to gas phase concentrations of these products. The products formed in the gas phase have the greatest relevance for atmospheric photooxidation models since the atmospheric surface to volume ratio is generally less than that of irradiated reaction chambers.

With appropriate assumptions, models (6-9) can account for the build-up and decline of several toluene photooxidation products during irradiation. But with over half of the carbon unaccounted for, such models must, by necessity, overlook major reaction pathways and

products. Clearly, an analytical technique capable of determining the missing products would provide data necessary to improve these models.

## I.2. LIMITATIONS OF ANALYTICAL TECHNIQUES USED TO STUDY ATMOSPHERIC CHEMISTRY

### I.2.a) Analytical Techniques Requiring Sample Concentration

Analytical techniques that identify and quantify many classes of oxidized compounds are most useful for analyzing contents of reaction vessels. Generally, the products of atmospheric photooxidation have been studied by gas chromatography with flame ionization or electron capture detection (6,9,10,17), gas chromatography/mass spectrometry (6,14,17), high performance liquid chromatography (13,14,17,18), or tandem mass spectrometry (19). All of these techniques require concentration of samples through cold trapping (9,10,14,17), adsorption in packed cartridges (6,17,18), or collection of gas phase products in a solvent (13,14,18), which can be followed by evaporation to a small volume (19). Often the concentration step is followed by derivatization (13,14,18).

Using chromatographic techniques to determine trace atmospheric species has several disadvantages.

- 1) Concentration, derivatization, and separation are laborious and time consuming relative to direct sampling or in situ techniques.

- 2) The time required for pre-analysis steps prohibits identifying reactive products.

3) Not all classes of compounds pass through a given column, requiring use of two or more columns (6,14).

4) Concentration by cold trapping before analysis may allow condensed phase or surface reactions to occur that can alter the identities and concentrations of the original sample components. Both Kenley et al. (17) and O'Brien et al. (10) noted reactions between  $\text{NO}_2$  and photooxidation products of aromatic compounds in their cold traps.

5) Very large reaction chambers are necessary to provide sufficient sample to follow product generation during a single batch experiment. Reaction chambers with volumes of 5,800 L and  $65 \text{ m}^3$  have been used to study atmospheric reactions (6,9).

Collecting products by flushing the reaction vessel with a solvent also has disadvantages.

1) Some components may be insoluble in a particular solvent.

2) Products can react with the solvent. O'Brien et al., studying toluene photooxidation (19), produced methoxy derivatives when methanol was used to collect the products.

3) Volatile compounds may be lost during evaporation. O'Brien et al. (19) collected products with  $\text{CH}_2\text{Cl}_2$  solvent, evaporated most of the solvent, and inserted a portion of the residue into a chemical ionization source with a probe. No ion peaks for the known products, formaldehyde, peroxyacetyl nitrate, and methyl nitrate, were found.

4) Chemical noise due to the solvent can create uncertainty in identifying true reaction products. Dumdei and O'Brien used two forms of deuterated toluene to overcome this interference and to distinguish between isomers (19,23).

#### I.2.b) In Situ Analytical Techniques

Long path fourier transform infrared (FTIR) spectroscopy (20-22) and differential optical absorption spectroscopy (15,21,22), have been employed to study atmospheric photooxidation in situ. These optical spectroscopic techniques avoid the disadvantages listed above; they are non-destructive of the sample and require no collection, concentration, or separation steps prior to analysis. But optical spectroscopic techniques have two major disadvantages.

1) The absorption spectra obtained are composite signals arising from the gas in the reaction chamber and condensed products on the chamber's walls or in aerosols (15,20). These spectra require deconvolution into contributions from numerous reactant and product species. Dumdei and O'Brien (23) identified 27 possible products from toluene photooxidation in the tandem mass spectrometry experiment cited above. Many of these compounds contain the same functional groups and would have similar infrared absorption spectra making determination of individual products from a difference spectrum difficult or impossible. Bandow et al. (15) were unable to identify a toluene photooxidation product from a difference spectrum



obtained after subtraction of several contributions due to known components in the reaction vessel from a composite long path FTIR spectrum.

2) Water vapor, necessary to simulate natural atmospheric conditions, absorbs so strongly over a wide IR region, that dry air must be used in optical spectroscopy experiments (15,20-22).

### I.3. Criteria for an Ideal Analytical Technique for Atmospheric Studies

The ideal analytical method would be capable of identifying and quantifying, in situ, all photooxidation products produced from concentrations of reactants representative of the atmosphere. The technique must be extremely sensitive and capable of distinguishing between individual compounds from classes of oxidized hydrocarbons in the presence of one another.

It is improbable that any one analytical technique could meet these criteria completely. One technique which could more closely satisfy these criteria than the techniques used historically, however, is atmospheric pressure ionization mass spectrometry.

### I.4 Atmospheric Pressure Ionization (API) Mass Spectrometry

#### I.4.a) Suitability

Atmospheric pressure ionization mass spectrometry (APIMS) is an extremely sensitive analytical technique for identifying and quantifying trace constituents in air (24) without prior sample concentration or

separation. Detection limits of compounds in the ppb to ppt range are typical and dynamic ranges of 3 decades are cited (25). This greater sensitivity vs electron impact (EI) and chemical ionization methods and a wide dynamic range suggest API mass spectrometry could be used to study photooxidation of naturally and anthropogenically emitted organic compounds present in the atmosphere directly in the gas phase.

#### I.4.b) Description of API Sources

Figure I.1 depicts schematically regions common to most API mass spectrometers. Sample gas enters the ionization region where ions could be created in various ways at atmospheric pressure (26). Most often, they have been created by secondary ionization with beta particles emitted from  $^{63}\text{Ni}$  foil or by corona discharges (26-29). A differentially pumped region is generally necessary to isolate the atmospheric pressure in the ionization region from the low pressure maintained in the mass analyzer. Most neutral molecules entering this intermediate pressure region are pumped out, while ions are drawn into the mass analyzer.

In APIMS, ionization occurs at atmospheric pressure rather than under vacuum as is the case for other ionization techniques. The mean free paths of species are small and numerous collisions ensure attainment of a steady state approaching chemical and thermal equilibrium within the time required for transport through the ionization region (27). Conversely, ions formed at low pressure have long mean free paths; fewer collisions result in a mixture of unequilibrated ions and neutral species. Consequently, in API sources, ~100% of the

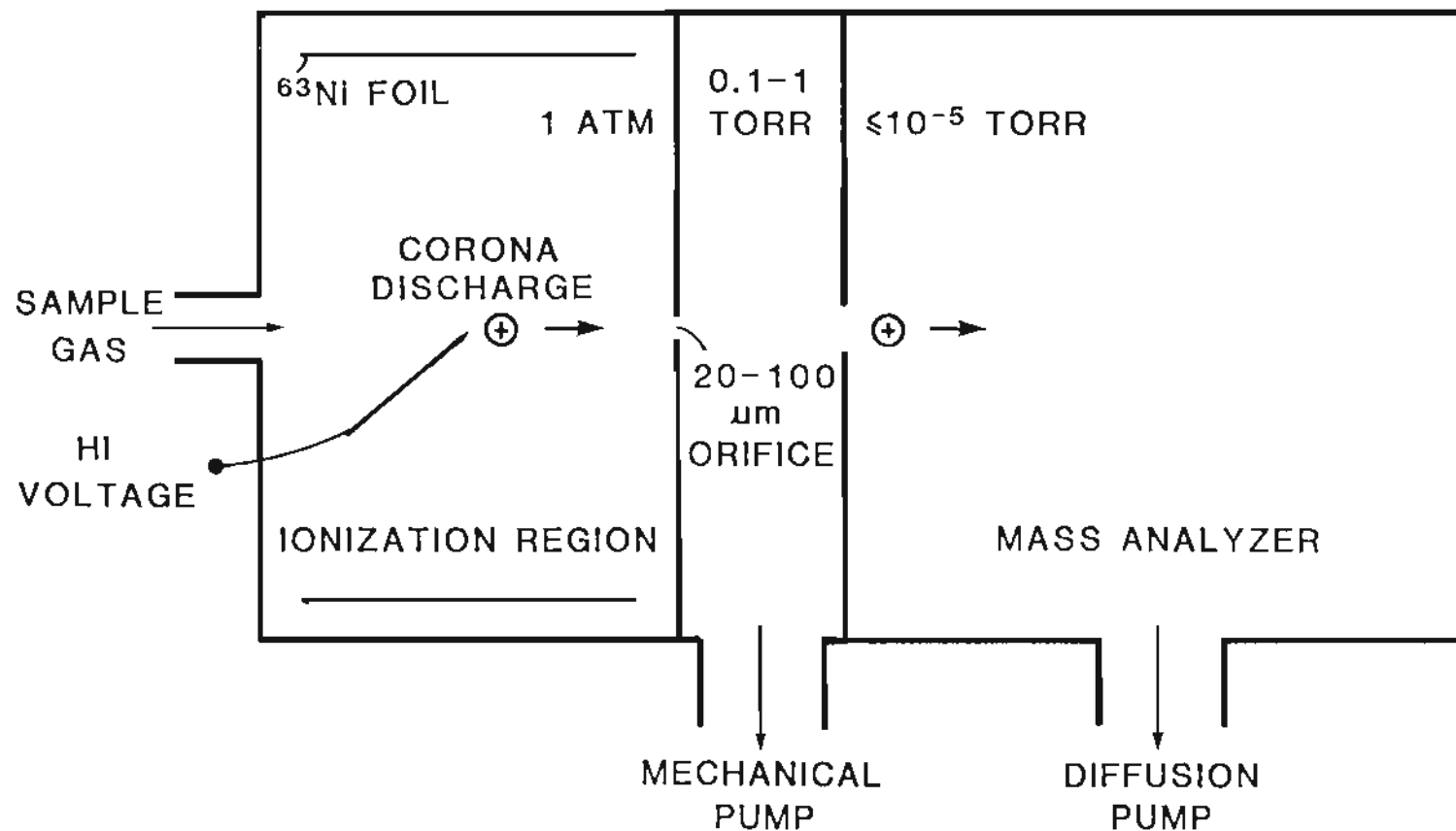


FIGURE I.1. Schematic diagram of an Atmospheric Pressure Ionization source showing the ionization region where ions are produced by either a beta particle emitting foil or a corona discharge. The direction of ion travel through the differentially pumped region into the mass analyzer is noted, as are the approximate pressures in each of the three regions.

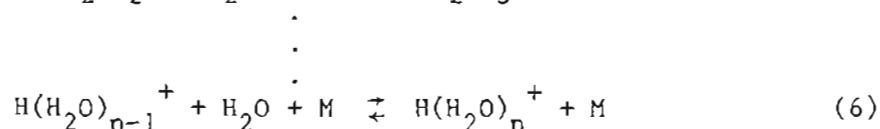
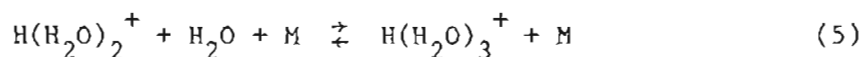
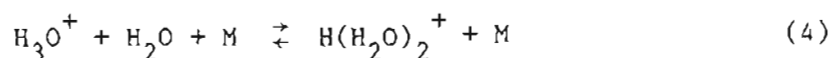
trace compounds undergoing sufficiently exothermic ionization reactions are ionized (26), resulting in greatly enhanced sensitivities for these compounds relative to EI sources for which only 0.01-0.1% ionization occurs (27). In addition, API is a softer ionization technique than chemical ionization (30), since ions formed are more likely to lose excess internal energy through collisions before unimolecular decomposition (fragmentation) can occur. Minimal fragmentation of molecular ions has made API attractive for liquid chromatography, tandem mass spectrometry analyses of non-volatile compounds (31).

#### 1.4.c) Ionization Mechanism

Both positive and negative ions are formed in the ionization region. As in chemical ionization techniques, the sample gas may be spiked with various reagents to increase specificity and sensitivity for a particular class of compounds. Without such additives, however, water in air is the chemical ionization reagent in the positive mode. Only the sequence of reactions producing positive ions in air containing > 0.1% of water will be discussed; positive ion spectra using such sample gases were recorded in all experiments.

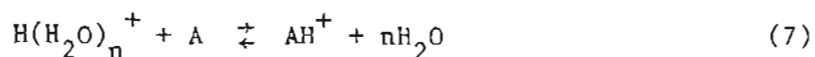
Ionization of air initially produces predominantly  $N_2^+$  and  $O_2^+$  ions. A sequence of ion-molecule reactions then produces hydrated protons,  $H(H_2O)_n^+$  (32). For the  $N_2^+$  ions:



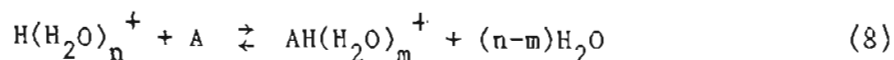


In addition to their direct formation in the corona discharge,  $\text{O}_2^+$  ions are produced by reaction of  $\text{N}_4^+$  clusters with  $\text{O}_2$  (33). Many  $\text{O}_2^+$  ions form  $\text{O}_4^+$  cluster ions; both  $\text{O}_2^+$  and  $\text{O}_4^+$  ions react with water to form  $\text{O}_2^+(\text{H}_2\text{O})$ . This ion then reacts to form hydrated protons and hydroxyl radical through consecutive reactions with one or more additional water molecules (34). The majority of the hydrated protons are formed through the oxygen ion pathways.

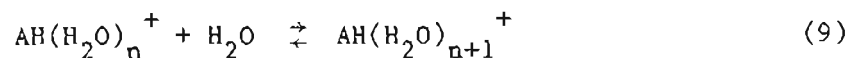
With proper design (Chapter II) the ion residence time in the ionization region is sufficient for these hydrated protons to serve as the primary reagent ions in the positive ionization mode by protonating trace molecules that are stronger bases in the gas phase than water. Many classes of organic compounds containing heteroatoms, e.g. O or N, have sufficiently high proton affinities to be ionized via this gas phase ion-molecule reaction.



Hydrated analyte ions are seen in addition to non-hydrated analyte ions in API mass spectra. These ions can arise from the transfer of one or more water molecules during proton transfer to a given species from a hydrated proton (28).



As for the hydrated protons, equilibria between hydrated analyte ions are established in the source for oxygenated analytes (35).



In addition, adiabatic expansion from the ionization region at atmospheric pressure into the next region at 1 Torr through a small orifice (Figure I.1) causes condensation of additional water molecules about ions in the gas stream (36).

#### I.4.d) Coalescing Hydrated and Non-hydrated Analyte Ion Peaks

Partitioning of each analyte's signal into peaks associated with different numbers of water molecules, and hence, different m/z ratios, complicates qualitative interpretation of mass spectra and decreases sensitivity.

Two general strategies for eliminating or reducing the abundance of hydrated protons larger than the hydronium ion in API mass spectra are to suppress their formation and to disaggregate those that are formed. Shahin demonstrated that reducing the number density of water molecules in the ionization region by lowering the pressure or the relative humidity in the region reduced the average size of the hydrated protons that are formed (37).

Kambara and Kanomata showed that hydrated protons exiting the ionization region may be disaggregated at about 1 Torr via gas phase collisions in the differentially pumped region (Figure I.1) between the ionization chamber and the source optics of the mass analyzer (38). A small potential applied across this region, the collision-induced

dissociation (CID) region, accelerates the ions and, hence, increases their kinetic energy between collisions with neutral molecules. As the CID potential is increased, the dissociation of hydrated protons following numerous collisions becomes more complete. If this method of disaggregating hydrated protons were applied to hydrated analyte ions, too great a potential applied across the CID region could fragment the molecular ions. The formation of fragmented ions would also reduce the abundance of molecular ions, again decreasing sensitivity and complicating the mass spectra. Fragmented ions are useful for identifying pure compounds, but generally, their appearance in spectra recorded from mixtures of many components is not helpful.

#### I.4.e) Interferences

Mass peaks arising from at least three other sources in addition to the two already mentioned can interfere with the determination of photoproducts by API mass spectrometry; all five interferences are listed:

- 1) compounds not associated with the photoreaction products of interest,
- 2) products from reactions occurring in the ionization region of the ion source,
- 3) isotopic peaks from major components in the mixture,
- 4) series of hydrated ions resulting from the ionization process, and
- 5) fragmented ions formed from molecular ions.

#### I.4.f) Resolution Required

If photooxidation products within complex mixtures are to be determined, multiple peaks at a given nominal mass that arise from contaminant, reactant, product, isotopic, hydrated, or fragmented ions must be resolved. Determination of an exact mass for each separated peak would provide a molecular formula, essential for each ion's identification. Instances can arise where high resolution would be required to distinguish between two molecular formulae, but the most important requirement is to be able to distinguish between photoproducts oxidized to different degrees, i.e. between products differing by a  $-\text{CH}_2-\text{CH}_2-$  group vs a  $>\text{C}=\text{O}$  group, corresponding to a mass difference of 0.0364 Daltons. A medium resolution of 4,100 (50% valley) up to a mass of 150 Daltons ( $150/0.0364$ ), an upper mass limit for products expected from most photooxidation experiments, would provide this capability.

Unfortunately, the resolving power of current API instrumentation is inadequate for this task. API sources have most often been coupled with quadrupole mass filters (24-29) and less often, with single focusing, magnetic sector mass analyzers (39,40). Unit resolution is commonly cited for quadrupole systems; examination of published spectra suggests that in many cases this claim is optimistic. Sakairi and Kambara specified a resolution of 300 (10% valley) for their magnetic sector instrument operated with an acceleration voltage of 3 kV (30).

Double focusing mass spectrometers provide much greater resolving capability than single sector instruments. The resolution specified for



the VG 7070E-HF mass spectrometer available at the Oregon Graduate Center operating in the electron impact mode is 25,000 (10% valley) while retaining 0.1% of the maximum ion signal (41). It seemed feasible that an API source interfaced to this instrument could achieve the desired resolving capability.

In tandem mass spectrometry studies of simulated atmospheres (19) the daughter ion spectra often provided sufficient structural information to identify the parent ion selected by the first quadrupole. When multiple ions are present at the same nominal mass, however, unit resolution cannot separate them; the daughter ion spectrum is a composite of fragmented ions formed from more than one parent ion. Such a spectrum can be impossible to interpret. An instrument providing medium resolution would identify those nominal masses at which multiple ions are found, and exact mass determinations would provide molecular formulae for those ions. This information could allow composite daughter ion spectra to be deconvoluted so that parent ions could be identified. Hence, the capabilities of the two types of instruments would complement each other.

## 1.5 RESEARCH GOALS

Our primary goal was to build an API source for this instrument that would provide sufficient sensitivity and resolution to establish the resulting instrument as a powerful analytical tool for identifying photooxidation products at trace levels in simulated atmospheres.

Several steps were required to attain this goal.

1) A discharge suppression device was designed and built to permit use of the mass spectrometer's full accelerating potential, thereby maximizing sensitivity and resolution.

2) An API source tailored to this instrument was designed and built, and resolution adequate to distinguish between hydrocarbons having the same nominal mass, but different numbers of oxygen atoms, was demonstrated.

3) The effects of three variables on the mass spectra obtained were studied; manipulation of these variables was then used to simplify spectra, to maximize sensitivity, and to differentiate between molecular, hydrated, and fragmented ions in the spectra.

4) The problem of interfering reactions occurring in the API source that gave rise to some of the same compounds produced by photooxidation of toluene, the compound chosen for initial studies, was overcome.

5) A useful dynamic range under the experimental conditions to be used in atmospheric studies was demonstrated.

6) The medium resolution of the instrument was used to confirm the presence of toluene photooxidation products in the gas phase, products that had been identified in past studies by analytical techniques that sampled the condensed phase as well.

The discharge suppression device is described in Appendix A; steps 2 through 6 are discussed in Chapters II through VI, respectively.

## CHAPTER II

## A MEDIUM RESOLUTION API MASS SPECTROMETER

## II.1. SOURCE DESIGN AND CONSTRUCTION

## II.1.a) Choice of Ionization Method

The two most common methods of ionizing sample gas molecules are through secondary ionization by beta particles emitted from  $^{63}\text{Ni}$  foil and by direct ionization using a corona discharge. We chose to use the latter method because it offers a wider dynamic range, a modestly higher sensitivity, and the possibility of varying ion residence times within the ionization region.

Carroll et al. (42) compared API sources using these two ionization methods. They found ion densities entering the mass analyzer (Figure I.1) were two orders of magnitude greater using the corona discharge; a greater number of primary ions permits larger concentrations of ionizable components in a gas mixture to be determined before depletion of the primary ions causes the signal to become saturated.

The Carroll group also observed several times greater sensitivity using the corona discharge due to the separation of positive and negative charges induced by the electric field. The ionization efficiency, typically 0.1%, is determined primarily by the ratio of the rate of ion production to the rate of charge recombination; separation of charges decreases the recombination rate (42).

### II.1.b) Source Block

Construction details of our API source are displayed in Figure II.1 (note that Figure II.1 is not a uniplanar cross-sectional view of the source). The body of the source is machined from a 2 in. diameter, 304 stainless steel cylinder. Shown in the figure are the sample inlet line, the corona discharge assembly, the first and second aperture assemblies, the pumping line, and the ion source's lens assembly; not shown are the vacuum gauge line provided to monitor the pressure in the collisionally induced dissociation (CID) region, the source heater (VG), and the thermocouple used to monitor the source temperature. The design of the source is based primarily on Caldecourt's (43), which in fact is a modification of a design by Kambara (40). Unlike Caldecourt's source, however, ours does not have a lens in the CID region; a more recent design by Kambara (30) also lacks this lens.

The corona discharge assembly consists of a 5 kV feedthrough (Ceramaseal), a shortened sewing needle made of Ni-coated steel (Milward #7), an Al-holder for the corona-tip, and a Vespel cylinder that aligns the tip and its holder with the exit orifice. The Vespel cylinder has a 1/4 in. milled slot that aligns with the inlet port and allows unobstructed flow of the sample gas into the corona discharge region. The tip of a corona-needle is located  $4.6 \pm 0.1$  mm from the exit aperture by using a fixture to position the needle within its holder before tightening the set screw. This tip to orifice distance is 15% larger than that used by Dzidic et al. (44); it was chosen to ensure sufficient residence time for the full sequence of ion-molecule

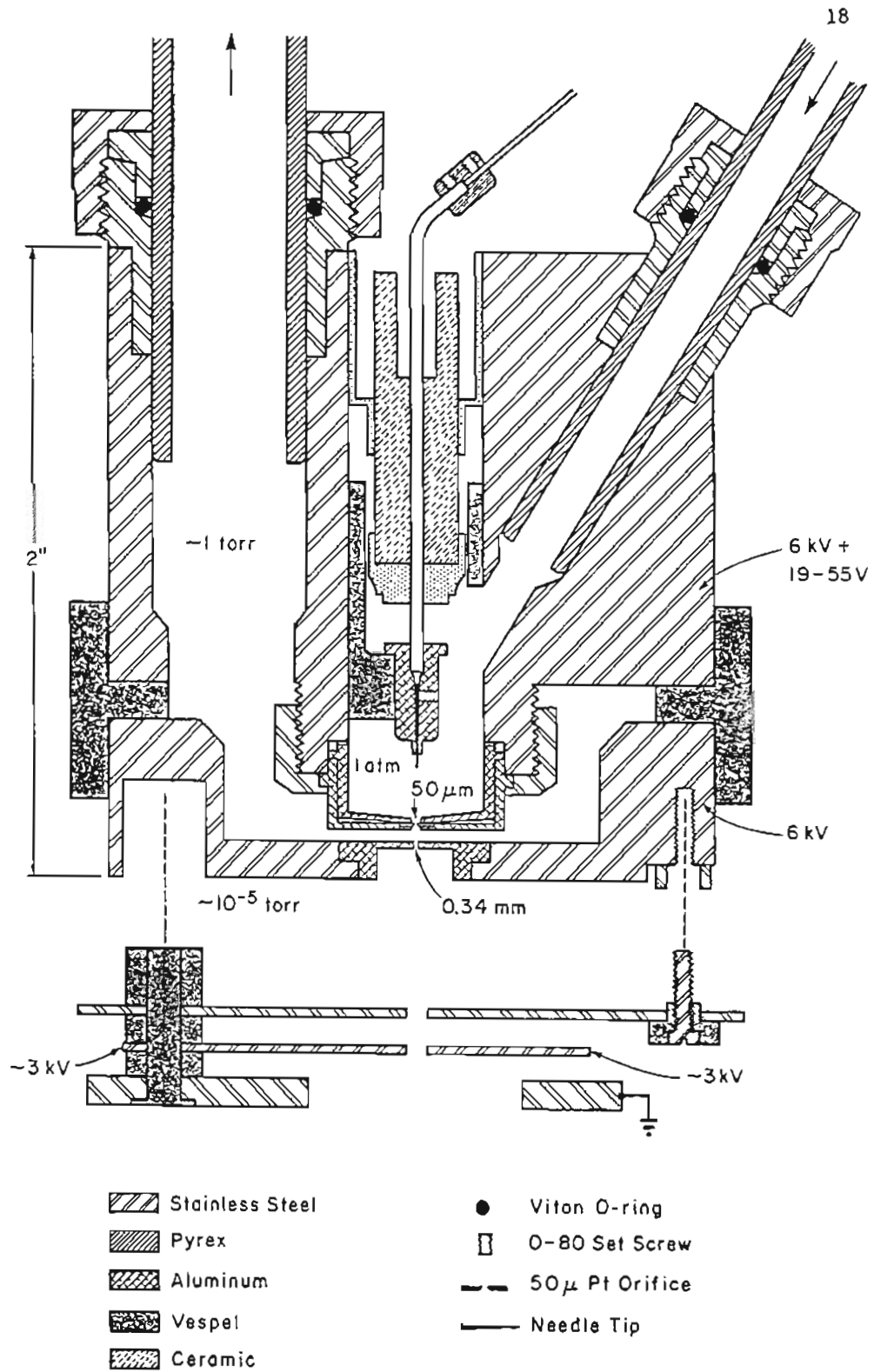


FIGURE II.1. Construction details of the API source (non-uniplanar cross section).

reactions to take place and produce abundant, protonated analyte ions.

The circular aperture separating the corona region from the CID region is centered in a 3 mm diameter, 0.010 in. thick Pt-disc (Ebtec). The annular region surrounding the orifice is countersunk on one side of the disc so that the aperture itself is ~0.003 in. long. Operation of the source with four aperture sizes, viz. 25, 50, 75, and 100  $\mu$ m, was investigated. The aperture disc is located and held firmly in place by two aluminum, cylindrical caps that are firmly clamped onto the end of the corona discharge chamber with a threaded ring (Figure II.1); this design allows quick access to the aperture disc for cleaning or replacement. The outside, bottom surface of the inner cap is faced at a  $2^\circ$  angle to provide a pinching action on the aperture disc that ensures a good seal. The sealing surfaces of the present aluminum caps are too easily scratched; therefore, future replacement caps will be made of stainless steel. A Vespel ring provides the seal between the caps and the chamber body.

The 304 stainless steel end plate of the API source is insulated from the source body by a large Vespel ring. This plate has an aluminum disc with a 0.34 mm aperture press-fitted into its center and a standard VG ion source lens assembly mounted onto its outside face. The Macor standoffs normally used to separate the lens electrodes were replaced with more durable Vespel insulators. The last lens plate, which is maintained at ground potential, has two holes which mate to dowels located inside the source housing on the support structure just in front of the entrance slit assembly; this docking arrangement, which is a standard feature of commercial VG ion sources, automatically aligns the

axis of the ion source with the optical axis of the mass analyzer.

### II.1.c) Source Support

Figure II.2 is a photograph of the API source (right side) and of the customized support assembly that was built to adapt the API source to the VG 7070E-HF mass spectrometer. The design preserves the standard, modular construction of commercial ion sources built for VG 7070 mass spectrometers. The main support components were custom fabricated from 304 stainless steel; the API source is insulated from these by three Vespel posts. Three gas lines service the API source: an inlet line (Teflon) that provides the corona discharge region with sample gas at 1 atm, a line leading from the CID region to a Teledyne-Hastings-Raydist DV-6M TC pressure gauge outside the vacuum envelope (glass to metal bellows), and a large diameter, Pyrex pumping line leading from the CID region. Both Teflon and glass-metal bellows provide adequate insulation for the source, which is maintained at 6 kV, and at the same time, ample flexibility to accommodate for the slight movement of the outer flange relative to the source that occurs during pump down. A 1 in. o.d. metal bellows sealed to the Pyrex provides this same function for the large pumping line (Figure II.2); the integrity of the vacuum envelope is maintained at the point where the pumping line passes through the source-housing flange by a 1 in. Cajon O-ring fitting welded into the flange. Similar seals with 0.25 in. Cajon O-ring fittings are provided for the sample inlet line and the pressure measurement line at their points of egress.

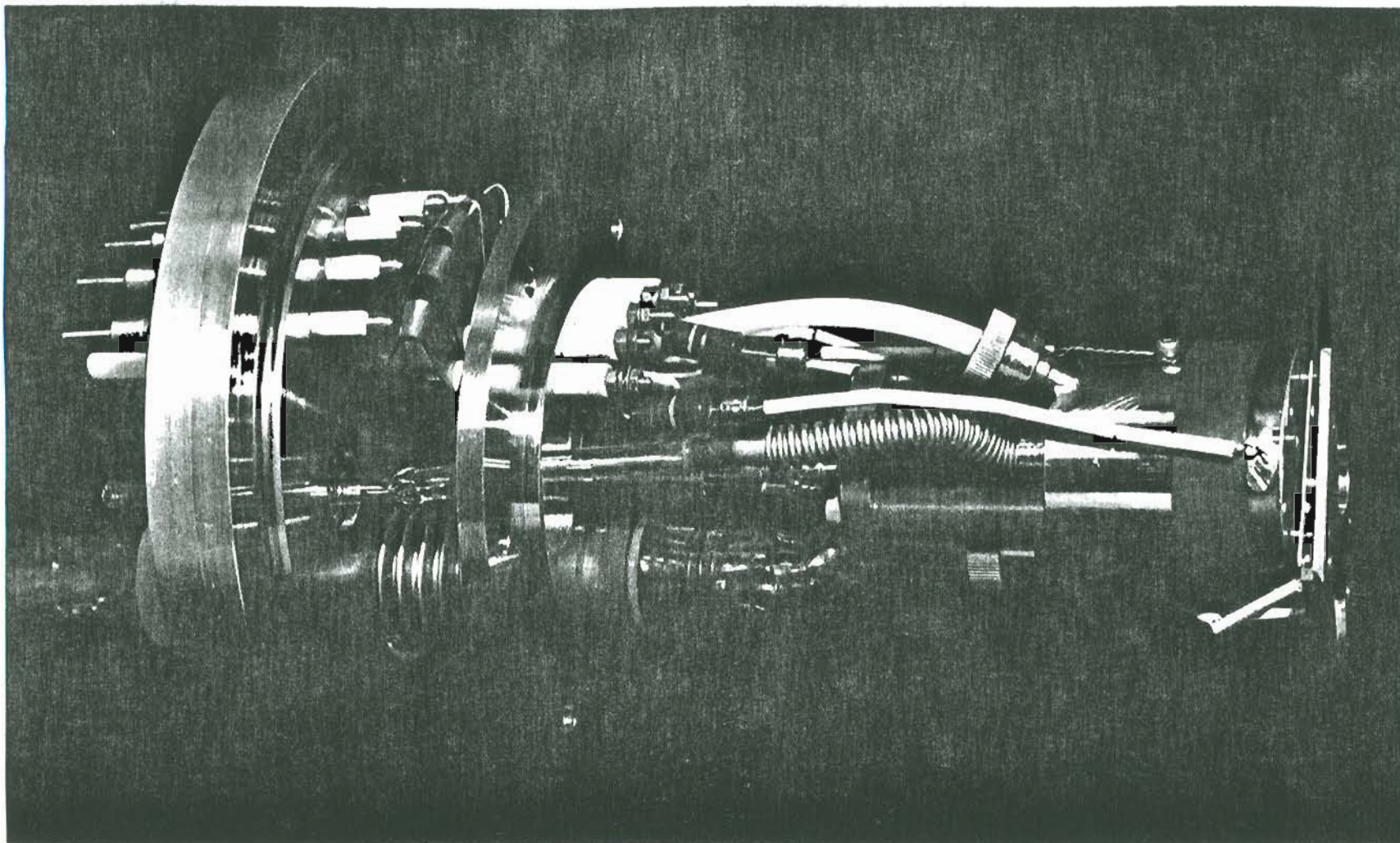


FIGURE II.2. Photograph of the API source and the support assembly used to adapt it to the VG 7070E-HF mass spectrometer.



Eleven 10 kV feedthroughs (Ceramaseal) are welded into the source-housing flange to provide electrical connections to the API source, beam centering half plates, thermocouple junction, and heater; the feedthroughs were modified to conform to standard VG form and dimensions.

#### II.1.d) Pumping System and Arc Suppression

A 50 cfm, Alcatel 2063, two-stage rotary pump is used to pump the API source. During operation, the pressure within the pumping line falls from  $\sim 1$  Torr in the CID region to  $\sim 0.05$  Torr at the head of the pump. In the vicinity of 0.1 Torr, conditions are ideal for glow discharges between the API source at 6 kV and grounded surfaces along the pumping line (45); these discharges disrupt operation, damage electronic components, and expose human operators to the hazard of a high voltage shock. The arcing problem was eliminated by devising a discharge suppression system (Appendix A) to prevent arcing to the pump and by isolating grounded surfaces within the mass spectrometer's ion source housing from exposure to the source at high potential through conducting gas volumes. Figure II.3 shows how the two grounded flanges and the large, grounded metal bellows used in the main pumping line were isolated from the gas within the pumping line ( $\sim 1$  Torr); the volume of gas extending from the three Buna-N O-rings between the inner surface of the bellows and the outer surface of the inner Pyrex tubing is at atmospheric pressure and is nonconducting at ion source potentials ( $\leq 6$  kV).

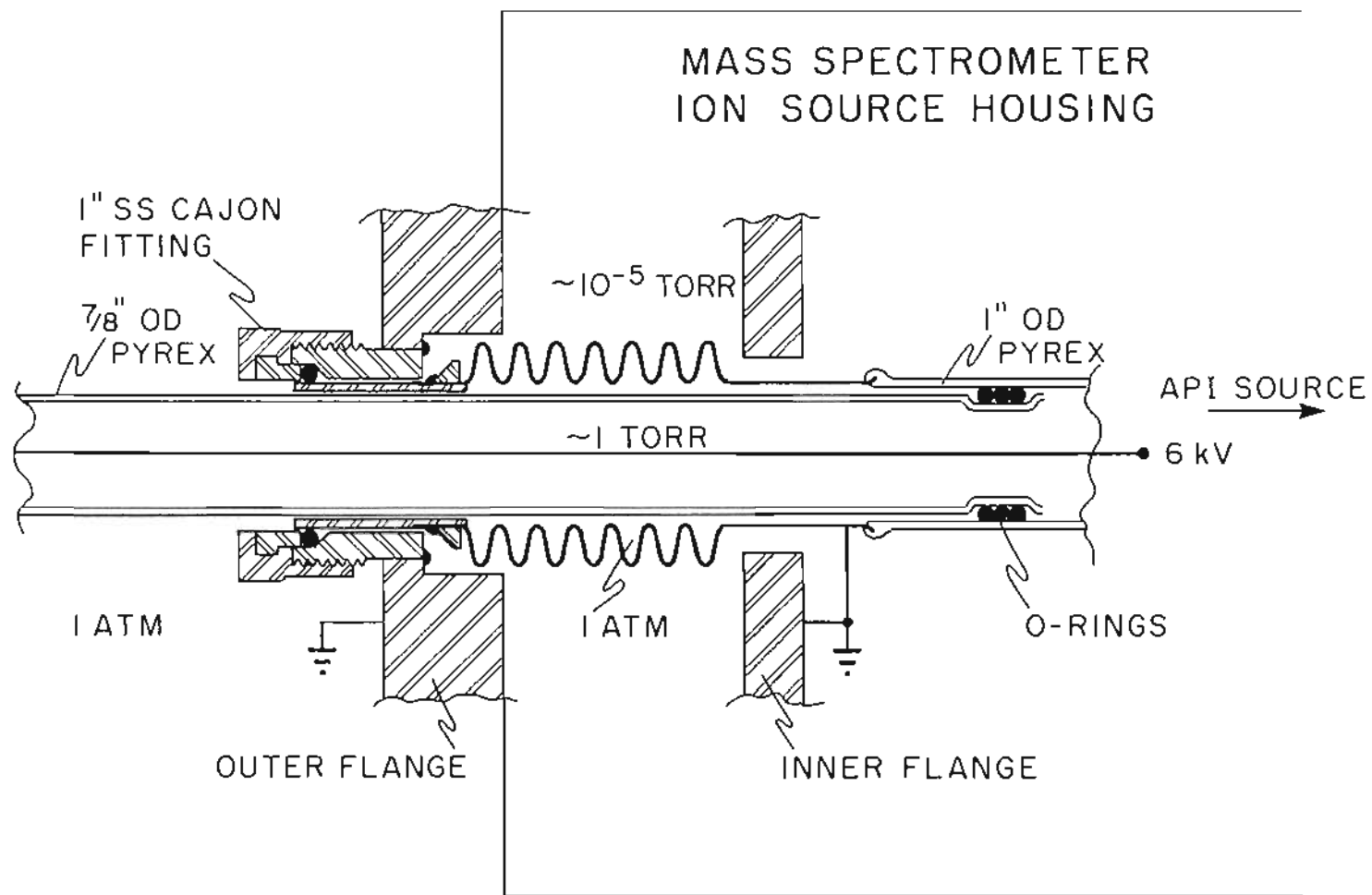


FIGURE II.3. Construction details of the assembly used to isolate the conducting gas exposed to the high source potential from grounded surfaces within the source housing of the mass spectrometer.

### II.1.e) Voltage Supplies

The corona discharge is initiated and maintained by a positive, 15 kV power supply (Bertan Model 602B-150P) modified to provide a constant current; the discharge is monitored with an ammeter (Hickok LX 303 DMM) placed in series with the external high voltage connection to the corona discharge tip. A limiting resistance of 500 M $\Omega$  is also in series with the high voltage connection to the tip in order to protect the circuit from sporadic arcing.

The voltage applied to the end plate of the API source (the 6 kV accelerating potential) and the voltages applied to the half plates of the source lens (focusing and beam centering potentials,  $\sim$ 3 kV) are provided by an independent, positive, 10 kV power supply (Bertan Model 602B-100P), instead of the mass spectrometer's ion source supply, to protect against the unlikely chance of arc-induced damage to the electronics and data acquisition system.

The potential across the CID region is provided by a voltage supply consisting of six 9 V batteries in series and a potentiometer that could be switched across any battery in the string; the high resistance side of the potentiometer is connected to the switch across a 1.5 V battery. The output of this supply could be varied continuously from 0-56 V.

## II.2 SOURCE OPERATION AND PERFORMANCE

### II.2.a) General

For the experiments in Chapter II, except where otherwise indicated, room air admitted into the source through the open inlet port was used

for testing (the limiting conductance is provided by the aperture separating the corona discharge and CID regions). The source is started by switching on the corona discharge power supply to 8-9.5 kV (measured from the discharge tip to ground). Interruption of the ion signal, especially when a new needle tip is used, occurs intermittently for the first few minutes following initiation of the corona discharge; to reduce the time necessary to achieve stable operation, the discharge is run at 1-1.5  $\mu\text{A}$  for about 2 min. Following this conditioning period, the discharge potential is adjusted to produce an average operating current of 0.2  $\mu\text{A}$ . During corona discharge, the needle tips are blunted by sputtering and are replaced when the ion signals become erratic. This effect was found to be minimized by operating at the lowest sustainable corona discharge current for our source (0.2  $\mu\text{A}$ ).

After operating the corona discharge continuously for ~30 min, the discharge current drifts by only  $\pm 0.01 \mu\text{A}$  during the time required to acquire a single mass spectrum (~2 min) and by only  $\pm 0.03 \mu\text{A}$  during periods  $\geq 1$  hr. Peak heights fluctuate by as much as  $\pm 20\%$  (time constant = 0.1 ms); these fluctuations are most pronounced when low corona discharge currents are used. To compensate for the short term variations in ion beam intensities and obtain good average peak areas, which appear as lines after the peaks are centroided by the data acquisition system, all mass spectra were recorded at the slow scan rate of 110 sec per mass decade. The voltage corresponding to an integrated peak area at a particular  $m/z$  ratio is directly proportional to the ion beam intensity at the time during a scan when ions of that  $m/z$  ratio are striking the detector. This voltage will be referred to as the ion

abundance throughout this dissertation. The average lifetime for corona discharge tips operated at 0.2  $\mu\text{A}$  under relatively clean conditions is estimated to be  $\sim 10$  hr. If there is a high level of organic compounds in the sample, deposits form on the corona tip and operation becomes erratic after only a few hours. Corona discharge tips made from iridium wire might have greater lifetimes (43); however, given the ease with which tips can be changed in our source, the short conditioning time required for new tips, and the low cost of sewing needles, the relatively short lifetimes of discharge tips has not been cause for concern.

Comparison tests with 25, 50, 75 and 100  $\mu\text{m}$  apertures revealed that the 50 and 75  $\mu\text{m}$  orifices produced the most intense total ion beams. It was decided to use the 50  $\mu\text{m}$  aperture routinely because of its lower conductance; high conductance is a matter of concern when samples are supplied from finite sources, such as photoreaction chambers. The gas flow through the API source with a well-sealed 50  $\mu\text{m}$  aperture in place is  $18\text{--}21 \text{ cm}^3 \text{ min}^{-1}$ . Clogging of the corona region's aperture by sputtered material has not been observed at the tip-to-orifice distance and low corona currents normally used. On a few occasions, however, particles carried by the sample gas stream have become lodged in the 50  $\mu\text{m}$  orifice. When this occurs, the source is removed and disassembled, the orifice is cleaned using ultrasonification, the source is reassembled and reinserted, and the mass spectrometer source region is re-evacuated, all in less than 30 min. The replacement of corona discharge needles also requires less than 30 min.

When the API source heater is used, very large peaks appear in the mass spectra arising from phthalates, e.g. protonated phthalic anhydride,  $m/z$  149. We attribute the appearance of these peaks to the Vespel components in the source assembly. These parts will be made of Macor or Cu as necessary in a future version of the source.

The alignment provided by the discharge tip assembly, the aperture holders, and the source's locating dowels is so reproducible that only subtle, if any, adjustment of the potentials on the beam centering plates or those that control the  $y$  and  $z$  directions of the beam path in the mass analyzer are required after removal, cleaning, reinsertion, and pump down of the API source (slits set for ~90% of maximum peak height).

#### II.2.b) Dehydration

A set of mass spectra of room air at a relative humidity of  $40 \pm 15\%$  was recorded to observe the effects of the CID region pressure and CID potential on the abundances of hydrated protons formed by reactions 4-6 (Chapter I). CID potentials were varied in 9 V increments from 19 to 55 V for each of three CID pressures, viz. 1.0, 0.7, and 0.4 Torr. For each condition, the five largest peaks in two successive spectra had to agree to within 15% before a spectrum was printed out. For all twelve conditions the mean deviation for the ion abundances for the five largest peaks between successive spectra was 2%. At each pressure the CID potential initially studied was again observed after the other four CID potentials were viewed; for all three CID pressures the average mean deviation for the five largest peaks between the initial and final

spectra was less than 6%. Hence, systematic and random instabilities during data collection were insignificant relative to the trends observed below.

The mass spectra in Figure II.4 illustrate the trends in ion formation and hydrate disaggregation that occur under different extremes of CID pressure and potential. The range of pressures in the CID region was constrained at the low end by sporadic arcing and at the high end by the limited pumping speed of the mass spectrometer's oil diffusion pumps. To eliminate the possibility of sporadic arcing all but the experiment represented in Figure II.4.a were performed using a CID pressure of 1 Torr. Figure II.4.a exhibits a mass spectrum recorded at the lowest settings of CID pressure and CID potential studied; the distribution of hydrated protons ( $m/z = 19, 37, 55, 73, \dots, 235$  corresponding to  $H(H_2O)_n^+$ ,  $1 \leq n \leq 13$ ) clearly shows that the higher order hydrates are abundant under these conditions. Increasing the CID pressure by over a factor of two causes only a minor decrease in the abundances of the higher order hydrates (Figure II.4.b), whereas increasing the CID potential to 55 V, nearly a factor of three, clearly produces marked dehydration of the hydrated protons (Figure II.4.c). Consequently, we use only the CID potential to control dehydration in the CID region.

Figure II.5 shows the relative ion abundances of the first five hydrated protons plotted as a function of potential; the relative ion abundances were computed from tabular listings of the entire set of room air mass spectra. As the potential increases, dehydration becomes more complete, and the larger hydrated protons ( $m/z$  55, 73, and 91) fall in

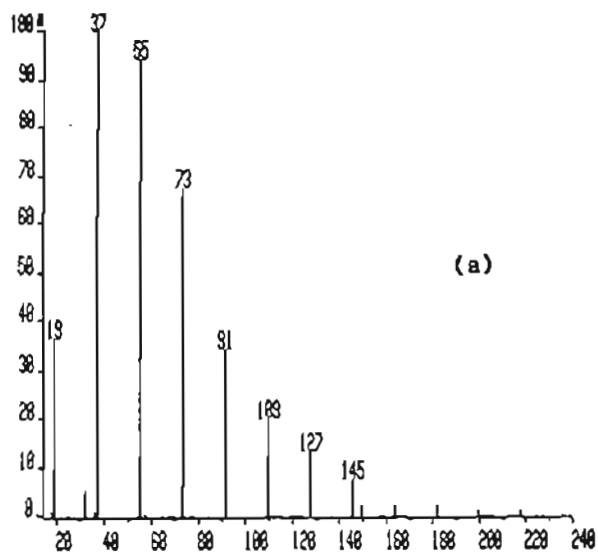
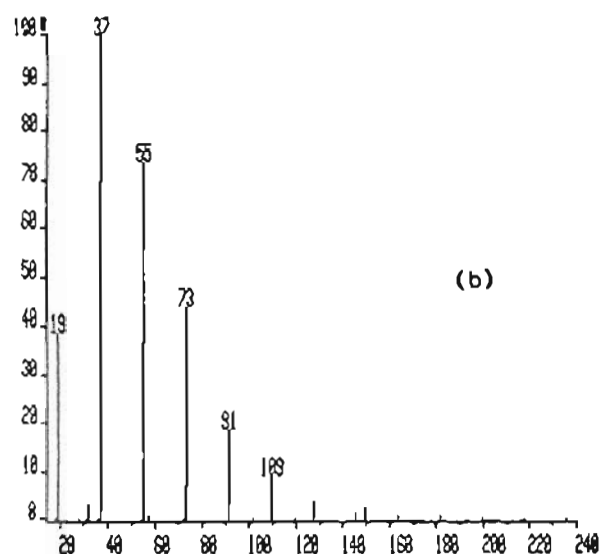
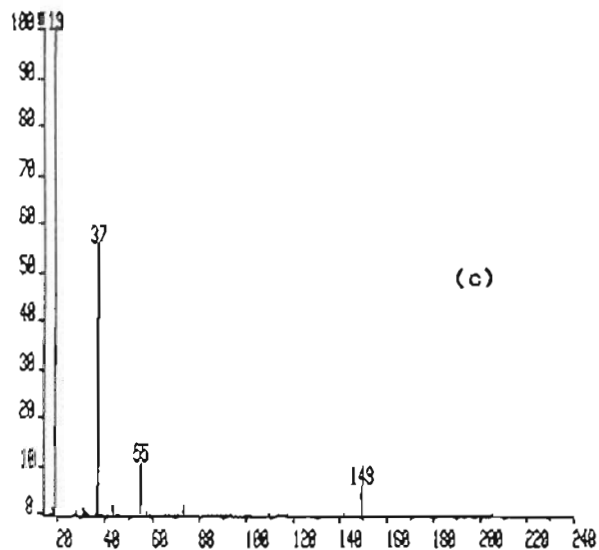


FIGURE II.4.



Mass spectra for room air at  $40 \pm 15\%$  relative humidity. For the spectrum in a) the CID pressure was 0.4 Torr and the CID potential was 19 V; in b) the CID pressure was 1 Torr and the CID potential was 19 V; and in c) the CID pressure was 1 Torr and the CID potential was 55 V. The peak at  $m/z$  149 is due to protonated phthalic anhydride, a fragmented ion produced from phthalates, which are common components of plasticizers (46).





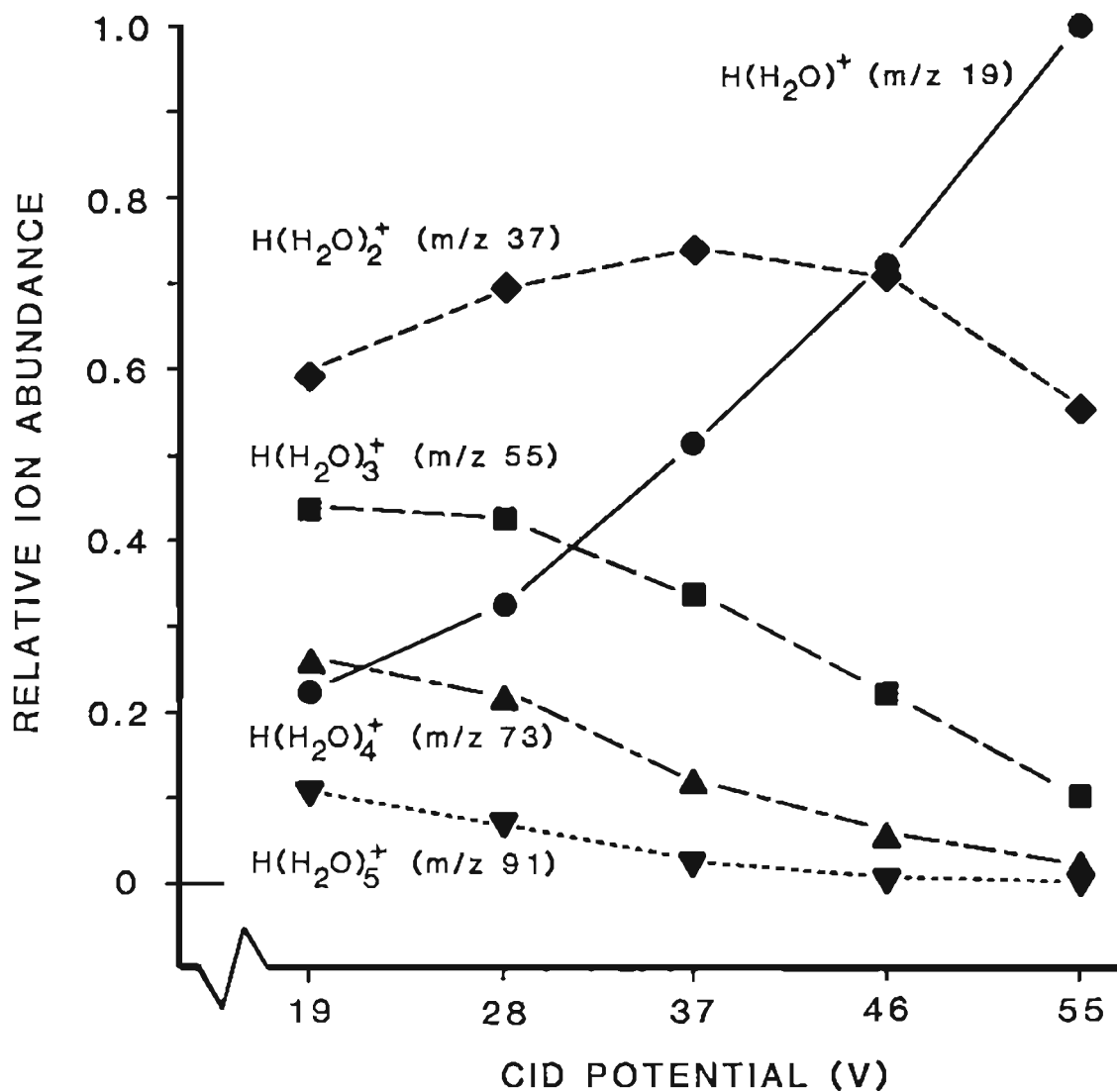


FIGURE II.5. Ion abundance plots of the first five hydrated protons as a function of CID potential with a CID pressure of 1 Torr. Ion abundances are corrected for ion collection efficiency and normalized to the abundance of the m/z 19 ion with 55 V applied across the CID region.

abundance relative to that of the hydronium ion ( $m/z$  19) at 55 V. The abundance of the hydronium ion itself increases steadily up to its maximum at the CID potential of 55 V. The relative abundance of  $H(H_2O)_2^+$  ( $m/z$  37) increases and then falls with increasing CID potential. This behavior reflects the competition between disaggregation of  $H(H_2O)_2^+$  while passing through the CID region and formation of  $H(H_2O)_2^+$  via dehydration of larger hydrated protons. At the highest CID potential spectra are simplest as can be seen by comparing Figure II.4.a with II.4.c

A high concentration of an easily protonated compound in the sampled air can decrease the degree of hydronium ion hydration. This effect is illustrated in Figure II.6 for the case of benzaldehyde vapor; the average number of water molecules associated with each proton is 2.92 in Figure II.6.a and 2.71 in Figure II.6.b. The degree of dehydration is obviously small relative to that induced by increasing the CID potential, and it virtually disappears at low levels of analyte. In the same manner as for the hydrated protons, the abundances of the hydrated, protonated benzaldehyde ions and of the protonated benzaldehyde dimer ion decrease as the CID potential increases.

The effects of diluting samples with dry zero air and of varying pressure in the corona region on the formation of hydrated ions as well as the effect of the CID potential on disaggregating hydrated ions are more completely reported in Chapter III.

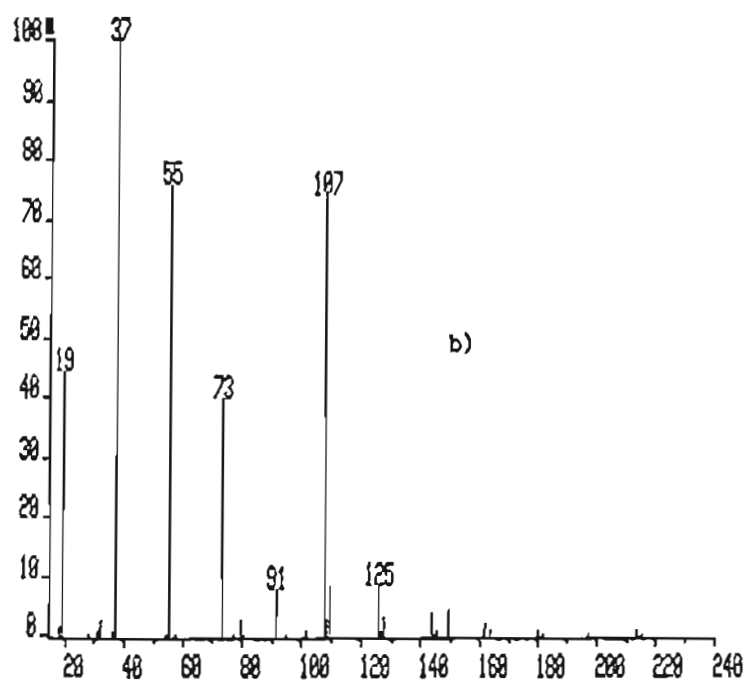
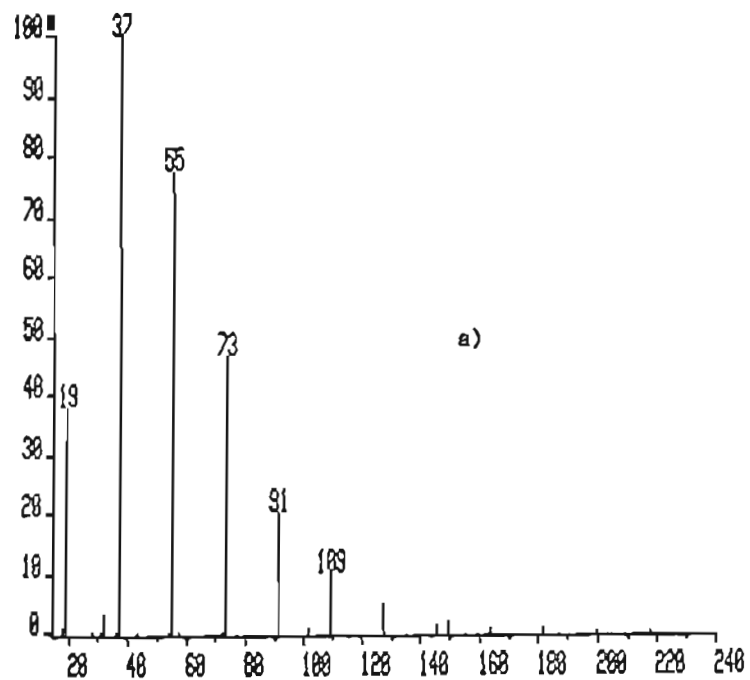


FIGURE II.6. API mass spectra for a) room air, and b) room air with benzaldehyde vapor added. Both spectra were recorded with a CID potential of 19 V and a CID pressure of 1 Torr. The m/z 107 peak is the protonated benzaldehyde ion; the m/z 125, 143, and 161 peaks are hydrated, protonated benzaldehyde ions; and the m/z 213 peak is protonated benzaldehyde dimer.

### II.2.c) Resolution

To determine the resolving power of the API-VG 7070E-HF mass spectrometer operating in the API mode, several mass spectra of various doublets in the vicinity of 100 Daltons were recorded; the scans were taken from high to low mass and were restricted to a range of approximately 5 Daltons. The CID voltage was adjusted to maximize the peak height of the nominal mass being resolved. The base resolution of the instrument, defined as that with the entrance and exit slits of the mass analyzer set to give an ion signal at a given mass to charge ratio equal to ~90% of its maximum, was determined from 10 consecutive scans over the protonated benzaldehyde ions  $^{12}\text{C}_7\text{H}_7\text{O}^+$  and  $^{12}\text{C}_6^{13}\text{CH}_7\text{O}^+$  to be  $1525 \pm 90$  (2s), 10% valley.

A test atmosphere consisting of 1 ppm of pinacolone (3,3-dimethyl-2-butanone), 3 ppm of 2,4-pentanedione, and zero air at a relative humidity of 58% was prepared in a 12 L flask, diluted 1:8 with dry zero air, and introduced into the API source (Chapter III discusses how this is done and the rationale behind these conditions). The CID potential was tuned to 27 V to maximize the molecular ion,  $(\text{M}+\text{H})^+$ , signals. In order to completely separate the two mass peaks at  $m/z$  101, the entrance slit was first narrowed to reduce the ion signal from its maximum by a factor of three, and then the exit slit was narrowed to further reduce the ion signal by an additional factor of two. Figure II.7 is a typical mass spectrum of the fully resolved  $(\text{M}+\text{H})^+$  ions of pinacolone and 2,4-pentanedione. The very large signal to noise ratio clearly indicates that these two species could be separated at much lower concentrations.

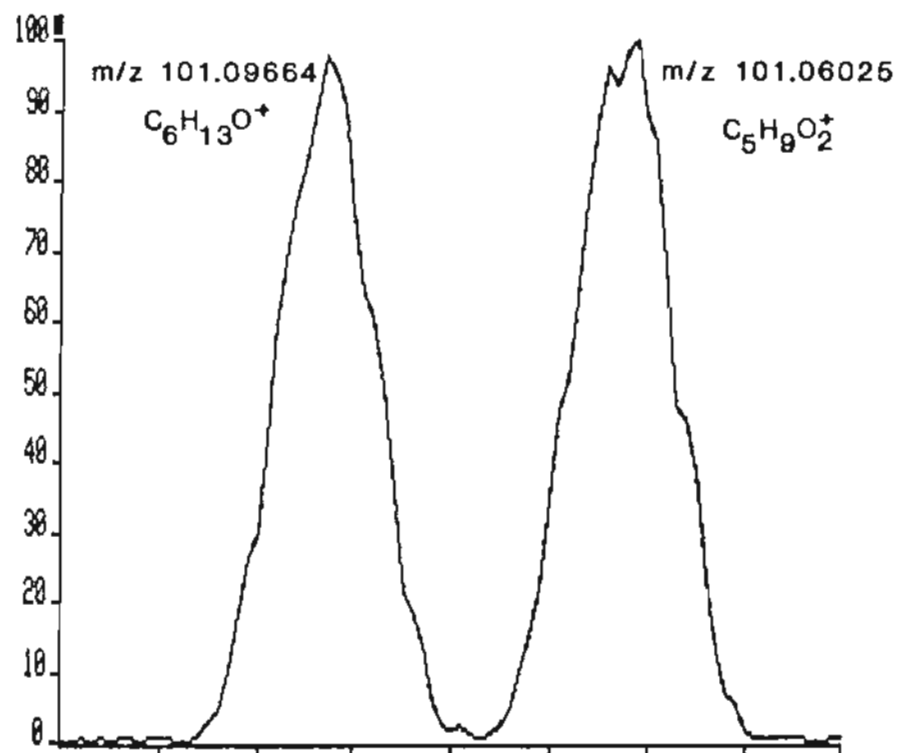


FIGURE II.7. API mass spectrum of pinacolone and 2,4-pentanedione showing full resolution ( $R = 2,800$ ,  $< 0.5\%$  valley) of the protonated molecular ions.

The average valley for 10 successive scans was less than 0.5% above the baseline, and the average ratio of peak heights for the same 10 scans was 1:0.96. Hence, the resolution at one-sixth of the open-slit signal strength is 2,800 ( $101/0.03639$ ).

To estimate the resolution expected with a 50% valley, a copy of Figure II.7 was cut from top-to-bottom through the valley minimum. The two peaks were then moved toward each other until they overlapped at 25% of their full height; this overlap simulates a 50% valley. The distance between the peak maxima is inversely proportional to the resolution ( $R = m/\Delta m$ ). Hence, multiplying the ratio of the interpeak distance before and after moving the peaks times 2,800 provides an estimate of 5,000 for the 50% valley resolution. This performance exceeds our design criterion of 4,100 with a 50% valley (Chapter I) necessary to resolve oxidized hydrocarbons having the same nominal mass, but different molecular formulae. The entrance and exit slits were narrowed similarly for the medium resolution experiments in Chapter VI.

The mass spectrum in Figure II.8 shows the fully resolved doublet at  $m/z$  107 comprised of the xylene radical ion containing one  $^{13}\text{C}$  atom and protonated benzaldehyde. A test atmosphere containing 1 ppm of benzaldehyde was supplied to the API source in the same manner described for the previous doublet. A CID potential of 28 V maximized the benzaldehyde ion signal, and the entrance slit was narrowed to reduce the maximum ion signal to one-fifth before narrowing the exit slit to reduce the remaining signal by one-half. Sensitivity for xylene, which is devoid of heteroatoms, is extremely low. To provide a  $^{13}\text{C}$ -xylene signal, a 0.02  $\mu\text{L}$  droplet was injected into the sample inlet line.

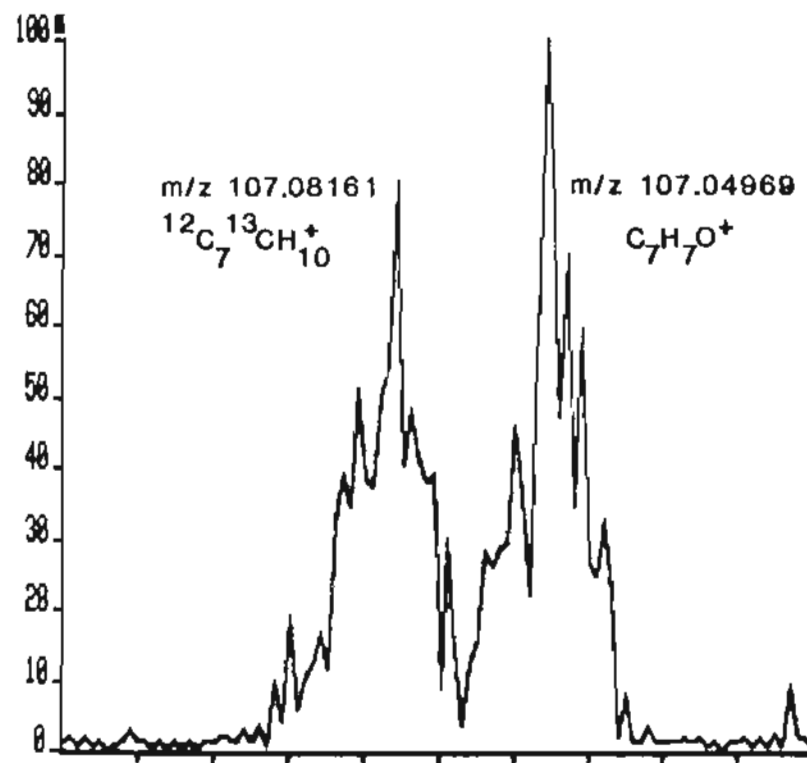


FIGURE II.8. API mass spectrum of the  $^{13}\text{C}$ -xylene radical ion and the protonated benzaldehyde ion showing full resolution ( $R = 3,300$ ,  $< 0.5\%$  valley) of the two peaks.

The resulting saturation of the xylene response provided a large  $^{13}\text{C}$ -xylene signal but caused the benzaldehyde ion abundance to fall by over 96%. As the drop evaporated, both peaks became equal in height at about 15% of the original benzaldehyde signal. The lower ion abundances account for the greater noise observed in Figure II.8 relative to Figure II.7. The average valley determined from 10 spectra (two each after five separate injections of xylene) was less than 0.5%; thus, the resolution at one-tenth of the open-slit signal strength is 3,300 ( $107/0.03192$ ).

Toluene was admitted into the system in an unsuccessful attempt to separate the tropylium ion,  $\text{C}_7\text{H}_7^+$  ( $m/z$  91.05478) from the hydrated proton,  $\text{H}(\text{H}_2\text{O})_5^+$  ( $m/z$  91.06065), a task requiring a resolution of  $\sim 15,500$ . For this test, the entrance slit was narrowed to allow transmission of one-tenth of the maximum signal; the remaining signal was successively halved by the exit slit and the two  $z$  restrictors in the flight tube leaving the signal at  $\sim 1\%$  of its maximum. The width of toluene's molecular ion peak at  $m/z$  92 was determined from the time-based units provided by the data acquisition system to be 0.019 Daltons 5% above the baseline corresponding to a resolution of  $\sim 4,800$  ( $92/0.019$ ) with a 10% valley. We know of no other instrument that has this resolving capability while operating in the API mode.



## CHAPTER III

MANIPULATION OF OPERATING CONDITIONS TO SIMPLIFY MASS SPECTRA,  
TO OPTIMIZE SENSITIVITY, AND TO DIFFERENTIATE BETWEEN  
MOLECULAR, HYDRATED, AND FRAGMENTED IONS

## III.1. INTRODUCTION

In Chapter I the problem of hydrated ion formation was discussed. The appearance of several ion peaks for each compound in a sample gas containing numerous components would provide spectra difficult to interpret and decrease sensitivity for each analyte. In this chapter manipulation of the number density of water molecules in the corona region by variation of the relative humidity of the sample gas and of the pressure in the corona region are used to suppress the formation of hydrated analyte ion peaks. Also demonstrated is manipulation of the collisionally induced dissociation (CID) potential to disaggregate hydrated ions formed before entering the CID region and to differentiate between molecular, hydrated, and fragmented ions in the spectra produced by the instrument.

## III.2. EXPERIMENTAL SECTION

## III.2.a) Flow System

The apparatus used to supply sample gas to the API source is shown in Figure III.1. All procedures pertaining to preparation, treatment,

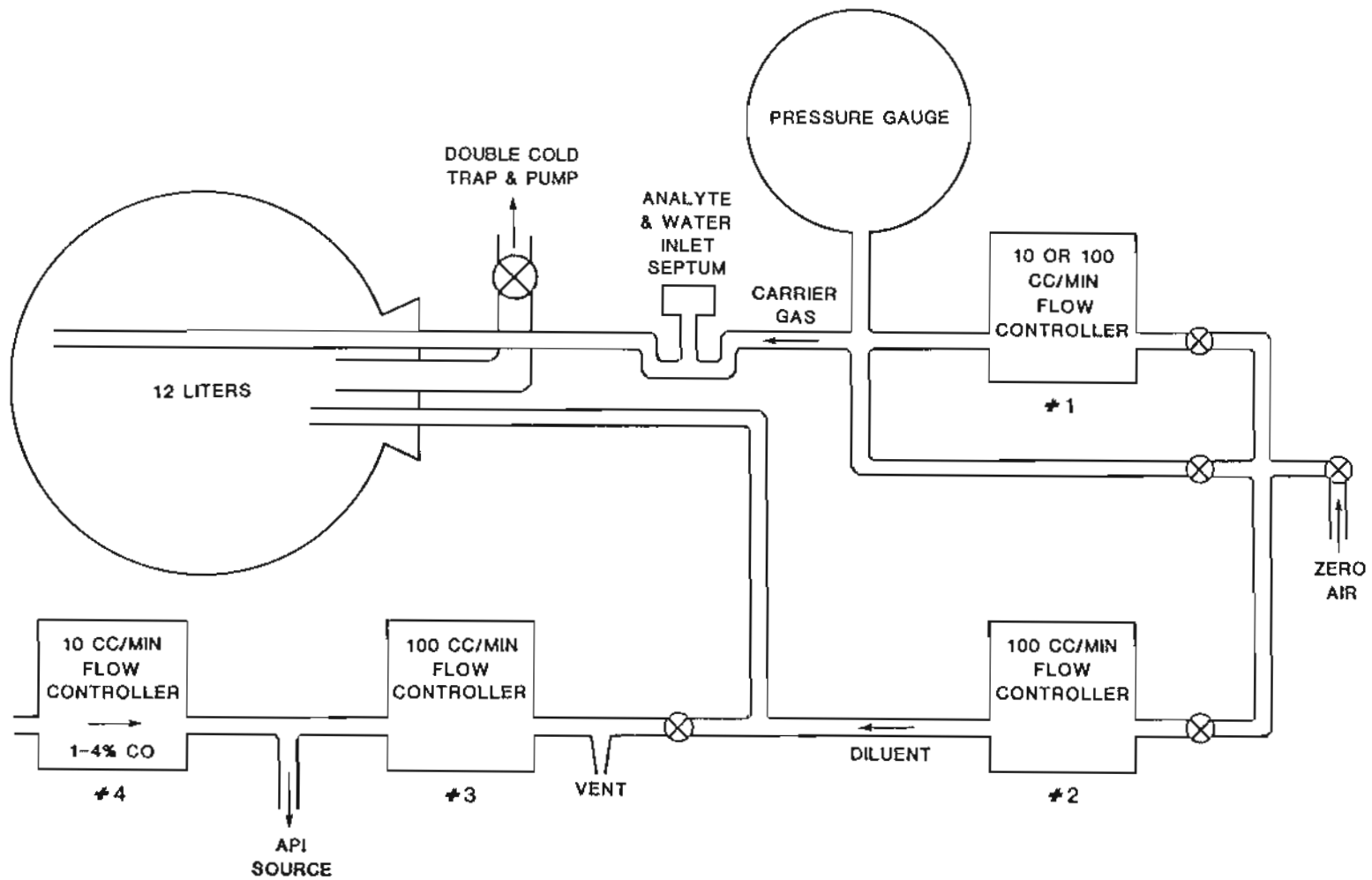


FIGURE III.1. Diagram of the 12 L reservoir and flow system used to supply sample gas to the API source. The functions of the four flow controllers are described in the text.

and supply of sample gas are described below with reference to this figure. Tylan model FC 260 flow controllers were used at all points indicated in the diagram; the controllers were calibrated against a soap film flowmeter to an accuracy of  $\pm 5\%$  over the upper 90% of their flow range. Calibration factors were used when a flowmeter was used in the lowest 10% of its range (flow controller #4 only).

During operation of the mass spectrometer, zero air, delivered through flow controller #1 in Figure III.1, was used to drive the test atmosphere from the reservoir into the API source. The relative humidity was corrected as necessary for the constant addition of zero air to the sample reservoir.

Besides this inherent dilution, the sample gas was systematically diluted en route to the API source with dry zero air using controller #2. In order to maintain atmospheric pressure in the sample reservoir without contaminating the sample gas with room air, approximately  $2 \text{ cm}^3 \text{ min}^{-1}$  of gas was allowed to escape from the system through a vent located just beyond the valve after the mixing junction.

The pressure in the corona region was determined primarily by the setting of flow controller #3 and by the conductance of the  $50 \mu\text{m}$  orifice. When studying the first test atmosphere, the orifice was held in place by a worn inner orifice holder, and a gas flow through the source of  $24\text{-}25 \text{ cm}^3 \text{ min}^{-1}$  was required to maintain a pressure of 1 atm in the corona region. The flow required decreased to  $19\text{-}20 \text{ cm}^3 \text{ min}^{-1}$  after installing a newly machined inner orifice holder before preparation of the second test atmosphere. Lower corona pressures were achieved by restricting the flow of gas through controller #3, but the

pressure in the CID region was maintained at 1 Torr by adjusting a needle valve (Appendix A). A constant CID pressure is necessary because it is another variable that alters the degree of hydration and fragmentation seen in the ion spectra (Chapter II), albeit to a lesser extent than the other variables discussed in this chapter.

Sufficient CO to provide 1% CO in the API source was supplied from a regulated cylinder through controller #4 to the ion source inlet stream. The CO was introduced to scavenge hydroxyl radicals formed simultaneously with the hydrated protons in the API source (Chapter IV) and, thus, to prevent their attack on analytes. The 1% concentration was set just above the flow controller's lower limit of regulation (-0.7%) in order to retain a modicum of adjustment.

The artificial atmosphere was fed to the API source through a 6 ft line of 1/4 in. pyrex tubing; a heating tape was used to keep the line at  $-70^{\circ}\text{C}$  to suppress adsorption of the analytes on the tubing walls. This latter measure was taken to prevent major loss of sample, no attempt was made to eliminate sample loss due to adsorption on the walls of the sample reservoir, the shorter lengths of unheated glass, the metal surfaces in the gas lines, and the unheated API source.

### III.2.b) Test Atmospheres

The experiments reported in this chapter were conducted with two artificial test atmospheres: 1) 36 ppm methanol, 190 ppm toluene, and 1.4 ppm benzaldehyde at a nominal relative humidity of 58% and 2) these same three analytes at 10% of the concentrations in 1). The spectra shown in this chapter were recorded with the higher analyte

concentrations in the reservoir 1) to ensure large signal-to-noise ratios, thereby avoiding the possibility of confusing analyte related mass peaks with those due to low level contaminants, and 2) to ensure both analyte ion peaks and hydrated proton peaks have significant amplitudes using the same amplifier scale, thereby avoiding amplifier saturation for the largest hydrated proton peaks when the optimum range for analyte peaks is used. Use of high analyte concentrations could result in saturation by the analyte molecules (47) at low relative humidities, whereas lower concentrations of analytes, more characteristic of those to be used in photooxidation experiments might not; the second atmosphere was used to check for such errors.

The first test atmosphere was produced in the following manner. The sample reservoir, a 12 L pyrex flask, and its associated flow lines were evacuated through a double cold trap to  $\sim 10^{-2}$  Torr (measured at the pump), backfilled with dry zero air (AirCo Grade 0.1) from a pressurized tank through a two stage, stainless steel regulator (Victor Model HPT 270 B) and an unmeasured bypass line (Figure III.1), and re-evacuated to  $\sim 10^{-2}$  Torr. Following the re-evacuation, backfilling of the reservoir with dry zero air was started through the unmeasured bypass line. Before the pressure reached 0.1 atm, 0.8  $\mu$ L of methanol, 10.8  $\mu$ L of toluene, 0.08  $\mu$ L of benzaldehyde, and 150  $\mu$ L of water were injected through the septum into the zero air stream entering the reservoir. The glass U-tube at the base of the septum-inlet was gently warmed during backfilling to help vaporize the injected liquids. When the pressure reached 1 atm, the zero air supply was shut off, and the system was allowed to equilibrate overnight. The second test atmosphere was

prepared by the same method except that only 10% as much of the three analytes was added to the flask. The smallest syringe available had a capacity of 1  $\mu\text{L}$ . To add only 0.008  $\mu\text{L}$  of benzaldehyde, 1.1  $\mu\text{L}$  of a solution of 3.6  $\mu\text{L}$  of benzaldehyde in 0.5 mL of toluene was injected through the inlet-septum (two injections of 0.5 and 0.6  $\mu\text{L}$ ).

### III.2.c) Determination of the Relative Humidity

An optical condensation, dewpoint hygrometer (General Eastern, model 1100DP) was used to measure the relative humidity of gas driven from the reservoir through the hygrometer with dry zero air. Because a flow of 200  $\text{cm}^3 \text{min}^{-1}$  was required for this measurement, it could not be made routinely, since this flow is -10 times that required by the API source and rapidly depletes the reservoir contents. After preparing a test atmosphere as described above, but with only water added, dew point temperatures were recorded every 30 sec for 30 minutes. The corresponding relative humidities, corrected for dilution by the carrier gas (Appendix B), increased from 58% after 3 minutes to 61% after 30 minutes. These measurements indicate two things. First, adsorption of water onto surfaces does not decrease the relative humidity in the reservoir, since 150 mL of water is necessary to provide 12 L of gas having a relative humidity of 58% at 22°C, the temperature at which the experiment was performed. Secondly, corrections made for dilution in the reservoir with time are reasonable; the corrected relative humidity was only 5% high after one-half of the reservoir volume had been replaced. The 10-fold greater mixing time available at the lower flows normally used ensures that errors due to any concentration

inhomogeneities within the reservoir would be less important than in this experiment.

#### III.2.d) Mass Spectrometer

All API mass spectrometry was performed on the VG 7070E-HF double focusing instrument at the Oregon Graduate Center using the corona discharge, API source described in Chapter II operating at an accelerating potential of 6 kV. The mass spectra discussed in this chapter were recorded using a corona current of 0.2  $\mu$ A; this was the smallest current capable of maintaining the discharge. Use of a small corona current minimizes corona tip erosion (Chapter II) and interfering chemistry in the source (Chapter IV).

The potential across the CID region (Figure III.2) was provided by the voltage supply described in Chapter I. Although the output of this supply could be varied continuously from 0-56 V, it was found sufficient in this study to simply vary it in 9 V increments.

In order to obtain good average peak areas, which are plotted as lines after the peaks are centroided by the data acquisition system, all mass spectra were obtained at the relatively slow rate of one mass decade in 3 min. Each mass spectrum was recorded from 218 to 18 Daltons with the slits set to provide ~90% of the ion signal obtained with the slits fully open. For all mass spectra recorded, the analyzer was scanned until the variation in peak areas at  $m/z$  33, 92, and 107 in at least two successive mass spectra was less than 15%.

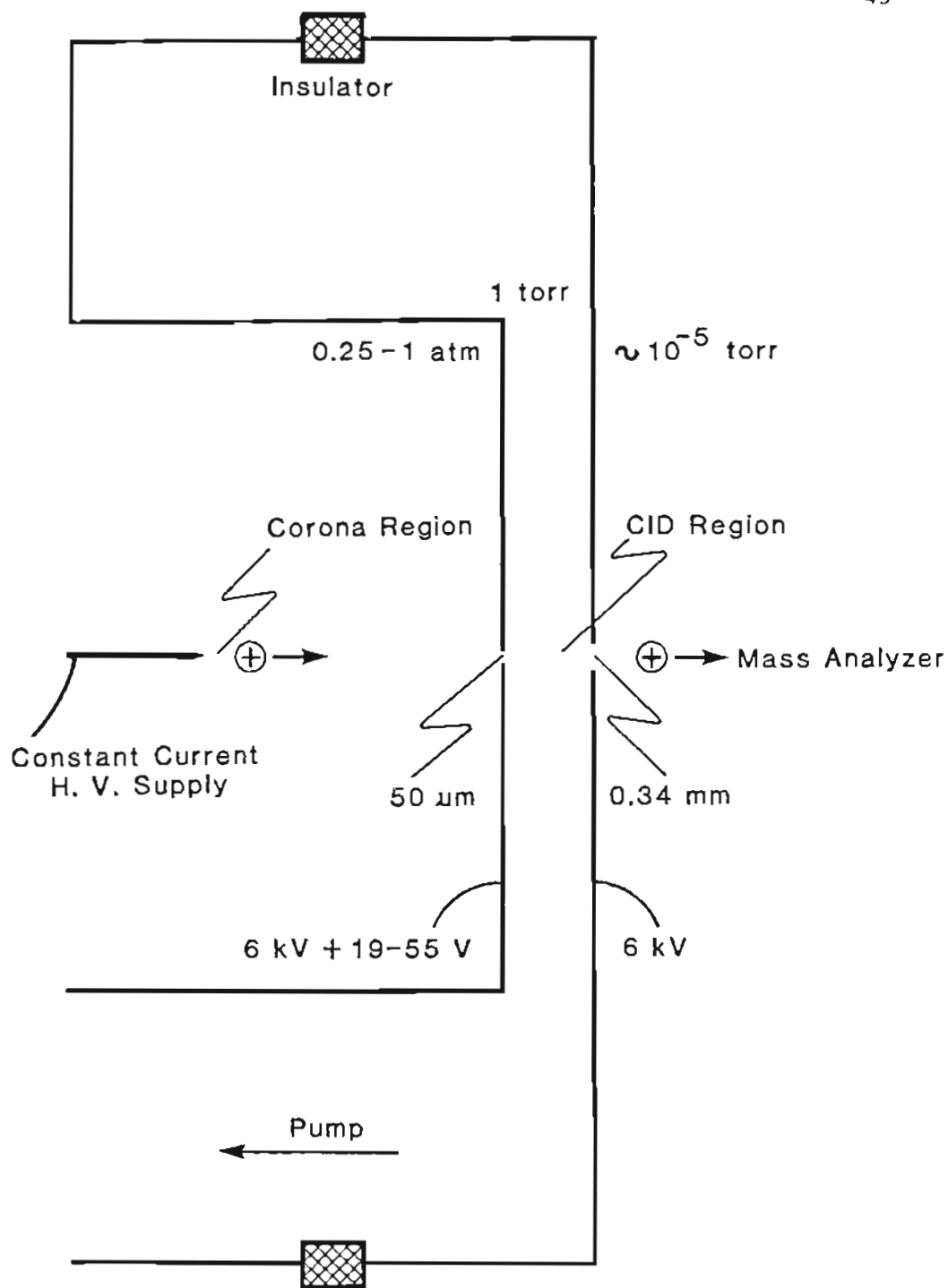


FIGURE III.2. Schematic diagram of our API source illustrating the corona and CID regions, the pressures in these regions, and the potential applied across the CID region.



### III.3 RESULTS AND DISCUSSION

#### III.3.a) Reproducibility of Mass Spectra

The data recorded for the more concentrated test atmosphere is presented in two arrays of mass spectra: a 5x5 array for which both the CID potential and the dilution ratio (relative humidity) were changed and a 3x4 array for which both the CID potential and the corona region pressure were varied.

For the first array at a given dilution ratio spectra were recorded over a 19 V to 55 V range in 9 V increments. No usable ion spectra could be obtained much below 19 V, presumably because no ions reached the mass analyzer. For each relative humidity, a second series of 19-55 V mass spectra was taken immediately after recording the first set. Mean deviations were determined for the five largest mass peaks in each pair of spectra for the same source conditions; the grand mean deviation for all 25 sets of spectra, 125 comparisons in total, was 6.6%. No significant systematic increase or decrease in peak areas over time was observed indicating that any adsorption of the analytes and water on the walls of the reservoir, the gas lines, and the API source had reached equilibrium before data were recorded at each dilution ratio. Relative to this reproducibility and stability, the trends observed in the array as a result of varying the CID potential or the relative humidity are statistically significant.

In the second array for each corona pressure, mass spectra were recorded in similar fashion over a 27 V to 46 V range of CID potentials; no mass spectra could be produced at pressures less than 0.25 atm, or at

0.25 atm with only 19 V across the CID region; hence, a narrower range of CID potentials was used. The narrower range also limited the change in relative humidity (2.5%) that occurred during the experiment. The grand mean deviation for comparisons of the five largest peaks under the twelve sets of conditions was 3.0% and again, no systematic change in ion abundances was observed. Hence, the trends observed in this array are also statistically significant.

For the less concentrated test atmosphere a 4x4 array of mass spectra was recorded over a range of CID potentials from 28 V to 55 V (again in 9 V increments) at the same dilution ratios studied with the first test atmosphere. A spectrum was also recorded at a CID potential of 19 V for a reservoir gas/diluent ratio of 1:8. The amplifier range used was 25 times more sensitive in order to obtain significant signals for the analytes. This caused clipping of the peaks for hydrated protons with  $m/z$  19 and 37 in all spectra and with  $m/z$  55 in many spectra. Duplicate spectra for each dilution ratio were collected only for the 28 V CID potential, before and after spectra were recorded for the higher CID potentials. The grand mean deviation for the peaks due to the three analytes for the duplicate spectra was 4.7%. Hence, reproducibility was consistent with that for the more concentrated atmosphere.

### III.3.b) Manipulation of the Relative Humidity and the CID Potential

Figure III.3.a is a subset of mass spectra, taken from the 5x5 array in Figure III.3.b, of the more concentrated methanol-toluene-benzaldehyde test atmosphere recorded with a corona region pressure of 1 atm.

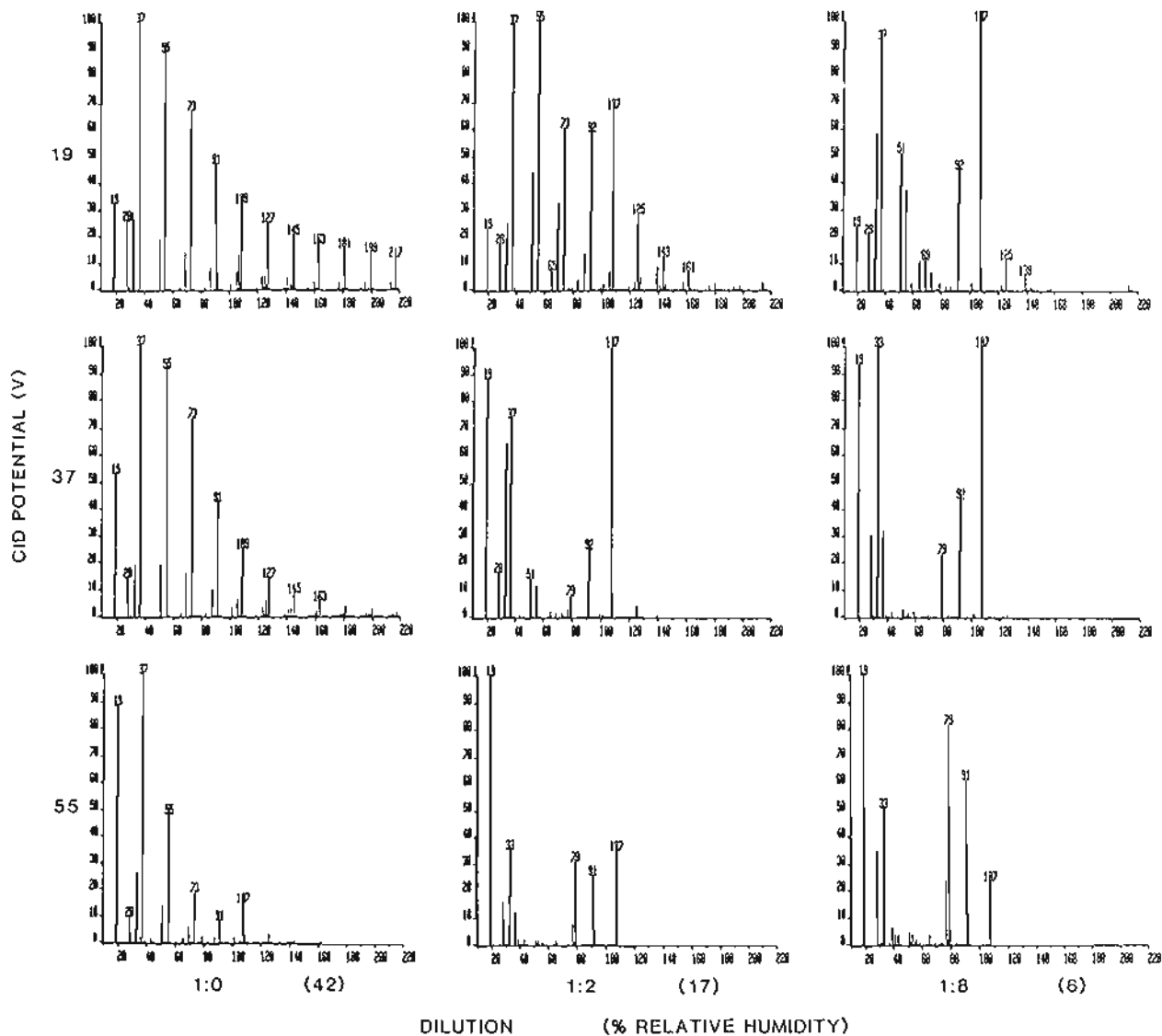


FIGURE III.3.a)

A 3x3 array of mass spectra taken from a 5x5 array displaying the dependencies of the spectra on the CID potential along the y axis and of the dilution ratio (relative humidity) along the x axis. The test atmosphere contained 36 ppm of methanol, 190 ppm of toluene, and 1.4 ppm of benzaldehyde.

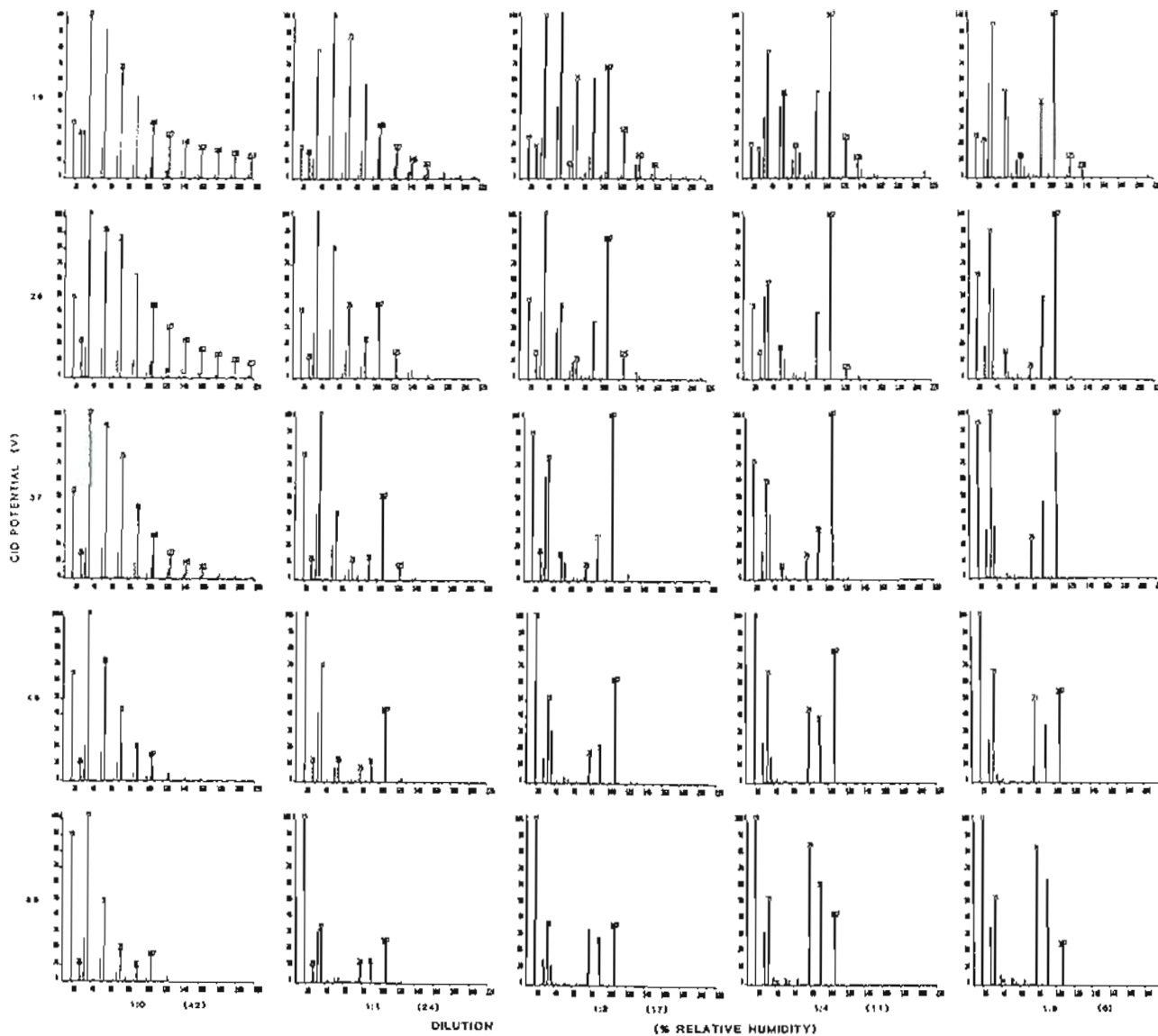


FIGURE III.3.b)

A 5x5 array of mass spectra displaying the dependencies of the spectra on the CID potential along the y axis and of the dilution ratio (relative humidity) along the x axis. The test atmosphere contained 36 ppm of methanol, 190 ppm of toluene, and 1.4 ppm of benzaldehyde.

The trends to be discussed are readily apparent in the abridged array in which the  $m/z$  labels of the peaks are easier to read. The spectra are arranged vertically according to the CID voltage and horizontally according to the relative humidity of the test atmosphere during recording. The mass peaks in each spectrum in Figures III.3.a and III.3.b (and Figure III.4) are normalized with respect to that spectrum's base peak.

Apparent inconsistency between the relative humidities and the test atmosphere/diluent ratios given in Figures III.3.a and III.3.b is caused by dilution of the contents of the sample reservoir with carrier gas during the experiment. The order in which the data was collected, low to high relative humidity, resulted in the actual relative humidities (viz. 6%, 11%, 17%, 24%, and 42%) being progressively lower than those that would have resulted from diluting the original test atmosphere (58% R.H.) by the indicated ratios. The analyte concentrations present in the flask were also diluted; the concentration of a given analyte was proportional to the dilution in relative humidity, i.e. concentration = initial concentration  $\times$  (relative humidity / 58%). For the second test atmosphere the range of relative humidities was 6% to 49%.

The mass peaks at  $m/z$  33 and 107 arise respectively from protonated methanol and benzaldehyde; the mass peak at  $m/z$  92 corresponds to the molecular ion for toluene,  $C_7H_8^+$ , which is formed via charge transfer. Hydrated protons appear at  $m/z$  19, 37, 55, ..., 217.

The array of mass spectra in Figure III.3.a graphically illustrates the behavior of hydrated, fragmented, and molecular ions as functions of

the CID potential and of the relative humidity. Increasing the CID potential independently of the relative humidity, i.e. moving downward in any column, decreases both the abundances of the hydrated hydronium ions,  $\text{H}(\text{H}_2\text{O})_n^+$  for  $n \geq 2$  ( $m/z$  37, 55, 73, ..., 217), relative to the hydronium ion ( $m/z$  19), and the average aggregation number,  $n$ , of the hydrates; conversely, the relative abundance of the hydronium ion increases. Similarly, the mass peaks corresponding to series of hydrated ions of benzaldehyde,  $\text{C}_7\text{H}_7\text{O}(\text{H}_2\text{O})_n^+$  for  $n \geq 1$  ( $m/z$  125, 143, ..., and 197), and of methanol,  $\text{MeOH}_2(\text{H}_2\text{O})_n^+$  for  $n \geq 1$  ( $m/z$  51, 69, 87 and 105), easily observed at 19 V and 17% relative humidity, disappear, while the prominence of the mass peaks corresponding to the molecular ions at  $m/z$  107 and 33 increase with increasing CID potential up to 37 V. As the CID potential increases, the kinetic energy of collisions in the CID region increases; more effective disaggregation of hydrated ions results.

In the middle column in Figure III.3.a, as the CID potential is increased, both the  $m/z$  92 peak and hydrated, protonated analyte peaks shrink; but the lack of a shrinking series of hydrated ions related to the  $m/z$  92 ion and the lack of growth in a peak some multiple of 18 Daltons lower in mass in the spectra allows one to rule out this peak as a hydrated ion.

The peak at  $m/z$  79 corresponds to a fragmented ion formed from benzaldehyde. Irrespective of the relative humidity, the peak at  $m/z$  79 grows relative to the parent peak at  $m/z$  107 as the CID potential is increased; the effect is so pronounced at the lowest relative humidity that for a CID potential of 55 V the relative abundance of the

fragmented ion is greater than that of the parent ion. At higher CID potentials more energetic collisions fragment a greater fraction of the parent ions. Peaks that grow with increasing CID voltage as parent ion abundances decrease are due to fragmented ions; such growth by the peak at  $m/z$  77 indicates it also corresponds to a fragmented ion.

In complex spectra a nominal mass peak can result from contributions by two ions exhibiting opposite trends. The peak at  $m/z$  91 is due to ion signals from both the  $\text{H}(\text{H}_2\text{O})_5^+$  hydrated proton and the tropylium ion ( $\text{C}_7\text{H}_7^+$ ) formed from toluene. Consequently, the ion signal at  $m/z$  91 can be a nonmonotonic function of the CID potential. As the CID voltage increases at a relative humidity of 17%, the peak ratio  $[\text{m}/z\ 91]/[\text{m}/z\ 92]$  first decreases as the contribution from the hydrated proton ion diminishes (this is more obvious in the intervening 28 V spectrum in Figure III.3.b) and then increases as the contribution from the toluene fragment becomes more significant. Since a resolution of 15,500 would be required, these peaks cannot be separated with our instrument or, for that matter, with any other known API mass spectrometer. Proper choice of operating conditions, however, can ensure that only one ion contributes significantly to the  $m/z$  91 ion signal; at high relative humidity and low CID potential the hydrated proton ion is predominantly responsible for the ion signal, while at low relative humidity and high CID potential the tropylium ion dominates.

The above trends were also seen in the mass spectra obtained for the more dilute test atmosphere.

In Figure III.3.a the disaggregation of hydrates that occurs when the CID potential is increased at constant relative humidity is also

observed when the relative humidity is decreased for a fixed CID potential (moving from left to right across any row). For both test atmospheres the larger hydrated proton peaks become less prominent in the spectra as the relative humidity within the corona region decreases. The ratio of the abundances of hydrated analyte ions relative to the abundance of their bare analyte ions also falls. The decreasing number density of water molecules shifts the equilibria for hydrated proton formation (reactions 4-6) to the left. The distribution of hydrated analyte ions in the corona region is likewise shifted toward smaller hydrates (reaction 9) as the relative humidity is reduced. Less hydration of ions during adiabatic expansion also causes smaller hydrated ions to enter the CID region. The mass spectra reflect these trends.

Growth in the abundances of the fragmented ions, relative to those for their respective parent ions, as the relative humidity decreases at a fixed CID potential is quite evident in Figure III.3.a; it was not as obvious in the mass spectra recorded for the less concentrated atmosphere. Although this trend is more tenuous than the others cited, it can be explained by assuming that hydrated molecular ions are able to dissipate collisional energy accumulated through multiple collisions in the CID region by shedding water molecules before gaining energy sufficient for fragmentation. Because bare analyte ions cannot dissipate energy in this manner, they are more likely to fragment while traversing the CID region. Hence, the reduction in the average size of the hydrated analyte ions entering the CID region that accompanies the reduction in the relative humidity results in a greater fraction of the analyte ions being fragmented.



### III.3.c) Manipulation of the Corona Region Pressure and CID Potential

Figure III.4 is a 3x4 array of mass spectra, which shows the effects of varying the pressure in the corona region at CID potentials of 28, 37, and 46 V respectively, using sample gas (driven from the reservoir without additional dilution) having a relative humidity of ~27%. As the flow into the API source was reduced to lower the pressure in the corona region, it was impossible to maintain the CO level at 1%; consequently, without adjustment of the flow controller, the CO concentrations were 1%, 1.3%, 2%, and 4% respectively, at corona pressures of 1 atm, 0.75 atm, 0.5 atm, and 0.25 atm. This change in sample gas composition had no obvious effect on the spectra obtained.

Reducing the pressure in the corona region has essentially the same qualitative effect as reducing the relative humidity; i.e. the average size and numbers of hydrated hydronium ions and of hydrated molecular ions from benzaldehyde and methanol decline. Hence, reducing the number density of water molecules by either method accomplishes dehydration. The dehydration and fragmentation trends observed in Figures III.3.a and III.3.b with increasing CID potential are also observed in Figure III.4.

### III.3.d) A Contrast Between Toluene and Protonatable Analytes

The ratios of the ion abundances for methanol, toluene, and benzaldehyde at a CID potential of 28 V, a relative humidity of ~27%, and a corona region pressure of 0.25 atm to those at the same CID potential, a relative humidity of 11%, and a corona region pressure of 1 atm were 1.05, 2.26, and 0.78 respectively. The ratios indicate the two

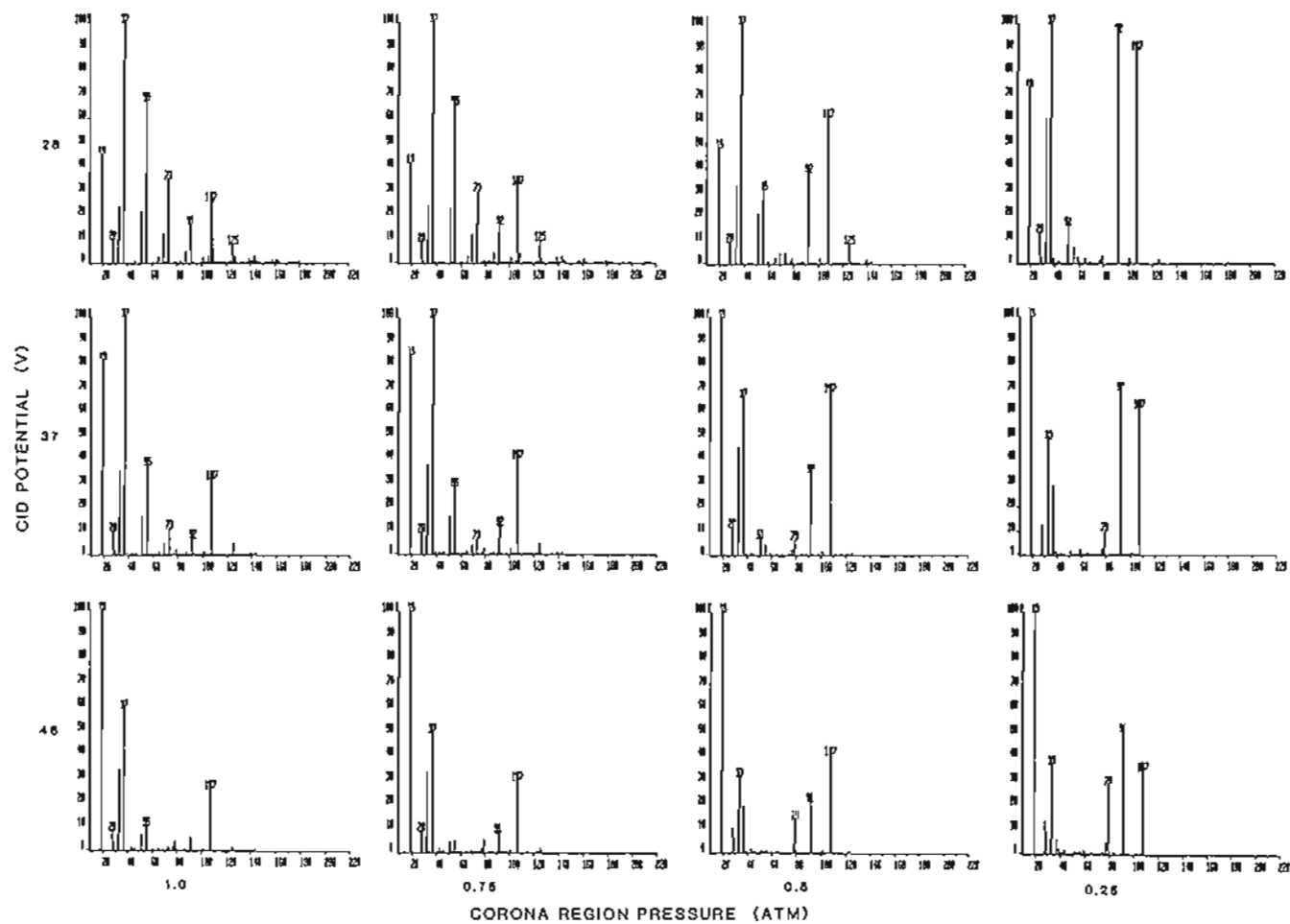


FIGURE III.4. A 3x4 array of mass spectra displaying the dependencies of the spectra on the CID potential along the y axis and of the corona region pressure along the x axis. The test atmosphere contained 36 ppm of methanol, 190 ppm of toluene, and 1.4 ppm of benzaldehyde.

sets of conditions provide similar abundances of protonated ions. Dehydration is essentially complete for both sets of conditions. Sensitivity toward toluene, however, is enhanced to a greater degree relative to protonatable analytes by reduction of the ion source pressure than by reduction of the relative humidity.

The relatively large ion abundance ratio for toluene suggests comparisons of mass spectra obtained at lower relative humidity to those obtained at reduced corona region pressure could possibly be used to differentiate between protonated and charge transfer ions.

### III.3.e) Relative Ion Abundances

In addition to being able to suppress or enhance the ion signals due to hydrates and fragments relative to those due to the molecular ions, it is important for purposes of quantification or identification of scant components in a mixture that the signal strengths of the molecular ions be maximized. Figures III.5.a, III.5.b, III.6.a, III.6.b, and III.7 display plots of the ion abundances of the three analyte ions, the benzaldehyde fragment at  $m/z$  79, and the hydrated proton at  $m/z$  55, vs one of the three variables manipulated in this study; the values of the two constant variables are labeled in each plot. Data were taken from the tabular printouts of the two arrays of mass spectra for the more concentrated test atmosphere. In these figures the abundance-values corresponding to a given ionic species were normalized to the largest value observed within the five figures; this normalization procedure allows comparison of ion abundances between the sets of conditions illustrated in the plots.

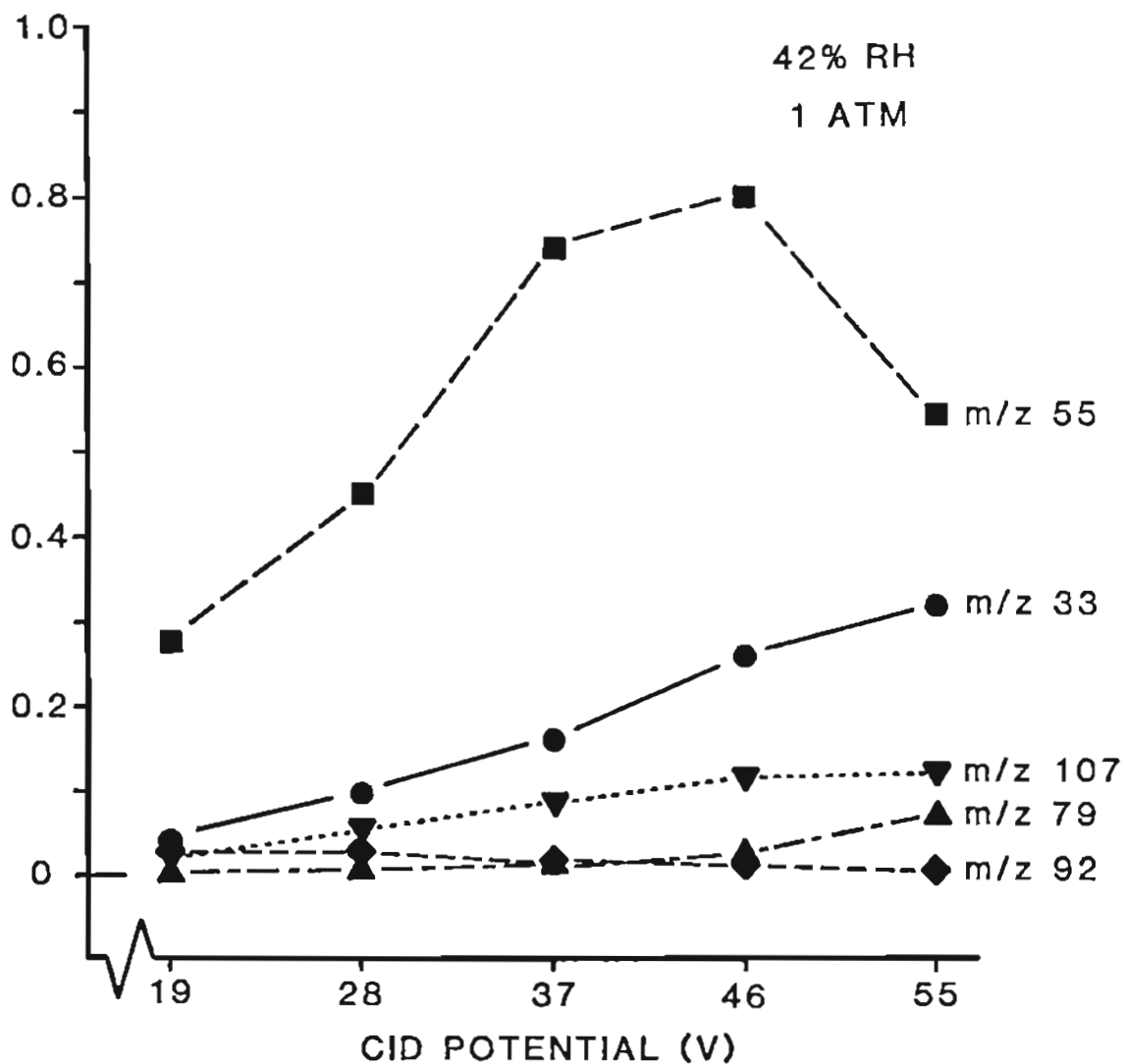


FIGURE III.5.a) Ion abundance plots of five ions vs the CID potential with a corona region pressure of 1 atm and a relative humidity of 42%. For each ion the abundances are normalized to the largest value obtained for that ion in the data used to plot Figures III.5 through III.7. The ions are: m/z 33, protonated methanol; m/z 55, hydrated proton,  $H(H_2O)_3^+$ ; m/z 79, fragmented ion of benzaldehyde; m/z 92, charge transfer ion of toluene; and m/z 107, protonated benzaldehyde. This data was recorded using the more concentrated test atmosphere.

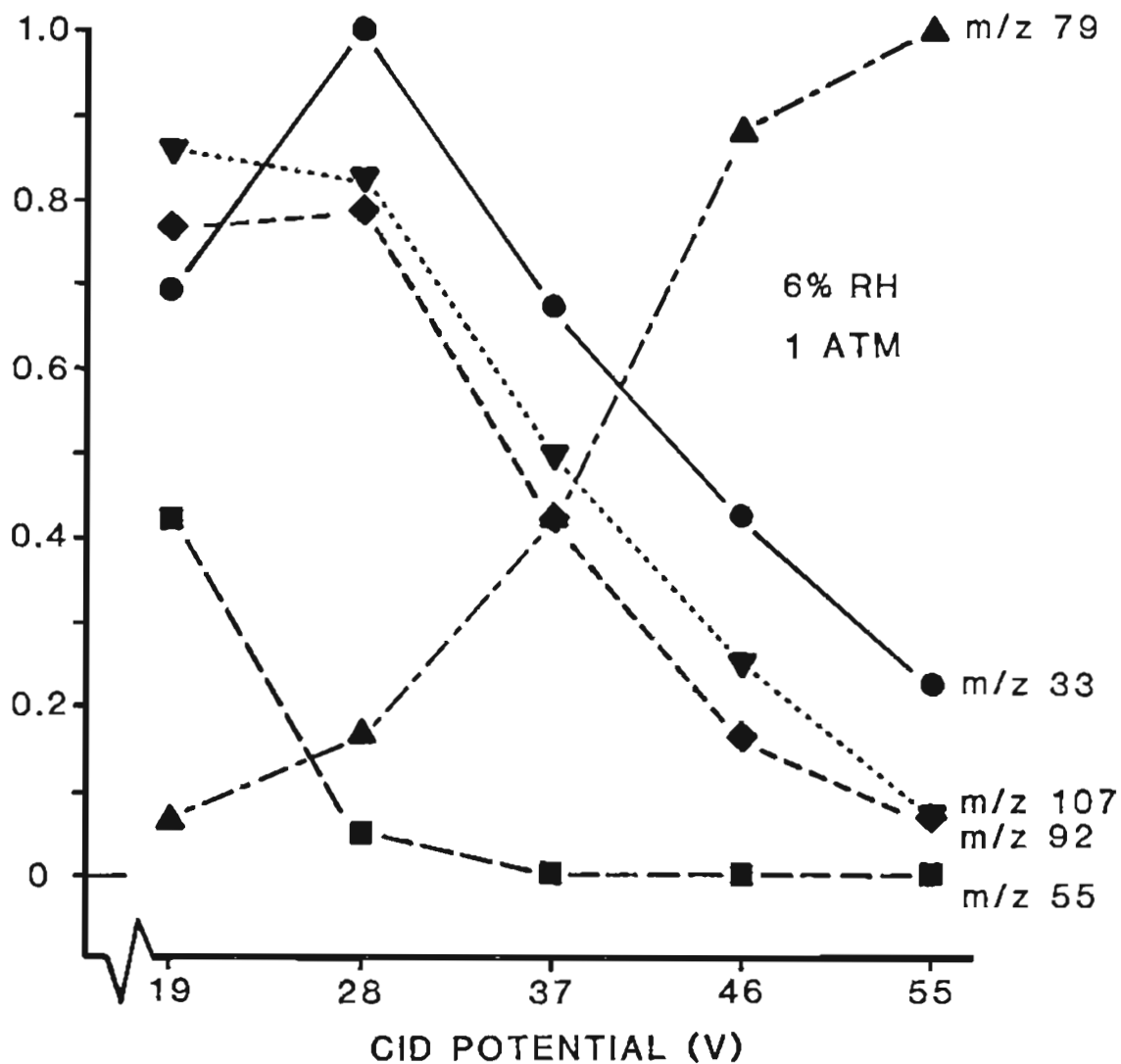


FIGURE III.5.b) Ion abundance plots of five ions vs the CID potential with a corona region pressure of 1 atm and a relative humidity of 6%. For each ion the abundances are normalized to the largest value obtained for that ion in the data used to plot Figures III.5 through III.7. The ions are: m/z 33, protonated methanol; m/z 55, hydrated proton,  $H(H_2O)_3^+$ ; m/z 79, fragmented ion of benzaldehyde; m/z 92, charge transfer ion of toluene; and m/z 107, protonated benzaldehyde. This data was recorded using the more concentrated test atmosphere.

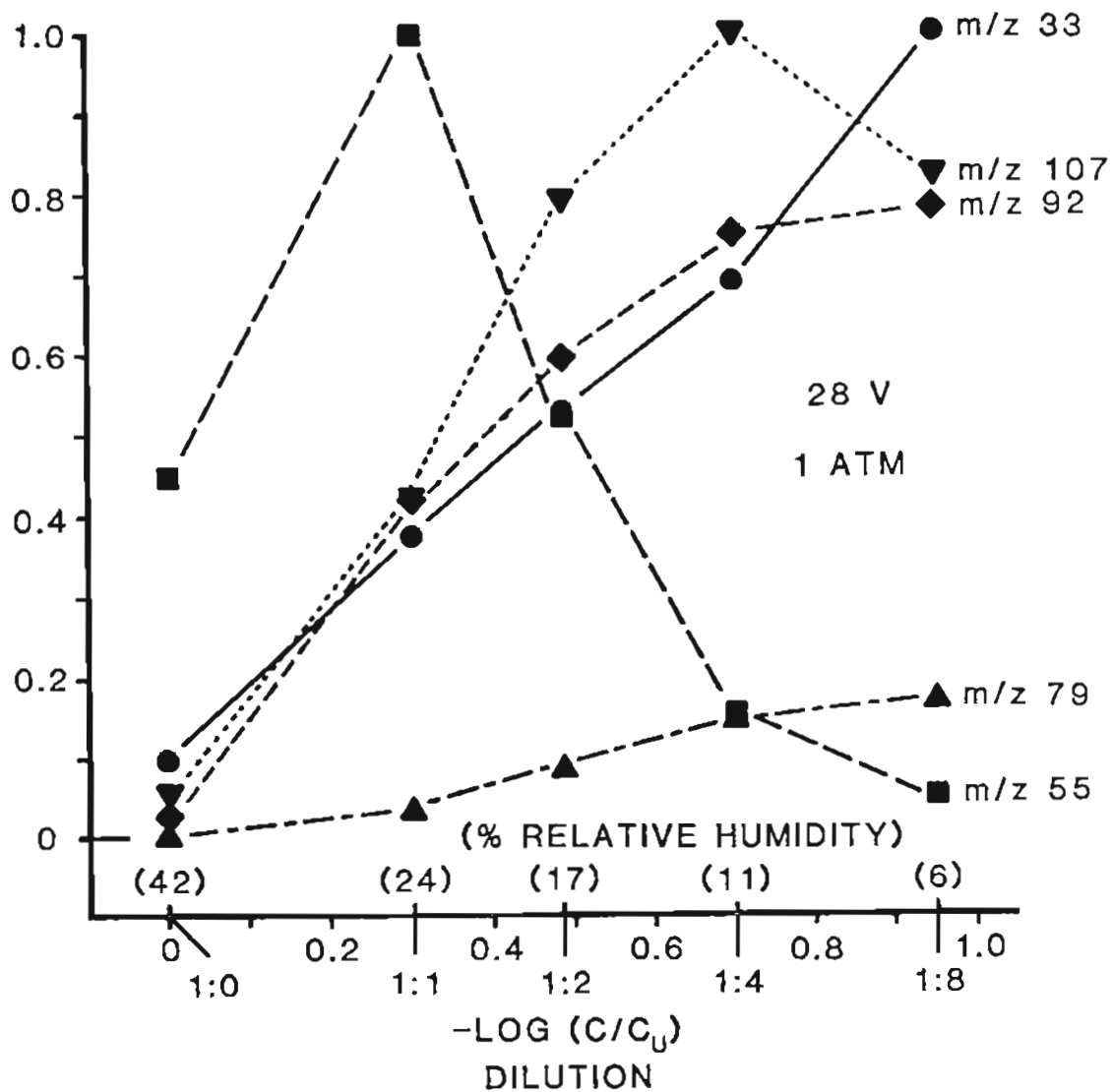


FIGURE III.6.a) Plots of the same five normalized ion abundances in Figure III.5 vs the dilution ratio (relative humidity) with a corona region pressure of 1 atm and a CID potential of 28 V. The negative logarithmic scale provides a more even distribution of the points along the x axis. This data was recorded using the more concentrated test atmosphere.

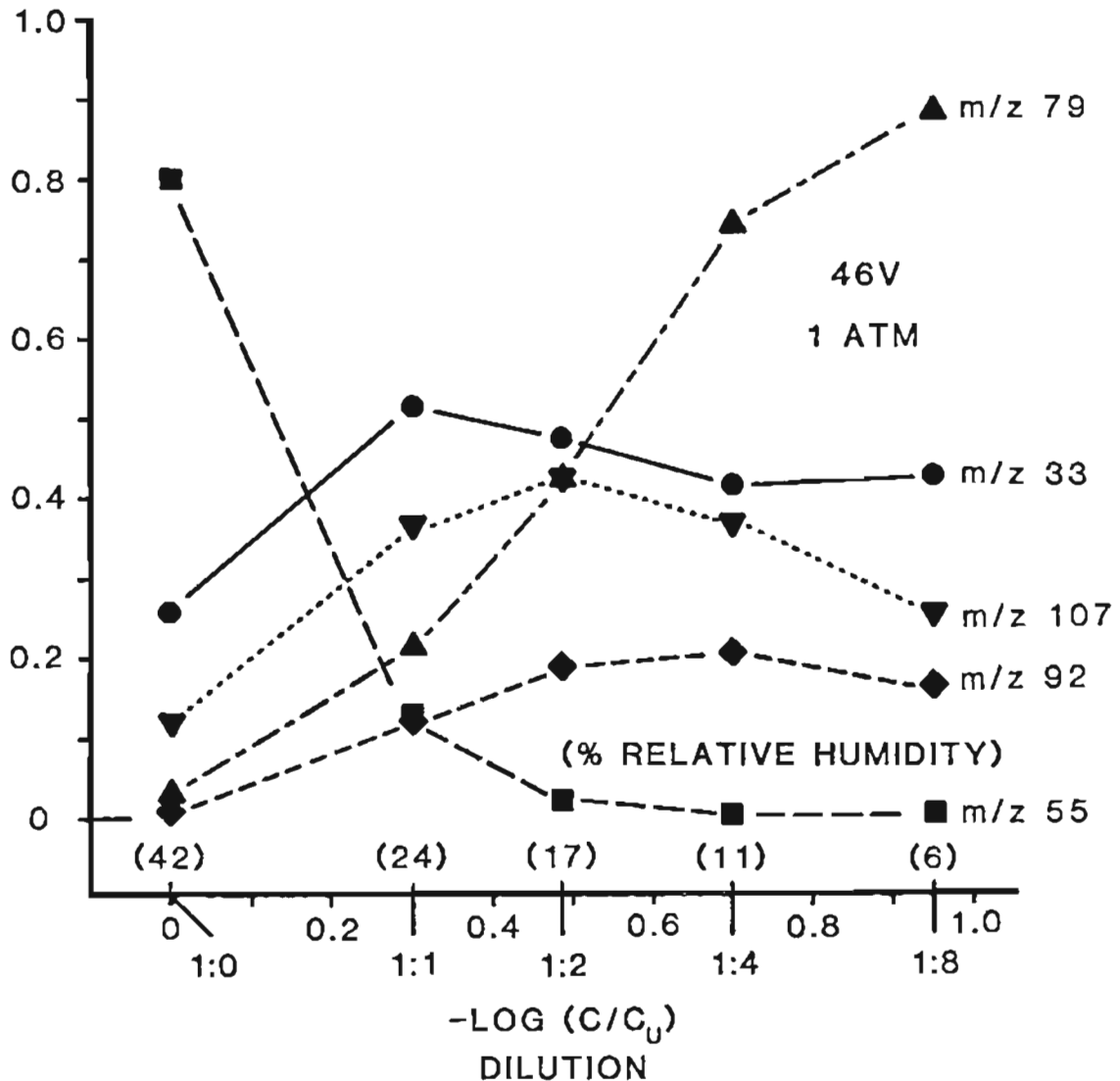


FIGURE III.6.b) Plots of the same five normalized ion abundances in Figure III.5 vs the dilution ratio (relative humidity) with a corona region pressure of 1 atm and a CID potential of 46 V. The negative logarithmic scale provides a more even distribution of the points along the x axis. This data was recorded using the more concentrated test atmosphere.

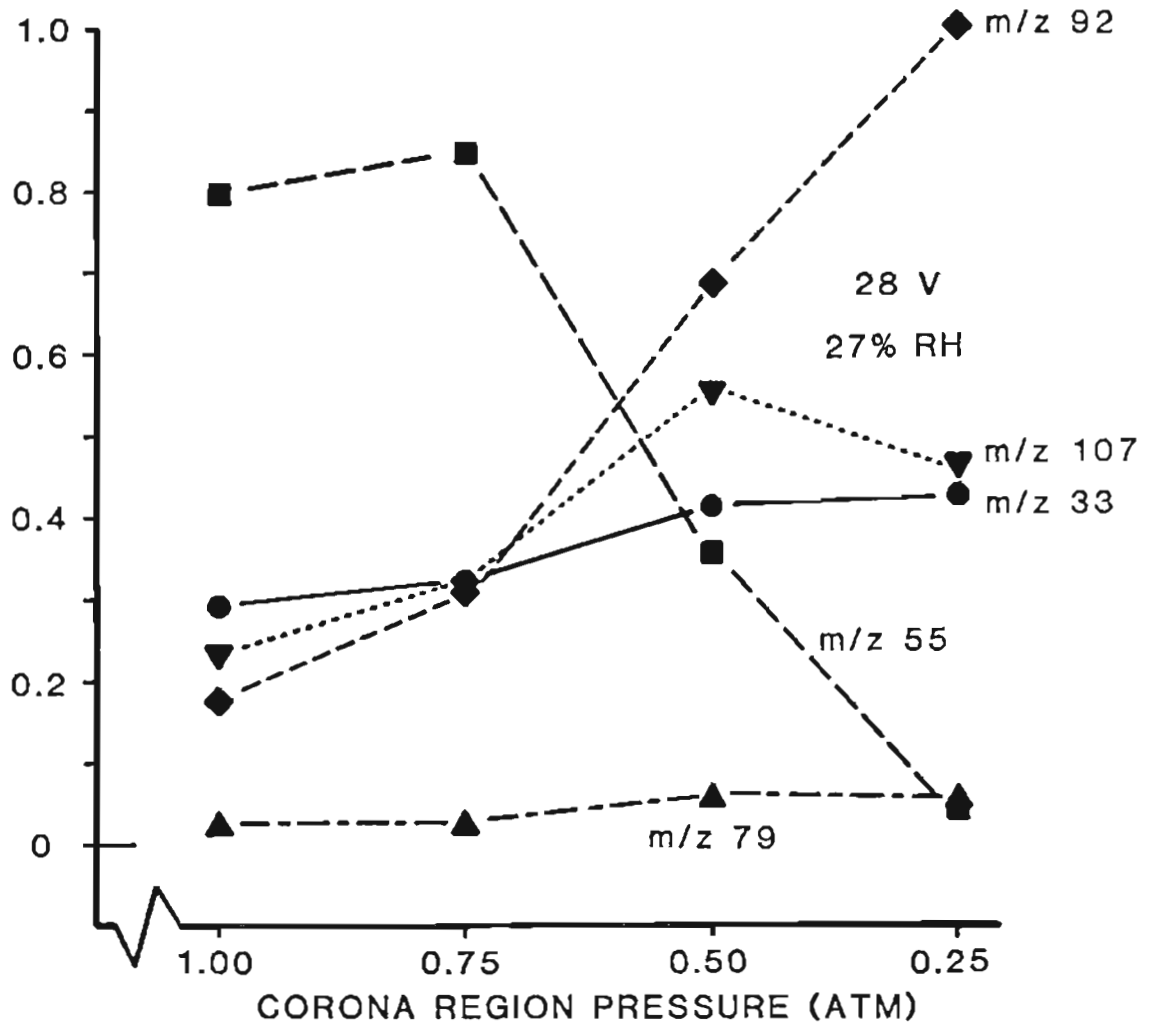


FIGURE III.7. Plots of the same five normalized ion abundances in Figure III.5 vs the corona region pressure with a relative humidity of ~27% and a CID potential of 28 V. This data was recorded using the more concentrated test atmosphere.



The total ion currents for all mass spectra from which ion abundance data was used were checked to ensure the trends cited and discussed below were not altered by the ion collection efficiency from each set of API source conditions. For the purpose of optimizing instrument response, the ion collection efficiency is but one variable influencing sensitivity for analytes; the values plotted are directly related to the ion abundances observed. If inferences about the ion-molecule processes that lead to observed trends are to be made, any significant effect of ion collection efficiency on the trends should be removed by normalizing signal intensities to the largest total ion current. When this was done the maximum for an ion within a figure was occasionally shifted one position to the right or left, but such shifts have no bearing on the qualitative explanations for the general trends discussed below. Agreement between the two test atmospheres regarding trends and maxima was generally good; only major discrepancies will be cited and discussed.

Observed trends result from the ion-molecule chemistry taking place in both the corona and CID regions. In Figures III.5.a and III.5.b the corona region pressure and relative humidities of the sample gas are constant. In these two figures the distribution of ions entering the CID region, determined by the constant conditions in the corona region, is fixed; the figures illustrate changes in ion abundances in the mass spectra that occur due to changes in the kinetic energy of collisions within the CID region as the CID potential is varied for high and low extremes of relative humidity.

Figures III.6.a and III.6.b demonstrate trends resulting from changing the relative humidity of the sample gas entering the source for fixed values of the CID potential and corona region pressure. Trends observed in these figures arise from changes in the number density of water molecules in the source; these changes alter the degree of hydration occurring in the corona region and the extent of condensation of water molecules about ions during adiabatic expansion through the orifice separating the two regions of the API source.

Figure III.7 also illustrates shifts due to changes in the number density of water molecules, in this case caused by changing the corona region pressure.

Discussed, in turn, are the trends evidenced by each class of ions represented in these figures: the hydrated proton,  $\text{H}(\text{H}_2\text{O})_3^+$ , at  $m/z$  55 (squares); the protonated molecular ions of methanol at  $m/z$  33 (circles) and of benzaldehyde at  $m/z$  107 (upside-down triangles); the molecular ion of toluene formed through charge transfer at  $m/z$  92 (diamonds); and the benzaldehyde fragment ion at  $m/z$  79 (right-side-up triangles).

### III.3.f) Hydrated Proton Ion

In Figure III.5.a the abundance of the  $m/z$  55 ion initially increases and then decreases as the CID potential increases. At high relative humidities, the average size of hydrated protons produced by reactions 4-6 within the corona region is large. Following condensation of additional water molecules about these hydrated protons during the adiabatic expansion through the orifice, disaggregation occurs in the CID region; incomplete disaggregation allows hydrated protons larger

than the hydronium ion to enter the mass analyzer. The abundance of  $m/z$  55 ions results from the competition between disaggregation of  $m/z$  55 ions into smaller hydrated protons and their production from incomplete disaggregation of larger hydrated protons. Initially, as the CID potential is increased, production of  $m/z$  55 ions becomes more important; for CID potentials greater than 46 V more complete disaggregation causes the abundance of  $m/z$  55 ions entering the mass analyzer to decline. In Figure III.5.b the relative humidity is much lower; the average size of hydrated protons reaching the CID region is much smaller and increasing disaggregation of hydrated protons causes the  $m/z$  55 ion abundance to decrease as the CID potential is increased over its entire range.

In Figures III.6.a and III.7 the  $m/z$  55 peak initially grows and then shrinks in abundance as the number density of water molecules in the source is reduced. At the low CID potential (28 V) used in these figures, disaggregation is very incomplete and the distribution of hydrated protons entering the CID region is reflected in the spectra. This distribution changes dramatically with the number density of water molecules in the source. In the spectrum for a 19 V CID potential and 1:1 dilution in Figure III.3.b, the  $m/z$  55 ion is the most abundant hydrated proton; this is also reflected in Figure III.6.a.

In Figure III.6.b more complete disaggregation at a higher CID potential (46 V) causes the  $m/z$  55 ion abundance to fall monotonically as the number density of water molecules is reduced; most of the hydrated protons entering the CID region, including the  $m/z$  55 ions, have been disaggregated into hydronium ions or hydronium ions associated

with one water molecule ( $m/z$  19 and 37) as seen in Figure III.3.b for the row of spectra recorded with this CID potential. The abundance of  $m/z$  55 ions in Figure III.6.b is determined by the number of larger hydrated protons that enter the CID region to be disaggregated into the  $m/z$  55 ion. Since the number of such larger hydrated protons falls along with the number density of water molecules, the initial increase in this ion's abundance, seen in Figures III.6.a and III.7, is not observed in this instance.

### III.3.g) Protonated Molecular Ions

At the high relative humidity in Figure III.5.a (42%) the abundances of the protonated methanol ion ( $m/z$  33) and protonated benzaldehyde ion ( $m/z$  107) are small compared to the low relative humidity condition in Figure III.5.b (6%). This observation and the very low relative abundances of these ions in the upper left corner spectrum in Figure III.3.a indicate that large hydrated protons do not appreciably protonate methanol and benzaldehyde molecules; the spectrum clearly shows that most of the ions are hydrated protons. This spectrum best reflects the ion distribution entering the CID region at the highest relative humidity studied, since the lowest CID potential induces the least disaggregation of hydrated ions.

Very recent work by Sunner et al. confirms and explains this observation for many oxygenated analytes (33). Their work demonstrates that larger hydrated protons do, however, protonate nitrogen bases. Hence, manipulation of the relative humidity (or corona region pressure) could be used to adjust the relative sensitivities for these types of

compounds in photooxidation studies.

In Figure III.5.a the abundances of both protonated molecular ions increase as the CID potential is increased. Greater disaggregation of large hydrated protons within the CID region provides more hydrated protons capable of protonating the oxygenated analytes. Additional analyte molecules are subsequently protonated within the CID region and the analyte signals are enhanced. It is reasonable that ion-molecule reactions can occur in addition to disaggregation and fragmentation in the CID region at a pressure of 1 Torr, since ion-molecule reactions occur at pressures several orders of magnitude lower when the inert gases normally used in a collisionally induced dissociation cell are replaced with a reactive gas (48).

In Figure III.5.b the protonated analyte peaks decline with increasing CID potential. Shifts to the left side in reactions 4-6 at lower relative humidity provide a smaller average size of hydrated protons in the corona region. Consequently, more protonated analyte ions are formed in the corona region. Fewer large hydrated protons enter the CID region to be disaggregated into smaller hydrated protons capable of protonating the oxygenated analytes. Signal enhancement from this process is therefore diminished, while increasing fragmentation of molecular ions causes a net decrease in the signal.

In Figures III.6.a and III.7 the protonated molecular ion abundances increase as the number densities of both water and analyte molecules fall. In Figure III.6.a the abundance of the benzaldehyde ion ( $m/z$  107) reaches a maximum at a relative humidity of 11%; the signal response of methanol continues growing up to the highest dilution, 1:8

(6% RH), used in the experiment. In Figure III.7 similar behaviors are seen. At the higher CID potential of 46 V (Figure III.6.b) the protonated analyte ion abundances initially increase as the relative humidity decreases; maxima then occur at different dilutions for the two analytes.

The analyte ion abundances depend on the number densities of both analyte molecules and reagent ions in the two regions of the API source. In the corona region the smaller hydrated protons present at lower number densities of water molecules more readily protonate the oxygenated analyte molecules as indicated by the initial increase in the relative abundances of the hydrated analyte ions in Figure III.3.a with decreasing relative humidity at low CID potentials. These hydrated analyte ions are formed in the corona region or during adiabatic expansion into the CID region.

At high number densities of water molecules, the availability of reagent ions limits the amount of  $AH^+$  ions formed; most of the positive ions exist as large hydrated protons. As the number density of water molecules is decreased, a greater proportion of the hydrated protons become small enough to protonate methanol and benzaldehyde in the corona region, and in the CID region a greater proportion of the hydrated protons are disaggregated into reagent ions, which can protonate the oxygenated analyte molecules present. After maxima in the protonated molecular ion curves appear, the availability of analyte molecules becomes important in determining the analyte ion abundances, and the decreased response due to analyte dilution exceeds the increased response due to increasing reagent ion availability.

The analyte ion signals are saturated with respect to the analyte molecules as long as the reagent ion availability controls their amplitudes. Differences in the maxima of the curves for the protonated molecular ions plotted in Figure III.8.a for the test atmosphere containing 10-fold lower analyte concentrations illustrate this point. While the ion abundances of the protonated molecular ions increased monotonically with increasing CID potential in Figure III.5.a, for the second test atmosphere at a relative humidity of 49%, the methanol and benzaldehyde signals peaked at 46 V and 37 V respectively. For the more concentrated atmosphere, analyte saturation occurred throughout the range of CID potentials. An excess of analyte molecules ensured essentially complete consumption of the increasing number of reagent ions resulting from disaggregation as the CID potential was increased; this saturation prevented the reduction in protonated analyte signals observed for the less concentrated atmosphere.

At a relative humidity of 6% (Figures III.5.b and III.8.b), the maxima in ion signals for protonated methanol occurred at the same CID potential for both atmospheres, while a broad maximum was seen at 19 and 28 V for protonated benzaldehyde in both figures. At this low number density of water molecules, sufficient numbers of reagent ions were present to avoid analyte saturation when sampling either test atmosphere even at low CID potentials. Hence, analyte dilution and increasing fragmentation caused the curves to fall as the CID potential increased.

For the dilute test atmosphere at a CID potential of 28 V (Figure III.9.a), the maxima in the abundances for the  $m/z$  33 and 107 ions occurred at a dilution of 1:2, rather than at dilutions of 1:8 and 1:4

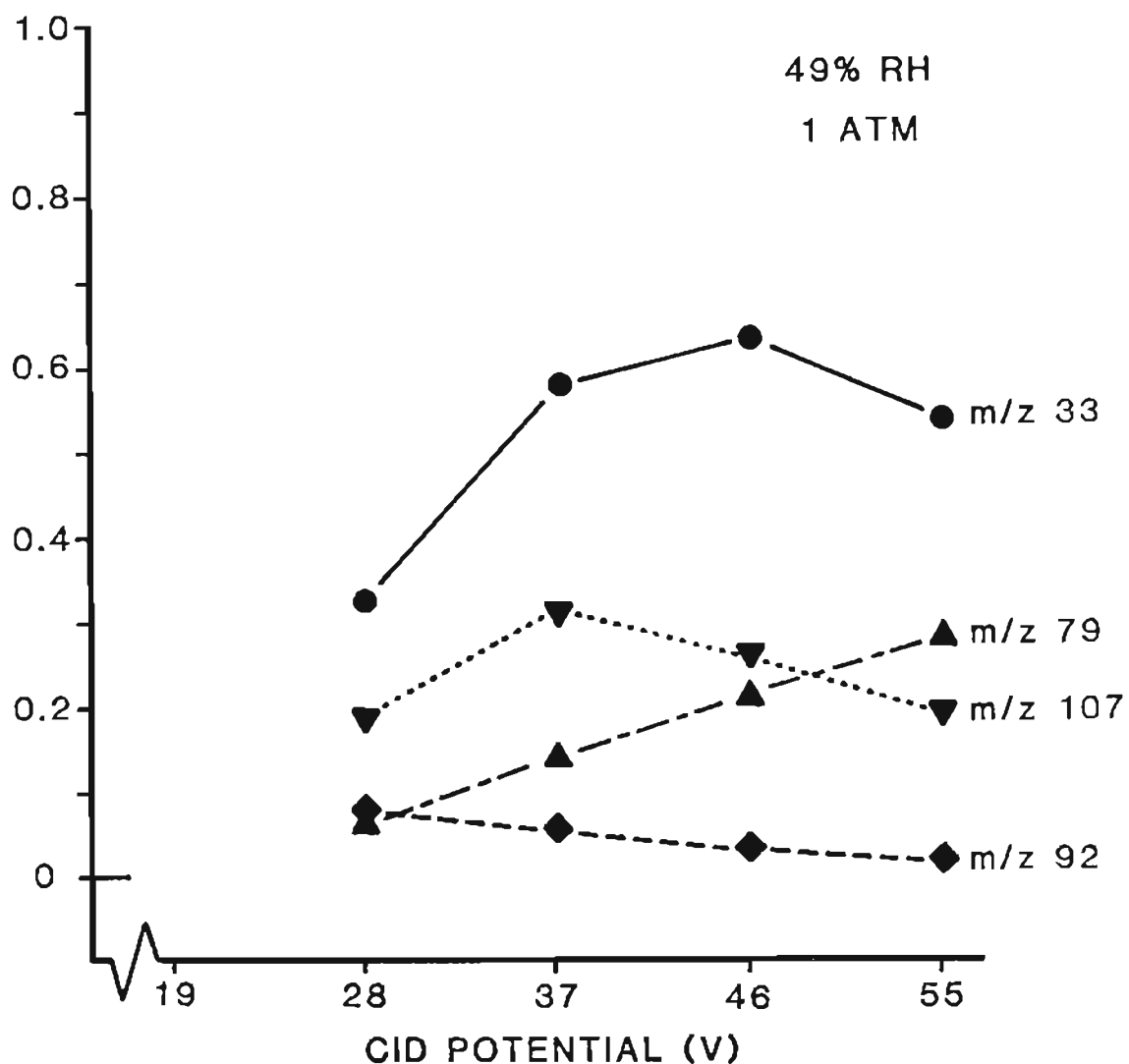


FIGURE III.8.a) Ion abundance plots of four ions vs the CID potential with a corona region pressure of 1 atm and a relative humidity of 49%. For each ion the abundances are normalized to the largest value obtained for that ion in the data used to plot Figures III.8 and III.9. The ions are: m/z 33, protonated methanol; m/z 79, fragmented ion of benzaldehyde; m/z 92, charge transfer ion of toluene; and m/z 107, protonated benzaldehyde. This data was recorded using the less concentrated test atmosphere.



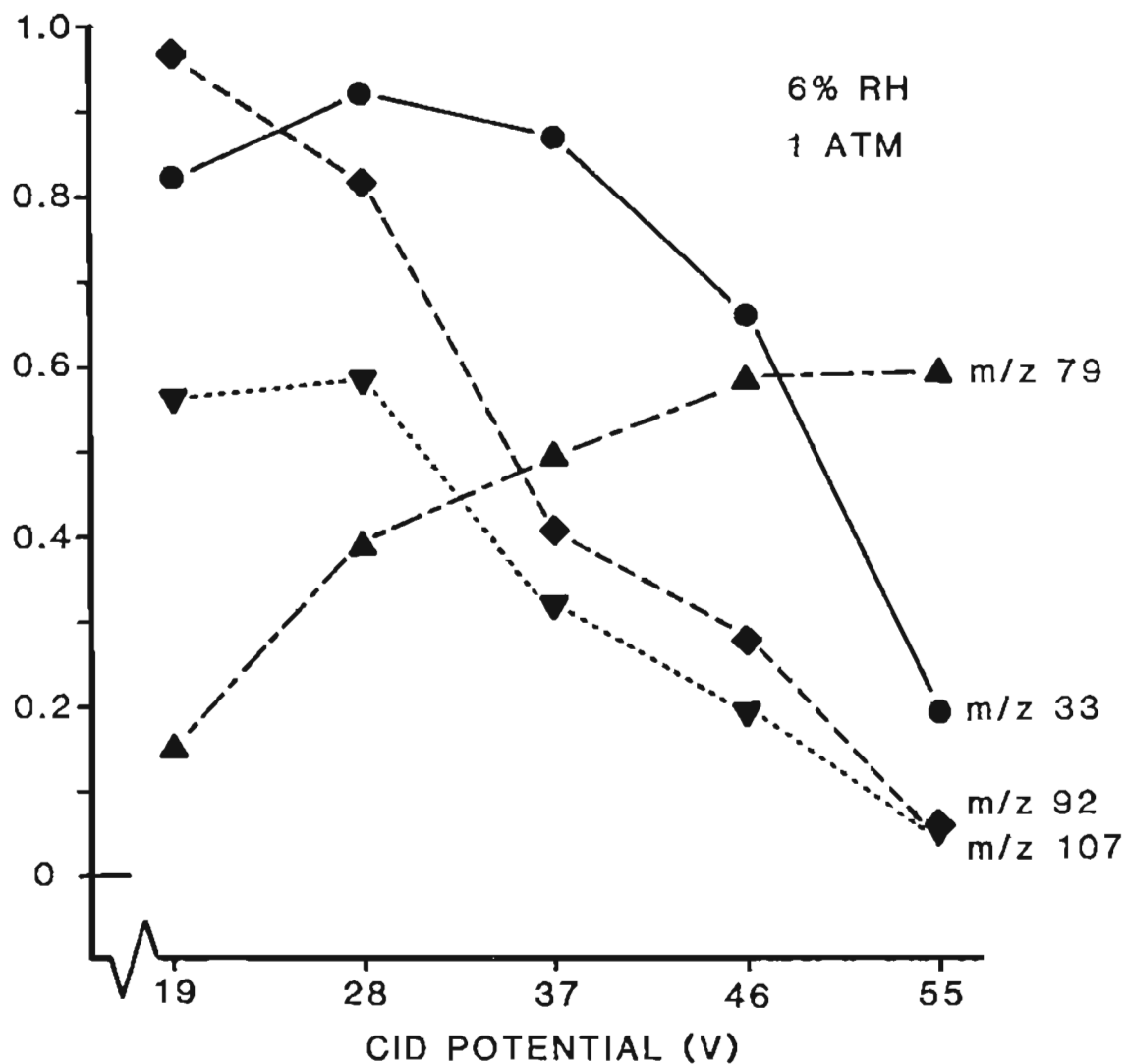


FIGURE III.8.b) Ion abundance plots of four ions vs the CID potential with a corona region pressure of 1 atm and a relative humidity of 6%. For each ion the abundances are normalized to the largest value obtained for that ion in the data used to plot Figures III.8 and III.9. The ions are: m/z 33, protonated methanol; m/z 79, fragmented ion of benzaldehyde; m/z 92, charge transfer ion of toluene; and m/z 107, protonated benzaldehyde. This data was recorded using the less concentrated test atmosphere.

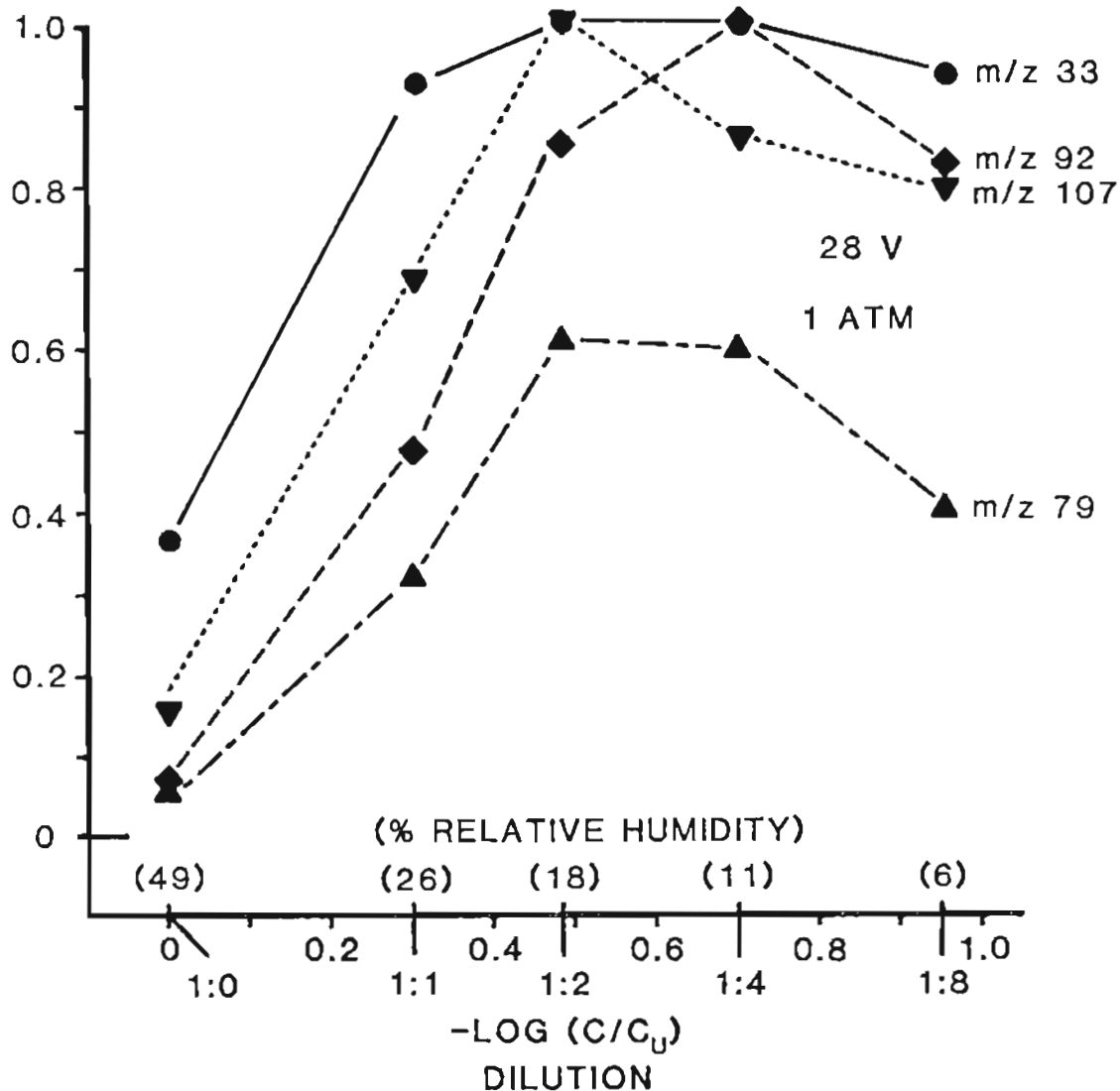


FIGURE III.9.a) Plots of the same four normalized ion abundances in Figure III.8 vs the dilution ratio (relative humidity) with a corona region pressure of 1 atm and a CID potential of 28 V. The negative logarithmic scale provides a more even distribution of the points along the x axis. This data was recorded using the less concentrated test atmosphere.

respectively, as was the case for the first atmosphere (Figure III.6.a). For the 46 V case (Figures III.6.b and III.9.b), however, the maxima occurred at the same dilution for benzaldehyde for both test atmospheres, and at dilutions of 1:1 and 1:2 for methanol for the more and less concentrated atmospheres respectively. For the more concentrated atmosphere with a CID potential of 28 V, the API source was essentially saturated with analyte molecules, so that the dilution of analytes at higher dilution ratios had little or no effect on the analyte ion abundances; the protonated analyte signals were limited by the number of reagent ions present. The more similar molecular ion curves of methanol and benzaldehyde for the two test atmospheres with a CID potential of 46 V indicates that the reagent ion concentrations in the CID region were large enough relative to the analyte concentrations in both atmospheres to avoid saturation for oxygenated analytes even at high relative humidities.

During collection of the data in Figures III.6.a and III.6.b dilution of the reservoir gas occurred between each pair of dilution ratios (viz., from left to right, 13%, 6%, 5%, and 4%). When saturation by analyte molecules occurs, more analyte molecules do not enhance the analyte ion signals, and slight dilution of the reservoir gas introduces little or no error. The greatest error occurs for the  $m/z$  107 curve in Figure III.6.b. When the reservoir gas/diluent ratio was increased from 1:4 to 1:8, the benzaldehyde concentration in the sample gas decreased by 47%, while the  $m/z$  107 ion abundance decreased only 25%. A portion of this decline resulted from greater fragmentation of the parent ion rather than from the dilution. The signal response vs

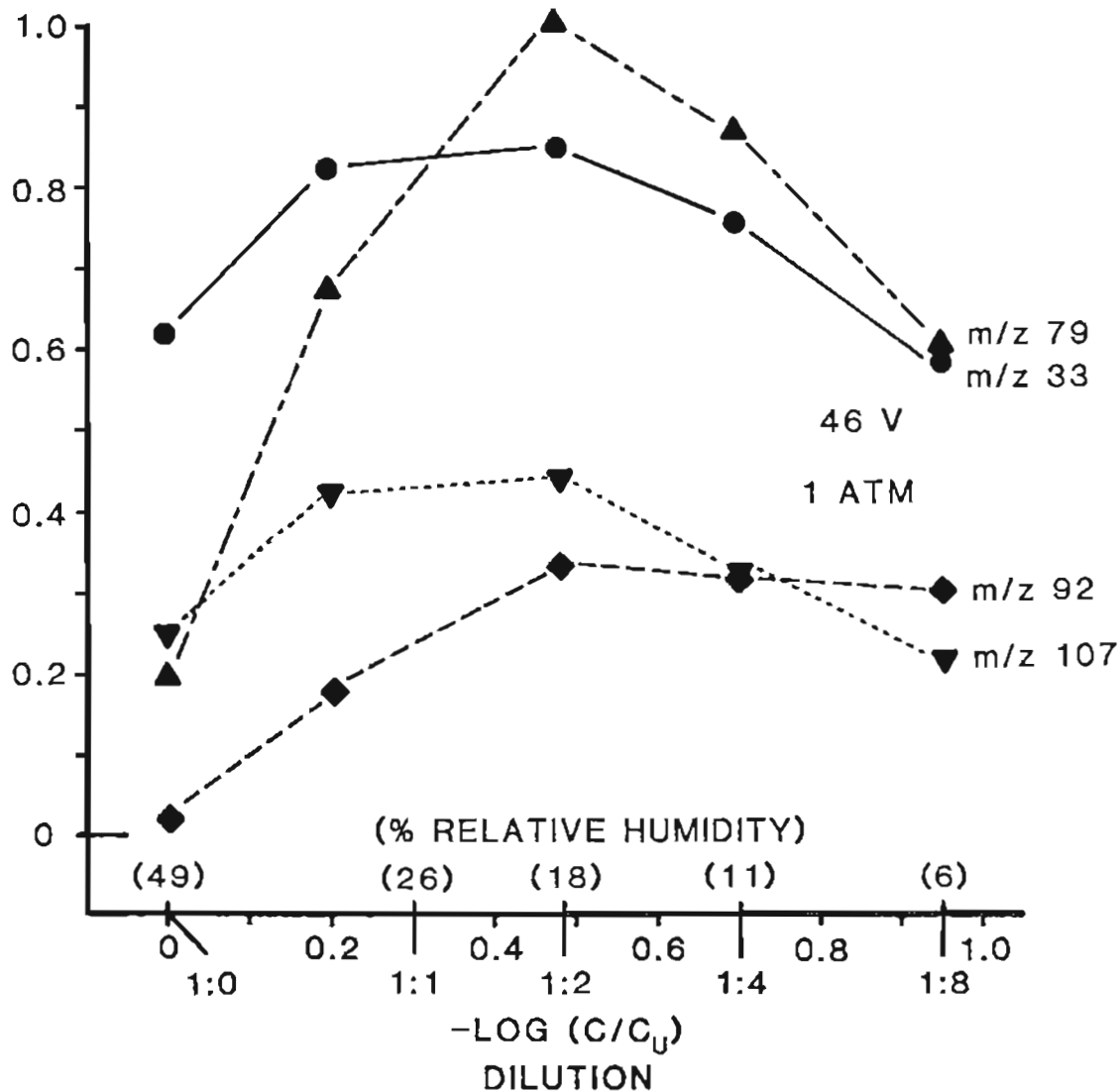


FIGURE III.9.b) Plots of the same four normalized ion abundances in Figure III.8 vs the dilution ratio (relative humidity) with a corona region pressure of 1 atm and a CID potential of 46 V. The negative logarithmic scale provides a more even distribution of the points along the x axis. This data was recorded using the less concentrated test atmosphere.

dilution was non-linear and, in fact, a 4% correction to account for reservoir dilution would result in an over-correction that would actually increase the error. Hence, no corrections for reservoir gas dilution were made for the plots displayed. When over-corrected plots were made, no changes in trends or maxima locations were observed.

Figures III.5.b, III.6.a, and III.7 indicate low number densities of water molecules provide greater sensitivity for protonatable analytes. Smaller hydrated protons in both the corona and CID regions result in more complete protonation of the oxygenated analytes in both regions.

#### III.3.h) Charge Transfer Molecular Ion

In contrast to the protonated molecular ions in Figure III.5.a, the small toluene signal at  $m/z$  92, comprised of ions formed in the corona region through charge transfer from precursor ions of the hydrated protons, declines as the CID potential is increased. Unlike methanol and benzaldehyde, no proton transfer to toluene molecules occurs from smaller hydrated protons formed through disaggregation in the CID region; the molecular ion peak for toluene declines due to increasing fragmentation caused by more energetic collisions at higher CID potentials. This trend is more obvious in Figure III.5.b in which larger ion abundances of the toluene molecular ion accompany a lower number density of water molecules.

As for the protonated analyte ions, enhancement of the toluene signal in Figures III.6.a and III.7 with decreasing number density of water molecules occurs, but for a different reason. Two or more consecutive reactions dependent on the number density of water molecules

(Chapter I) are necessary to produce a hydrated proton. Hence, water competes with toluene for charge transfer from precursor ions of the hydrated protons since the ionization potential of water, 12.6 eV, is higher than that of toluene, 8.8 eV (49). Reduction of the number density of water molecules in the corona region allows a greater fraction of the precursor ions to transfer charge to toluene molecules, enhancing the toluene signal. This signal enhancement indicates the  $m/z$  92 peak is not a hydrated ion since hydrated ion signals simultaneously decrease.

#### III.3.1) Fragmented Ion

In Figures III.5.a and III.5.b the  $m/z$  79 fragmented ion from benzaldehyde increases in abundance as the CID potential is increased. The increasing kinetic energy imparted to ions through collisions with neutral molecules in the CID region fragments a greater proportion of the parent ions. The fragmented ion abundances are greater in Figure III.5.b than in Figure III.5.a because more parent ions ( $m/z$  107) are available in the CID region for fragmentation at the lower relative humidity.

In Figures III.6.a, III.6.b, and III.7 the ion abundance of the  $m/z$  79 fragmented ion increases with decreasing number density of water molecules. For the test atmosphere containing 10-fold lower analyte concentrations, however, the  $m/z$  79 fragmented ion abundance curves showed maximums at a dilution of 1:2 rather than monotonic growth through the highest dilution for CID potentials of 28 and 46 V (Figures III.9.a and III.9.b). In addition, although the peak ratio,

{m/z 79}/[m/z 107], increased monotonically with a 46 V CID potential, it leveled off for dilutions greater than 1:1 for the 28 V case. These results indicate that decreasing the number density of water molecules does not always increase the extent of fragmentation; hence, it is an unreliable variable for identifying fragmented ions. Increasing the CID potential with constant number densities of water molecules, however, increased the ion abundance of the m/z 79 fragmented ion throughout the CID potential range for both test atmospheres (Figures III.5.a, III.5.b, III.8.a, and III.8.b). Hence, manipulating the CID potential is the best method for identifying fragmented ions.

#### III.4 CONCLUSIONS

##### III.4.a) Oxygenated Analyte Sensitivities

These results lead to the following conclusions.

- 1) Sensitivity for methanol and benzaldehyde (and many other (33) oxygenated molecules) is enhanced when the number density of water molecules in the corona region is low. Only small hydrated protons are effective at protonating such molecules; the fraction of the sum of all hydrated protons small enough to protonate these analytes is larger at lower relative humidities (36) as equilibria 4-6 are shifted to the left.

- 2) The abundances of oxygenated analyte ions are determined by the number densities of both small hydrated protons and of analyte molecules. Reducing the number density of water molecules through dilution with dry zero air or through

reduction of the pressure in the corona region enhances sensitivity for oxygenated analytes until the increase in the number of smaller hydrated protons in the corona region is offset by the dilution of the analyte molecules.

#### III.4.b) Operating Conditions for Studies of Atmospheric Reactions

The results of this study suggest some general guidelines for optimization of an API source's operating conditions when studying atmospheric photooxidation.

The most conveniently and rapidly adjusted variable is the CID potential. The useful lower limit of the CID potential is readily found by reducing the CID voltage until the ion signals become erratic or disappear altogether. In general, for a given pressure in the corona region and a given relative humidity, increasing the CID potential from its useful lower limit will cause:

- 1) hydrated proton peaks to fall abruptly, possibly after a small initial rise,
- 2) hydrated molecular ion peaks to fall,
- 3) protonated molecular ion peaks to pass through a broad maximum or, if the number density of water molecules is low, to just decline gradually,
- 4) molecular ion peaks formed by charge transfer to fall, and
- 5) fragmented ion peaks to grow.

Molecular ion peaks formed by charge transfer can be distinguished from hydrated ions by reducing the number density of water molecules in



the API source; the ions formed by charge transfer will increase in abundance while hydrated ion abundances will decrease.

The optimum settings for the CID potential are determined by the requirement for differentiating between hydrated ions, protonated molecular ions, and fragmented ions, while retaining good sensitivity. Sensitivity for protonatable analytes is enhanced when the number density of water molecules is small enough that many small hydrated protons are present in the corona region. Only a small CID potential is needed under such conditions to decluster hydrated analyte ions, thereby simplifying the mass spectra obtained; too great a CID potential decreases sensitivity by fragmenting molecular ions.

Awareness of the trends discussed should be a valuable aid in real time analysis of atmospheres.

CHAPTER IV  
SUPPRESSION OF SPURIOUS OXIDATION PRODUCTS IN AN  
ATMOSPHERIC PRESSURE IONIZATION SOURCE

IV.1. INTRODUCTION

In previous chapters the design and operation of an API source built for use with a VG 7070E-HF mass spectrometer were described, and medium resolution sufficient to distinguish between oxidized hydrocarbons having the same nominal mass but different molecular formulae was demonstrated. Manipulation of operating variables to simplify the complex spectra expected from gas mixtures, to enhance sensitivity for analytes, and to identify the types of ions present was also demonstrated.

With this instrument and our understanding of its operation, we began a study of toluene photooxidation. With toluene in the reaction vessel peaks due to oxidation products appeared in mass spectra recorded before irradiation. Toluene was being oxidized in the API source. The experiments in this chapter were performed to delineate the problem and to develop strategies for suppressing the formation of these spurious products. The three strategies examined were: 1) minimization of the corona discharge current to reduce production of the radical that attacks toluene; 2) addition of a scavenger gas for this radical; and 3) enhancement of the flow through the source to reduce the residence

(reaction) time for neutral species in the corona region.

## IV.2. EXPERIMENTAL SECTION

### IV.2.a) Test Atmospheres and Flows

A test atmosphere of zero air at a nominal relative humidity of 58% containing 10 ppm of NO was prepared in the 12 L reservoir as described in Chapter III. 10 ppm of methyldeuterated toluene was added after recording a background spectrum. Contents from the reservoir were driven toward the API source with dry zero air and then diluted 1:8 with additional dry zero air to provide a sample gas having a relative humidity of ~6%. This choice of relative humidity enhanced sensitivity for D<sub>3</sub>-toluene and its products, suppressed formation of hydrated ions (Chapter III), and slowed the rate of exponential dilution which occurred in the reservoir during the experiment. The flow drawn through the API source was normally 19-24 cm<sup>3</sup> min<sup>-1</sup>. Allowing for an additional flow of 2 cm<sup>3</sup> min<sup>-1</sup> through a vent that assured atmospheric pressure was maintained in the flask (Figure III.1), a maximum flow of 2.9 cm<sup>3</sup> min<sup>-1</sup> was required from the reservoir; hence, after 8 hours of continuous flow, the flask contents are diluted no more than 11% (Appendix B). In one experiment the flow through the corona region was increased four-fold to 82.5 cm<sup>3</sup> min<sup>-1</sup> by drilling a 100 μm hole through the walls of the orifice holders to the pumping line (Figure II.1).

These experiments were performed over a 4 day period. After 3 days the flask contents had been diluted 29%. The dilution ratio for additional zero air was changed to 1:5.4 to restore the relative

humidity and toluene concentration in the API source to its initial value. The range of relative humidity within the corona region during the experiments was 4.6-6.5%. This small range and the toluene dilution did not significantly affect the qualitative comparisons discussed below. A motor driven syringe was used to add CO to the sample gas entering the API source in one experiment.

#### IV.2.b) CID Potential and Mass Spectrometer Operation

The CID potential was maintained at 28 V to provide dehydration of hydrated ions without excessive fragmentation of parent ions (Chapter III).

Mass spectra were recorded with the slits set to pass ~90% of the maximum ion signal in order to maximize sensitivity; the resolution provided was ~1,500 (Chapter II). The peak areas were centroided by the data acquisition system and displayed as line spectra. A scan speed of 2 min/decade was used to smooth rapid fluctuations seen in the ion beam current. The spectra displayed are averages of four scans showing less than a 15% range in ion abundances for five of the largest peaks in the four spectra. The amplifier scale was chosen to provide good sensitivity for the chemical noise and the toluene oxidation products, which are the subject of this study.

The software initially displays any spectrum normalized to the largest peak in that spectrum. To facilitate visual comparison of the spectra on the basis of ion abundance the ordinate for all spectra was normalized to the same arbitrary abundance unit. Those spectra obtained using a 0.2  $\mu$ A corona current were also normalized with respect to the

total ion current to correct for day-to-day fluctuations. An amplifier range 25 times less sensitive was used to obtain the total ion currents to avoid amplifier saturation by the largest peaks ( $m/z$  19 and 37) in the spectra.

### IV.3. RESULTS AND DISCUSSION

#### IV.3.a) Background Mass Spectrum

Figure IV.1.a shows a mass spectrum obtained for zero air using a corona current of 1  $\mu\text{A}$ . The peaks seen arise from contaminants outgassed from the flow system or from the Vespel components in the corona region (Chapter II). Such contaminants can be ionized or react to form products in the corona region; these products can also be ionized. Ions can then be fragmented in the collisionally induced dissociation (CID) region, while ions formed from highly polar compounds may appear as hydrated ions in the spectra.

#### IV.3.b) Mass Spectra Displaying Spurious Products

Figures IV.1.b-d were obtained after addition of 10 ppm of  $\text{D}_3^-$  toluene to the reservoir using corona currents of 0.2, 1, and 5  $\mu\text{A}$  respectively. These spectra demonstrate two important points:

- 1) Numerous peaks appear in addition to the  $m/z$  95 peak due to the  $\text{D}_3^-$ -toluene molecular ion formed by charge transfer. Normally, in the absence of contaminant compounds containing odd numbers of N atoms, positive chemical ionization using a strong protonating agent such as hydrated protons, produces chemical

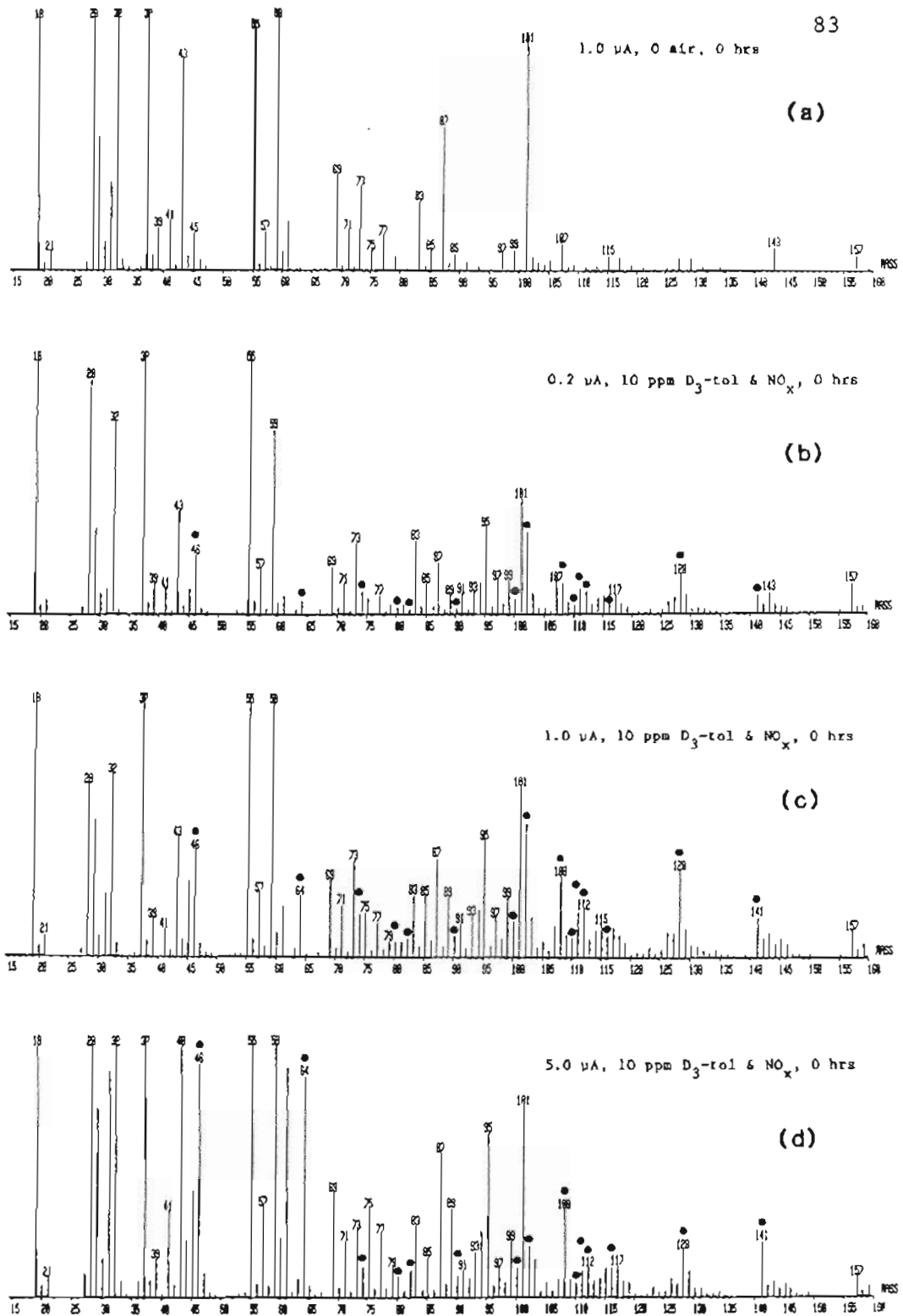


FIGURE IV.1. Four scan averages of mass spectra recorded before irradiation. The conditions are: a) background, 1  $\mu\text{A}$  corona current; b) after addition of 10 ppm of  $\text{D}_3\text{-toluene}$  to the reservoir, 0.2  $\mu\text{A}$ ; c) 1  $\mu\text{A}$ ; and d) 5  $\mu\text{A}$ .

noise having predominantly odd numbered  $m/z$  peaks. This is the case in Figure IV.1.a. Addition of  $D_3$ -toluene yielded numerous peaks at even  $m/z$  ratios due to ions containing the deuterated methyl group ( $CD_3$ ). The additional peaks result from reactions in the API source that produce spurious products, i.e. products not formed in the simulated atmosphere during irradiation.

Prominent examples of peaks due to spurious products formed from  $D_3$ -toluene, appearing as molecular, fragmented, or hydrated ions, are observed at  $m/z$  46, 64, 74, 80, 82, 90, 100, 102, 108, 110-112, 116, 128, and 141; these peaks are marked with dots. Identification of all these peaks has not been attempted, rather developing strategies to suppress them was the goal of this research.

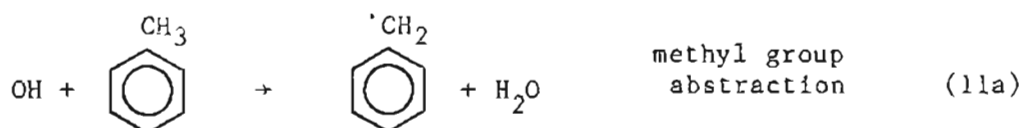
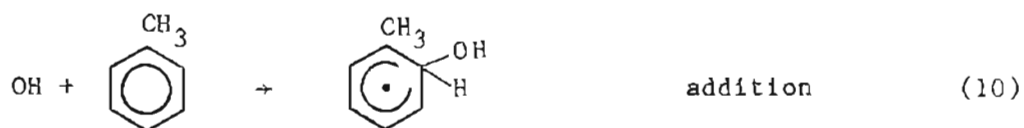
2) Over the range of corona current the total ion current increases 40%, while the proportion of the total ion current due to peaks having even  $m/z$  ratios increases by 80%. Relative to higher corona currents, the 0.2  $\mu A$  current produces a mass spectrum with a smaller fraction of the total signal resulting from spurious product and related peaks, while sacrificing only a small amount of the ion abundances due to true analytes.

#### IV.3.c) OH Radical Attack to Produce Spurious Products

As presented in Chapter I, series of ion-molecule reactions in the corona region produce hydrated protons. In these reaction sequences an OH radical is produced for each hydrated proton. Hence, the number of OH radicals formed in the ion source equals the sum of the hydrated

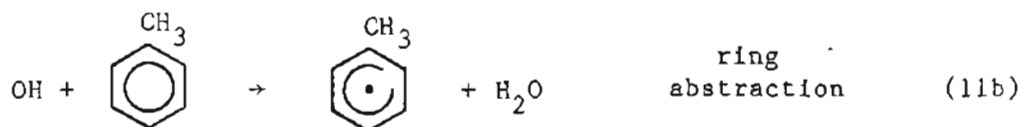
protons and of the protonated ions formed from these primary ions. Less than 1% of the total ion current observed in a mass spectrum is due to precursor ions of the hydronium ion or to charge transfer ions. Therefore, the number of OH radicals formed is approximately equal to the number of positive ions formed.

The formation of OH radicals is important because OH radical attack of toluene through addition to the aromatic ring ( $\geq 85\%$ ) and by abstraction of a hydrogen from the methyl group ( $\leq 15\%$ ) are the predominant initial reactions which consume toluene in the troposphere and in reaction vessels.



Reaction sequences branching from these and later intermediates yield numerous toluene photooxidation products (6-9).

At temperatures above  $380^\circ\text{K}$ , Perry et al. (52) determined that the addition pathway to product formation is unimportant, because the OH-toluene adduct decomposes into reactants, and that abstraction of a hydrogen atom from the aromatic ring is important.





#### IV.3.d) Effective Temperature in the Corona Region

The effective temperature within the corona region is above room temperature, the temperature at which many photooxidation studies are performed. Dzidic et al., using ion abundances and the temperature dependence of equilibrium constants, estimated the effective temperature to be 340-370°C above the source temperature when using a positive 10  $\mu$ A corona current (44). More direct measurements using interferometers (50,51) and thermocouples (50) to measure the temperature along the tip-to-orifice axis for point-to-plane, negative corona discharges found temperatures  $\sim 5^\circ\text{K}$  above the surrounding air. This study provides indirect evidence for an effective temperature between these extremes in the volume where spurious products that are protonated and analyzed are formed.

The product distribution resulting from OH attack in the API source will differ from that formed in a reaction vessel; most markedly at higher corona currents, which elevate the effective temperature in the corona region. As the effective temperature increases, the addition pathway will become unimportant, while the additional abstraction pathway will become more important. As seen in Figures IV.1.b-d, the product distribution clearly changes as the corona current is increased.

#### IV.3.e) Dependence of Spurious Product Yields on the Corona Current

Figure IV.2 displays ion abundances normalized to the total ion current for five mass spectra recorded over a 0.2 to 5.0  $\mu$ A range of corona currents; the currents are plotted on a logarithmic scale to

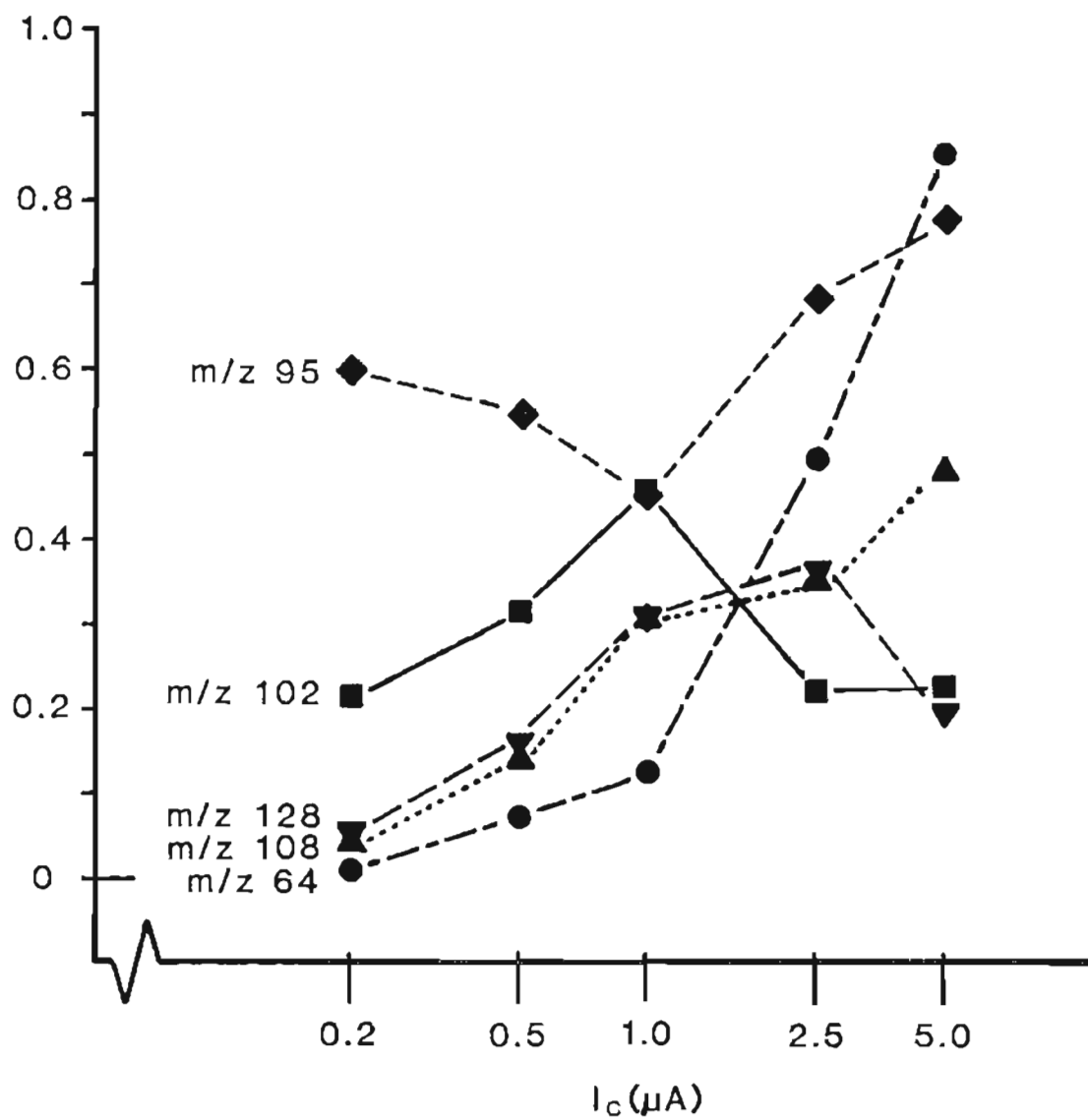


FIGURE IV.2. Ion abundances normalized to the total ion current (arbitrary units) vs the corona current plotted on a logarithmic scale. The  $m/z$  ratios plotted correspond to ions identified in the text.

avoid crowding of the points. The  $m/z$  ratios correspond to the  $D_3^-$  toluene molecular ion,  $m/z$  95, which is formed by charge transfer with the precursor ions of the hydronium ion, and to the four protonated, spurious products that yielded the largest relative ion abundances: protonated  $D_3$ -acetic acid (23),  $m/z$  64; possibly protonated  $D_3$ -4-oxo-2-pentenal (23),  $m/z$  102; protonated D-benzaldehyde (6-9,23),  $m/z$  108; and possibly protonated  $D_3$ -6-oxo-2,4-heptadienal (23). As the corona current increases two important variables are increased: the effective temperature in and near the discharge and the number of OH radicals formed in the corona region.

The relative abundance of the  $m/z$  95 ion first decreases, then increases. Initially, the increasing OH concentration increases the fraction of toluene consumed as it approaches the corona tip where charge transfer occurs. At higher corona currents the effective temperature increases and the addition pathway to spurious products becomes less important, decreasing the overall rate constant for OH attack of toluene; this effect is more important than the increasing OH concentration, and the fraction of toluene consumed decreases allowing more toluene to reach the charge transfer region.

Bolstering this explanation is the concurrent decrease in the relative abundance of the ion at  $m/z$  102 as the toluene molecular ion increases in relative abundance. An ion at  $m/z$  102 is also a spurious product formed from o-cresol as was observed when o-cresol alone was added to zero air entering the API source to determine if it would be protonated or form ions through charge transfer. Like toluene, o-cresol forms charge transfer ions and reacts with OH radicals, having a rate

constant 7.3 times greater than that for toluene. O-cresol is itself a product of toluene photooxidation in the atmosphere with a yield of ~20% (9) and its production is believed to occur through the addition pathway. As the addition pathway becomes insignificant at a higher effective temperature, less o-cresol is formed and the ion at  $m/z$  102, probably formed from o-cresol, decreases in relative abundance.

The Arrhenius plot of Perry (52) for toluene suggests that the effective temperature at which the addition pathway becomes unimportant is  $\sim 350^\circ\text{K}$ ; in Figure IV.2 this temperature corresponds to a corona current between 1 and 2.5  $\mu\text{A}$ . When using a corona current of only 0.2  $\mu\text{A}$ , the effective temperature must lie close to room temperature.

The ion abundance at  $m/z$  108 grows steadily with increasing corona current. Benzaldehyde is formed through the abstraction pathway which occurs more rapidly as the temperature increases.

The ion peak at  $m/z$  141 (not plotted) due to  $\text{D}_3$ -nitrotoluene increases gradually but nonmonotonically. Nitrotoluene is normally formed through the addition pathway (6-9) and would be expected to show a decline in ion abundance similar to that seen for the ion peak at  $m/z$  102 with increasing effective temperature. Since hydrogen extraction from the ring by OH becomes important at higher temperatures, however, nitrotoluene may be formed by reaction of  $\text{NO}_2$  with the resulting radical, a pathway not available at room temperature. This would explain its eventual increase in ion abundance.

The ion peak at  $m/z$  64 due to protonated  $\text{D}_3$ -acetic acid increases dramatically as the amount of OH formed increases. OH radicals attack primary products formed from toluene to produce secondary products; the

secondary products can, in turn, be attacked to produce tertiary products, etc. Production of later generation products, such as acetic acid, becomes more important as the OH concentration increases. Hence, the spectra in Figures IV.1.b-d display much larger peaks at even m/z ratios corresponding to smaller products as the corona current is increased. As primary products are attacked by OH radicals, ring fragmentation can produce more than one secondary product, and more than one observable product ion may arise from one toluene molecule.

The spurious product thought to be responsible for the m/z 128 ion should be a primary product formed through the addition pathway. In that case, its relative ion abundance should decline at corona currents  $> 1 \mu\text{A}$ ; instead the decline is not observed until after  $2.5 \mu\text{A}$ . An explanation for the location of the ion abundance maximum for this ion is not obvious.

#### IV.3.f) The OH Enriched Region

The residence time for neutral species in the corona region is much greater than the ion residence time,  $< 10^{-4}$  sec (33,44,53); the latter is determined by the potential gradient between the corona tip and the walls of the corona region. With a flow of  $20 \text{ cm}^3 \text{ min}^{-1}$  and a corona region volume of  $0.65 \text{ cm}^3$ , the neutral residence time is 2.0 sec ( $0.65 \text{ cm}^3 \times 1 \text{ min}/20 \text{ cm}^3 \times 60 \text{ sec/min}$ ). Adequate time is available for radical-molecule chemistry to occur (Appendix C).

Positive ions formed in the corona discharge are accelerated away from the needle tip (Figure IV.3) by the potential gradient between the tip and the corona region walls, while the negative ions are attracted

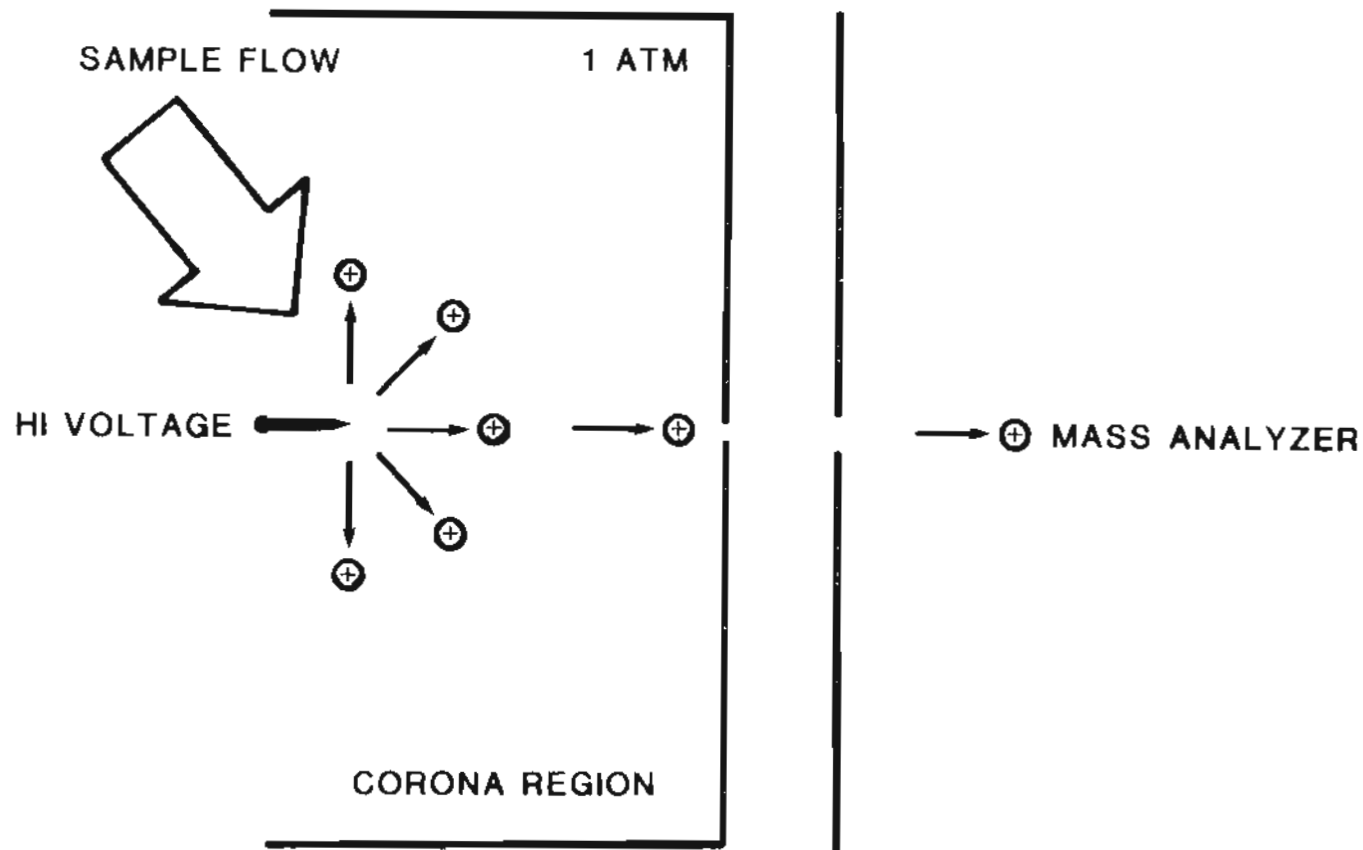


FIGURE IV.3. Illustration of the directions of ion travel and sample flow in the corona region. The majority of ions sampled by the mass analyzer are formed within a relatively small solid angle centered on the corona tip-to-orifice axis.

back to the needle tip. As the positive ions travel toward the walls, hydrated protons are formed. The neutral OH radicals produced are not accelerated and could build up in concentration within the corona region. Depicted schematically in Figure IV.4 are concentric regions where different ions are presumed to predominate. The figure is meant to illustrate the sequence of reactions, but nothing about the actual volumes where particular ions are dominant. The extent to which diffusion distributes the OH radicals is unknown.  $D_3$ -toluene molecules must approach the corona tip before undergoing charge transfer with the precursor ions of the hydronium ion; those that enter the OH enriched region first are subject to OH radical attack to yield spurious products.

The spurious products formed in this OH enriched region can be attacked by the OH radicals to yield later generations of spurious products; those readily protonated can also be ionized by hydrated protons and repelled from this region. The fractions of such products that are protonated and consumed by OH attack will depend on the concentrations of OH and hydrated protons. Both  $D_3$ -toluene molecular ions and ions due to spurious products that reach the mass analyzer were formed in a relatively small volume along the axis between the needle tip and the first orifice (Figure IV.3). The ions sampled include products of OH attack within the enriched region.

Only a small fraction of the toluene in the OH enriched region need be consumed before protonated product peaks appear in the mass spectra. For example, the response for benzaldehyde, as determined from a spectrum recorded with 19 ppm of toluene, 0.14 ppm of benzaldehyde, and

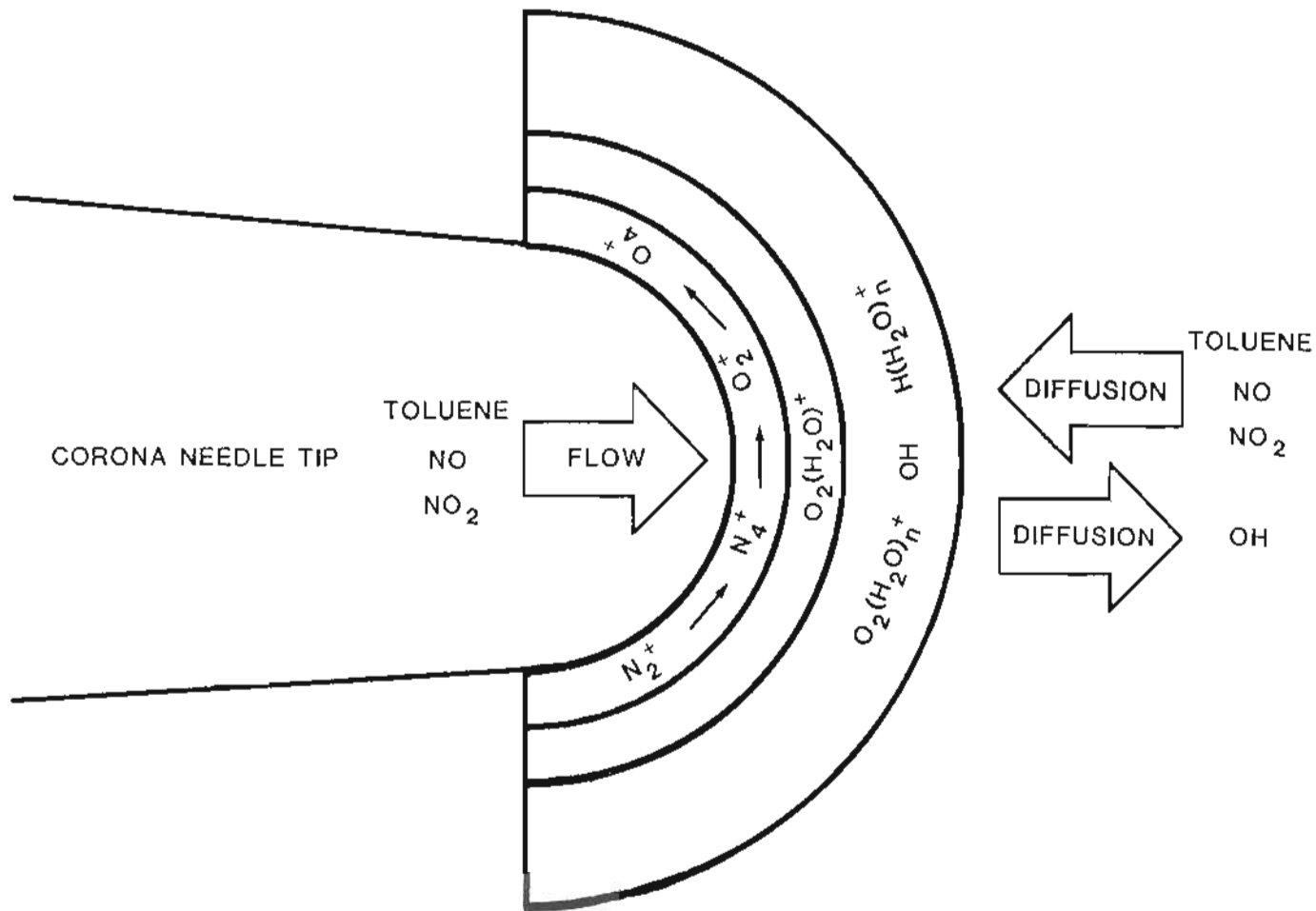


FIGURE IV.4. A schematic diagram of the needle tip illustrating regions where different positive ions are presumed to predominate based on the sequence of ion-molecule reactions discussed in Appendix C. The flow direction assumed in Appendix C is also illustrated. The OH enriched volume is larger than the enclosed region due to diffusion of OH radicals away from the tip.



3.6 ppm of methanol in the reservoir (Chapter III), is > 200 times that of toluene under these source conditions. As for toluene, sensitivity for spurious products ionized by charge transfer is much lower; such products are not likely to be observed. Benzaldehyde, a true photooxidation product that is readily protonated, does not display spurious product peaks in its mass spectrum. Much lower concentrations of benzaldehyde than of toluene are normally studied; any products formed are present at still lower concentrations and are not observed.

Discussions of the dimensions of the OH enriched volume and of the reactions that occur within it are found in Appendix C.

#### IV.3.g) Necessity for API Source Chemistry Suppression

To study reaction kinetics it is necessary to determine the yields of photooxidation products in the irradiated reservoir as a function of irradiation time. Subtraction of a spurious product's peak area measured before irradiation multiplied by the fraction of D<sub>3</sub>-toluene remaining after irradiation from the peak area of the same product would provide a simple correction for the interference by the chemistry in the API source. At least two time dependent factors prohibit the use of such a simple correction factor. As the reaction proceeds in the irradiated reservoir, NO is converted to NO<sub>2</sub>. NO<sub>2</sub> reacts with OH 2.3 and 1.7 times faster than do NO and toluene respectively. Hence, the proportion of OH consumed by toluene would decline and an overcorrection would be made. Similarly, o-cresol, 7.3 times more reactive than toluene at 298°K, and other reaction vessel products would also compete significantly for the available OH in the corona region, again reducing

the fraction of OH consumed by toluene. An overcorrection would again result. The OH radical attack of D<sub>3</sub>-toluene must be suppressed before accurate photoproduct yields can be obtained.

Higher corona currents provide more OH radicals that produce more spurious product and related peaks. Depending on the particular product and on the irradiation time, consumption of the product or additional production from precursor compounds in the source could inflate or deflate the true yield. Interference in determining product yields would be greatest for true products formed through the abstraction pathway. To minimize these problems a corona current of 0.2  $\mu$ A is routinely used, the minimum current necessary to sustain a continuous discharge. If strategies to suppress the OH-toluene chemistry in the source were effective at higher corona currents, the advantage of slightly higher ion abundances at higher currents would be worth pursuing. This was not found to be the case.

#### IV.3.h) OH Scavenger Gas Addition

An ideal scavenger gas: 1) would not introduce new mass peaks into the spectra by its own ionization or through ionization of its products of reaction with OH, peaks which could interfere with or be misidentified as analyte peaks and which would decrease the dynamic range by consuming primary ions; 2) would not alter product yields by reacting with toluene, with the OH-toluene adduct, the H abstracted toluene radical or other radical intermediates, or with true products; and 3) would not corrode components of the API source and flow system. CO displayed none of these failings.

CO reacts with OH radicals only 0.038 times as rapidly as the same concentration of toluene (Table C.1). Hence, a concentration of CO considerably greater than that of the D<sub>3</sub>-toluene entering the API source was necessary.

Figure IV.5.a redisplays the mass spectrum in Figure IV.1.b (0.2  $\mu$ A corona current, no CO added) for comparison with the spectrum in Figure IV.5.b obtained with a 0.2  $\mu$ A current using 0.8% CO as an OH radical scavenger gas. The reaction rate of OH with CO should be  $3.4 \times 10^2$  times greater than that with toluene at their respective concentrations. Comparison of the peaks marked with dots indicates, as expected, strong suppression of the spurious products formed from D<sub>3</sub>-toluene in the API source, without the appearance of additional peaks. Also suppressed are peaks arising from OH radical attack of contaminants. Possible spurious product and spurious product related peaks of D<sub>3</sub>-toluene and of contaminants that have obviously been suppressed by CO addition are observed at m/z 46, 64, 74, 80-82, 85, 86, 97-100, 102, 103, 108, 110-118, 126-129, 141, 142, 144, 146, 158, and 159. Some of these peaks are primarily isotopic peaks of the preceding peak containing a <sup>13</sup>C atom. The peaks not suppressed are due primarily to protonated contaminants and related peaks.

Addition of 0.8% CO while using corona currents of 1 and 5  $\mu$ A did not suppress the D<sub>3</sub>-toluene-OH chemistry nearly as effectively. Adding greater than 5% CO caused new peaks to appear separated by 28 Dalton increments. For CO additions much less than 0.8%, the spurious product peaks reappeared. Hence, the recommended range of CO addition is 0.5 to 3%; this range is effective using the lowest sustainable corona current

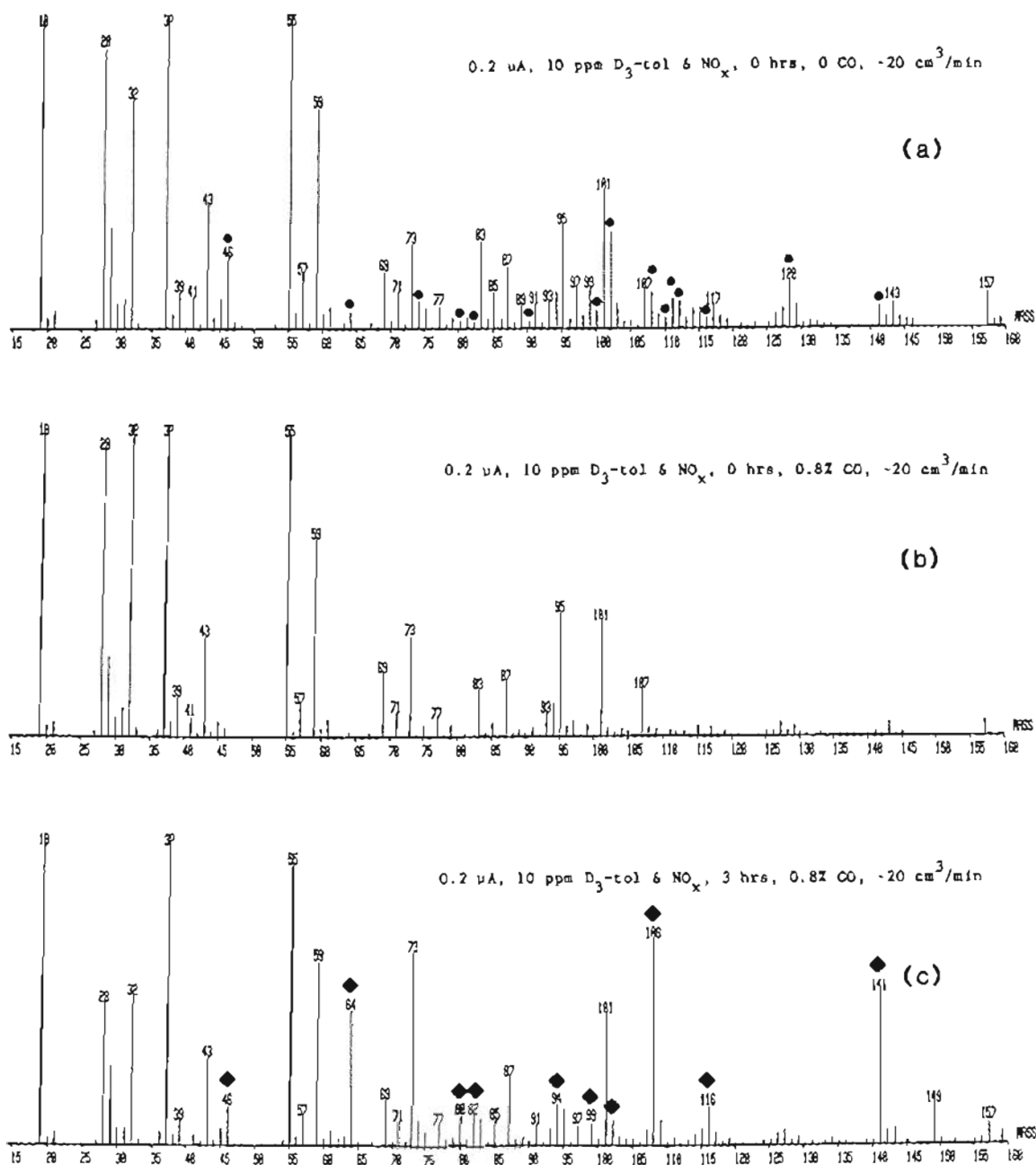


FIGURE IV.5. Four scan averages of mass spectra recorded using a  $0.2 \mu\text{A}$  corona current at the lower flow a) before irradiation and without CO addition; b) before irradiation and with 0.8% CO addition; and c) after irradiating the reservoir for 3 hrs and with 0.8% CO addition. Dots mark spurious product and related peaks. Diamonds denote true photooxidation product and related peaks from methyldeuterated toluene.

(0.2  $\mu$ A). Empirically, it is a simple matter to adjust the amount of CO added until the OH-chemistry interference disappears, while checking that no new peaks appear, before irradiating the reaction vessel.

#### IV.3.1) Appearance of True Photooxidation Products from Toluene

Figure IV.5.c displays a mass spectrum recorded after 3 hrs of irradiation with a 0.8% CO addition to the sample gas using a 0.2  $\mu$ A corona current. Comparing this spectrum to Figure IV.5.b shows large increases in the abundances for ions attributable to molecular, fragmented, and hydrated ions formed from photooxidation products of  $D_3$ -toluene listed by Dumdei and O'Brien (23): m/z 46 (a  $D_3$ -acylium ion, a fragment formed from methylketones), m/z 64 (protonated  $D_3$ -acetic acid), m/z 80 (protonated D-benzaldehyde fragment), m/z 82 (protonated  $D_3$ -acetic acid monohydrate), m/z 94 (?), m/z 102 (protonated  $D_3$ -4-oxo-2-pentenal), m/z 108 (protonated  $D_3$ -benzaldehyde), m/z 116, (protonated  $D_3$ -hydroxy-5-oxo-1,3-hexadiene), and m/z 141 (protonated  $D_3$ -nitro-toluene). There is no indication that the added CO diminishes the abundances of true products.

The peak at m/z 128, possibly due to protonated  $D_3$ -6-oxo-2,4-heptadienal (23) and so prominent in spectra without CO addition (Figure IV.1.b-d), is very minor in Figure IV.5.c. When using a corona current of 0.2  $\mu$ A, the effective temperature in the volume where spurious products are formed is not much above room temperature. Hence, spurious product yields in the source should bear a resemblance to product yields in the reservoir after some finite irradiation time. Adsorption or condensation onto the walls of the reservoir could decrease sensitivity

for this product. If this is the case, experiments in which the reservoir were heated to desorb products from the reservoir walls would produce a significant peak area at this  $m/z$  ratio.

#### IV.C.j) Alternate Flow Path for Neutral Species

With the additional orifice the flow through the API source increased four-fold. Figure IV.6.a-c displays mass spectra recorded, before irradiation, with a 0.2  $\mu\text{A}$  corona current, a) without CO added and with the lower flow, b) without CO added and with the higher flow, and c) with 0.8% CO added and with the lower flow. Comparing Figures IV.6.a and IV.6.b substantial reduction in the ion abundances of many spurious product and related peaks (again denoted by dots) is observed (e.g., at  $m/z$  46, 64, 100, 102, 108, 111, 128, 141). The extent of this reduction varies for different ions, e.g. the  $m/z$  102 ion shows the greatest reduction, while the  $m/z$  112 peak remains relatively unchanged. Appendix C provides a model to explain differences in suppression effectiveness with enhanced flow.

Remaining abundances at  $m/z$  46, 102, 112, 128, and 141 indicate addition of 0.8% CO (Figure IV.6.c) was more effective at suppressing peaks due to spurious products formed from  $\text{D}_3$ -toluene than was increasing the flow by a factor of four.

#### IV.3.k) Chemical Noise Suppression

Noise peaks derived from different sources will undergo different degrees of suppression. Contaminants at a fixed concentration in the gas stream entering the API source that become protonated could show an

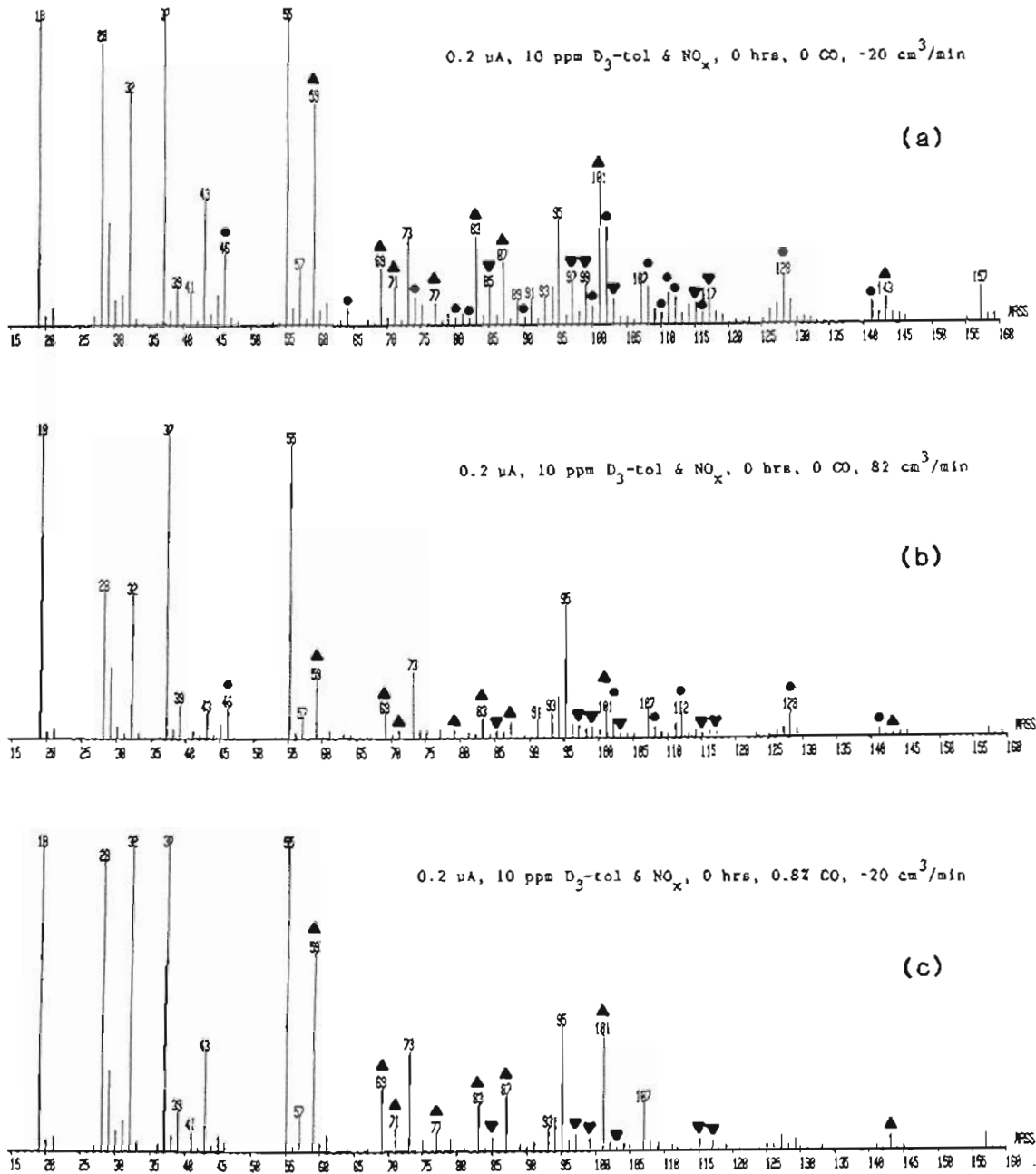


FIGURE IV.6. Four scan averages of mass spectra recorded using a 0.2  $\mu$ A corona current before irradiation a) without CO addition and with the lower flow; b) without CO addition and with the higher flow; and c) with 0.8% CO added and with the lower flow. Spurious product and related peaks are marked by dots and two types of chemical noise peaks are denoted by triangles (see text).

increase in ion abundance with increased flow or with scavenger gas addition. If the contaminant's rate constant for OH attack were large, the fraction ionized within the OH enriched region would increase; if this constant were small, the ion abundance would remain relatively constant. Ion peaks due to products formed in the source from a contaminant not readily protonated and present at a fixed concentration in the sample stream would show an across the board decrease in ion abundance when CO is added and differing degrees of reduction when the flow is increased as was observed for ion peaks arising from spurious products of toluene.

With increased flow, contaminants outgassed from surfaces at a constant rate will be present at one-fourth of their lower flow concentrations; hence, peaks due to these contaminants should decrease about four-fold relative to constant concentrations in the sample gas. A large enough flow would eliminate chemical noise due to contaminants outgassed at a constant rate and from their products formed in the API source; the residence time within the OH enriched volume for components in the sample stream would become too small for significant amounts of OH radical attack and subsequent ionization to occur.

Comparison of the spectra in Figure IV.6.a-c demonstrates that chemical noise arises from ionization of both contaminants and of spurious products generated by OH-contaminant chemistry. Noise peaks at  $m/z$  59, 69, 71, 77, 83, 87, 101, and 143 (right-side-up triangles) are suppressed most dramatically in the spectrum taken with the enhanced flow through the corona region. The contaminants primarily responsible for these noise peaks are most likely outgassed from surfaces at a



constant rate. Their remaining ion signals after CO addition indicate they were ionized directly.

Noise peaks at  $m/z$  85, 97, 99, 103, 115, and 117 (upside-down triangles) are substantially diminished in both the CO addition and alternate flow spectra. These noise peaks must be due primarily to products formed from OH attack of contaminants outgassed at a constant rate, since both suppression strategies are effective.

#### IV.3.1) Photooxidation Products from Toluene with Alternate Flow

Figure IV.7.a,b are mass spectra obtained after 3 hrs of irradiation using a 0.2  $\mu$ A corona current with a) the alternate flow configuration and b) 0.8% CO addition. Peaks at  $m/z$  46, 64, 80, 82, 94, 99, 102, 108, 116 and 141 due to photooxidation products produced in the reaction vessel display substantial growth in both spectra. The relatively small chemical noise peaks at  $m/z$  59 and 101 in the enhanced flow spectrum relative to any spectrum obtained with a lower flow are striking, and the peaks of interest stand out against the contaminant related peaks.

A greater increase in the flow through the corona region would further suppress chemical noise and spurious product peaks. This strategy would work best when unlimited sample volumes are available. An additional pumping line from the corona region to the outside of the vacuum housing of the mass spectrometer would permit large volumes of sample to be pumped through the corona region, while maintaining the CID region pressure at 1 Torr. For example, trace contaminant determinations in ambient air have been made with a corona discharge,

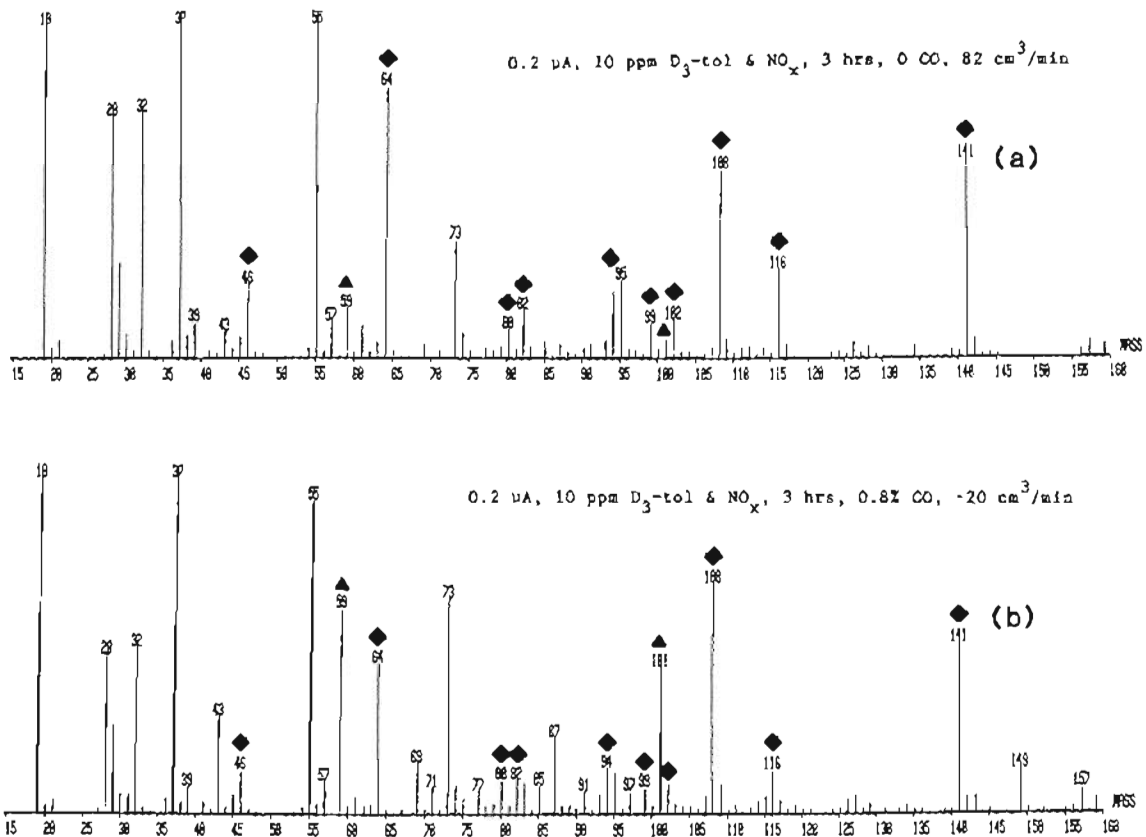


FIGURE IV.7. Four scan averages of mass spectra obtained after irradiating the reservoir for 3 hrs using a 0.2  $\mu$ A corona current a) with no CO addition and with the enhanced flow and b) with 0.8% CO addition and with the lower flow.

API source coupled with a triple quadrupole mass spectrometer utilizing a sample throughput of  $0.1\text{--}5\text{ L sec}^{-1}$  (24), 300 to  $1.5 \times 10^4$  times our normal flow. No problem with reactions in the API source was cited.

In the enhanced flow spectrum (Figure IV.7.a) the mass peaks corresponding to the highly polar compounds  $D_3$ -acetic acid ( $m/z$  64 and 82) and  $D_3$ -hydroxy-5-oxo-1,3-hexadiene ( $m/z$  116) are considerably larger relative to the peaks due to less polar D-benzaldehyde ( $m/z$  80 and 108) than in the  $OO$  addition spectrum (Figure IV.7.b). The enhanced signals obtained for the polar compounds suggest adsorption onto gas line walls is diminished with greater flows; less time is available for adsorption en route to the API source. Because the lower flow spectrum was recorded after the higher flow spectrum, the increased response was not due to saturation of the adsorption sites in gas lines leading to the corona region.

#### IV.4. CONCLUSIONS

OH radicals produced in the API source through the sequence of ion-molecule reactions that produces the primary reagent ions reacted with toluene to produce spurious products. Attack of toluene by OH radicals in the troposphere and in reaction vessels is the first step in toluene photooxidation. Hence, the chemistry occurring in the API source was a major interference when determining yields of products formed in the reaction vessel.

Three strategies reduced this interference to an insignificant level. First, the smallest sustainable corona current was used to limit the number of OH radicals produced. The portion of the total

ion current due to spurious product and related peaks was thereby minimized, while sacrificing a much smaller portion of the signals due to true products.

Second, addition of CO scavenged OH radicals and greatly suppressed OH attack of toluene without introducing new peaks into the mass spectra.

Third, a modest increase in the flow through the corona region reduced the residence time for neutral species in this region. Consequently, the yields of spurious products from D<sub>3</sub>-toluene and from contaminants undergoing OH attack were reduced. Also diminished were the signals from contaminants outgassed from surfaces at a constant rate. A significant gain in the signal-to-noise ratio resulted.

With our currently limited reaction vessel volume, still larger flows are not practical; use of a scavenger gas must remain our primary solution to the problem of unwanted chemistry occurring in the API source. These results, however, indicate a combination of scavenger gas addition and modestly increased flow through the corona region would substantially enhance our signal-to-noise ratio and enhance sensitivity for easily adsorbed compounds, while eliminating the problem of spurious product formation by OH radical attack.

## CHAPTER V

## DETECTION LIMIT AND DYNAMIC RANGE DETERMINATIONS

## V.1. INTRODUCTION

API mass spectrometry is capable of detection limits in the ppb to ppt range with a dynamic range of three or more decades for many compounds (25). A simple experiment was performed to estimate the limit of detection and dynamic range for benzaldehyde within the reservoir using our medium resolution API mass spectrometer and sample delivery method.

## V.2. EXPERIMENTAL SECTION

## V.2.a) Benzaldehyde Addition

A detection limit in the ppb range was anticipated based on the response seen with 0.14 ppm of benzaldehyde in the reservoir (Chapter III). Direct injection of the liquid into the reservoir inlet line would require a volume of  $5.5 \times 10^{-4}$   $\mu\text{L}$  for a 10 ppb addition of benzaldehyde. Because a 1  $\mu\text{L}$  syringe was the smallest available, such small volumes could not have been injected reproducibly. To surmount this limitation, without resorting to a more complicated system for adding benzaldehyde, a small amount of benzaldehyde was dissolved in a liquid that is relatively inert to positive ionization when using hydrated protons as the chemical ionization reagent. The insensitivity

for xylene observed in the resolution experiment utilizing these compounds (Chapter II) indicated that this compound would be an excellent solvent for this purpose. 11  $\mu\text{L}$  of benzaldehyde were added to 1.0 ml of m-xylene; injections of 0.05  $\mu\text{L}$  then corresponded to 10 ppb additions of benzaldehyde. For the first two of the last three additions, a 10  $\mu\text{L}$  syringe was used to add 5  $\mu\text{L}$  (1.0 ppm of benzaldehyde) and 7.5  $\mu\text{L}$  (1.5 ppm of benzaldehyde) of the mixture. For the last addition 0.115  $\mu\text{L}$  (2.1 ppm) of pure benzaldehyde was injected. After each addition the bottom of the U-shaped inlet (Figure III.1) was gently heated for 1 min to ensure complete evaporation of the liquid.

#### V.2.b) Mass Spectrometer Operation

To maximize sensitivity the slits were set to provide baseline resolution. The scan range was narrowed to 85-115 Daltons and 1 scan was obtained every 30 sec. The areas of the mass peaks were centroided and displayed as lines by the software. For each scan the voltage proportional to the area of the  $m/z$  107 peak was read on the cathode ray tube and recorded in a notebook. At least 16 min were required after each benzaldehyde addition before the last ten voltages displayed no systematic trends. The last ten voltages were then averaged to obtain a voltage proportional to the ion abundance for a given concentration of benzaldehyde. The current range of the electron multiplier amplifier was changed twice during data collection to accommodate the increasing signal due to additions of benzaldehyde.

A CID potential of 28 V provided maximum sensitivity for benzaldehyde. The test atmosphere containing 0.14 ppm of benzaldehyde

had shown a broad maximum in sensitivity between relative humidities of 17% and 24%. To operate on this broad maximum throughout this experiment, during which dilution of both the benzaldehyde and the relative humidity in the reservoir occurred, a reservoir gas/diluent ratio of 1:1.5 was used. With an initial relative humidity of 58% in the flask, the relative humidity of the sample gas initially supplied to the source was 23%. The flow through the source was  $21 \text{ cm}^3 \text{ min}^{-1}$ .

### V.3. RESULTS AND DISCUSSION

#### V.3.a) Response Curve and Detection Limit

Figure V.1 is a plot of the  $m/z$  107 ion abundance (arbitrary units) as a function of the concentration of benzaldehyde (ppb) added to the reservoir. The error bars represent two standard deviations above and below each point. Noise of a fixed amplitude becomes less important relative to the signal as larger ion abundances are recorded. Consequently, the error bars enclose a smaller range relative to the ion abundances as more additions are made; at high benzaldehyde concentrations the error range is smaller than the radius of the points in the figure.

The first point corresponding to 10 ppb of added benzaldehyde provides a signal-to-noise ratio of 2.6:1. Extrapolation of the line joining the first two points to a signal-to-noise ratio of 2:1 (marked by a triangle in Figure V.1) provides a detection limit of 8 ppb in the flask corresponding to 3 ppb in the API source under the source conditions of this experiment. It is the larger detection limit that is

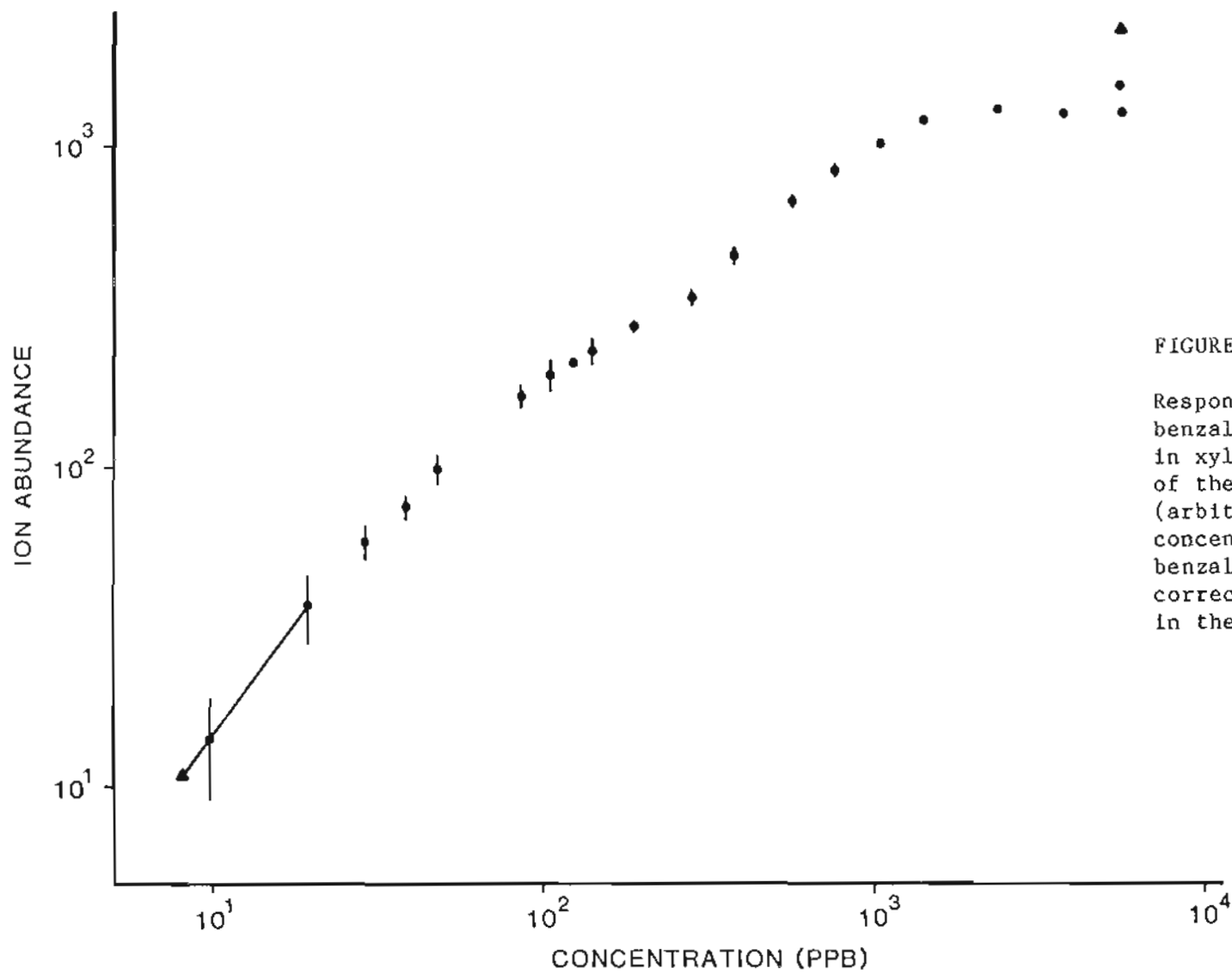


FIGURE V.1.

Response curve for benzaldehyde dissolved in xylene: abundance of the  $m/z$  107 ion (arbitrary units) vs concentration of benzaldehyde (ppb) corrected for dilution in the reservoir.



analytically important when this system is used to perform photooxidation experiments.

By the end of the experiment, the relative humidity had fallen to 16%. To determine the magnitude of the error introduced by this change, the dilution ratio was changed to 1:1.08 in order to increase the relative humidity in the sample gas to 20% for the last point after saturation had clearly been achieved. The difference in the ion abundances at the two humidities, corresponding to the distance between the two dots at the largest benzaldehyde concentration in Figure V.1, was small. This small difference indicates that the gradual change in relative humidity during the experiment did not significantly affect the shape of the benzaldehyde addition curve.

The reduction in concentration due to dilution of earlier additions of benzaldehyde was greatly mitigated by the increasing magnitude of successive additions. Before plotting the points corrections were made for dilution of all previous additions for each point; the largest correction in benzaldehyde concentration was  $< 7.5\%$ .

### V.3.b) Xylene Interference

Near the maximum in the response curve, curvature toward less sensitivity with additional benzaldehyde is expected as the number of analyte ions becomes significant relative to the number of primary reagent ions. But this curvature continues, even after saturation of the response curve occurs (slope = 0). At saturation all of the primary reagent ions protonate benzaldehyde molecules and further additions should have no effect. To determine if some of this curvature was due

to the increasing concentration of m-xylene, the last addition made was of pure benzaldehyde. This point shows no further decline, but rather, a small increase. This result suggests an increasing fraction of the precursor ions of the hydrated protons charge transfer to m-xylene. The dynamic range for analytes ionized by protonation decreases since fewer hydrated protons are formed.

This competition between m-xylene and water molecules for the precursor ions decreases the number of hydrated protons available to protonate benzaldehyde throughout the range of the response curve and could be responsible for the curvature toward less sensitivity throughout much of the range. This curvature is not normally expected for oxygenated analytes and was not observed by Sunner, et al. (33) for additions of acetone vapor over almost two decades.

To estimate the increase in dynamic range that would result if no xylene were present, the signals at m/z 106 and 107 (before the relative humidity was adjusted) were summed and plotted as the triangular point at the last addition (Figure V.1). Addition of signals from spurious products formed from xylene could further increase this sum, but such products were not monitored during the experiment. This triangular point illustrates that a wider dynamic range would be available in the absence of xylene; competition from other components in the sample gas for precursor ions of the hydrated protons (or for primary reagent ions) diminishes the dynamic range for a given analyte.

A small positive interference by xylene arises from molecular ions containing one  $^{13}\text{C}$  atom (m/z 107). This interference is readily estimated. For example, at the last point (Figure V.1) the xylene

signal at  $m/z$  106 was 34% of the  $m/z$  107 signal. The isotopic abundance of  $^{13}\text{C}_7\text{H}_{10}^+$  is 9% (46) of the  $\text{C}_8\text{H}_{10}^+$  abundance. Hence, only 3% ( $0.09 \times 0.34 \times 100\%$ ) of the  $m/z$  107 signal was due to xylene.

To avoid interference from xylene, standard additions of analyte vapor can be made into the sample gas line from a motor driven syringe containing the analyte liquid when the vapor pressure of the analyte at the syringe temperature is known (24). Maintaining the syringe below room temperature would prevent condensation of analyte vapor en route to the corona region.

### V.3.c) Adsorption

The increase in the slope of the curve starting with the twelfth point suggests an increase in sensitivity for benzaldehyde. This may occur due to a decrease in the importance of adsorption of benzaldehyde after later additions. The fraction of the adsorption sites for benzaldehyde that are occupied in the reservoir may approach 1, so that additional benzaldehyde resides in the gas phase; the lack of further adsorption results in an apparent increase in instrumental sensitivity.

Adsorption has been very apparent for acetic acid produced in the reservoir after a given irradiation time. In duplicate spectra separated in time by other data collection, ion abundances of other large peaks in the spectra displayed excellent reproducibility, while the acetic acid peak grew. This behavior most likely resulted from adsorption along the unheated parts of the gas lines leading to the corona discharge. As a greater fraction of the adsorption sites became occupied, the acetic acid en route to the AFI source was depleted less,

and more of it reached the corona discharge to provide a larger ion abundance.

Interference by adsorption on quantitation could be removed by using a flow through reservoir system (54,55) in place of the batch system currently used.

#### V.3.d) Operational Solution to Limited Dynamic Range

Despite the xylene interference and the dilution of benzaldehyde exiting the reservoir in order to lower the relative humidity of the gas entering the source, a dynamic range of two decades is apparent.

Figure V.1 indicates saturation when more than 1.5 ppm of benzaldehyde is in the reservoir; this corresponds to 0.6 ppm in the API source.

Assuming other oxidation products ionized by protonation have sensitivities similar to benzaldehyde, no more than -1.4 ppm of observable products (and contaminants) in the flask can be tolerated if saturation is to be avoided under conditions chosen to maximize sensitivity. When standard addition is to be used for quantitation, the total concentration of observable species must be less.

On the other hand, if conditions are made non-optimum, by increasing the dilution ratio, the dynamic range can be displaced to higher analyte concentrations in the reservoir. In addition, lowering the relative humidity would increase the population of smaller hydrated protons in the corona region. A greater number of smaller hydrated protons that protonate benzaldehyde and other oxygenated analytes would extend the responsive region of the dynamic range plot.

From the standpoint of simulating atmospheric conditions, the maximum sensitivity conditions should be used, since even then, the concentration of toluene in the flask will be much greater than that found in the southern California air basin during smog episodes, ~40 ppb (6). The experimental conditions actually used, however, will be determined primarily by the reservoir capacity and by the flow through the API source.

#### V.3.e) Source Modifications to Increase Dynamic Range

Two additional changes could extend the dynamic range. Heating the source, after first replacing the Vespel parts in the corona region to avoid domination of the mass spectra by phthalate associated peaks (Chapter II), would decrease the average size of hydrated protons in the source (36); greater availability of smaller hydrated protons would extend the responsive region of the plot. The absence of significant ion peaks at  $m/z$  19 and 37 would indicate all potential primary ions were consumed. As long as these peaks are significant, larger hydrated protons are reaching the CID region where they are disaggregated; only a portion of the smaller hydrated protons formed protonate additional analyte molecules. Operating conditions which minimize the  $m/z$  19 and 37 peaks would extend the dynamic range at the high end by providing additional primary ions.

Very recently, Sunner et al. (35) observed 15- and 42-fold greater sensitivities for benzaldehyde and acetone when they heated their sample gas (33% relative humidity) to temperatures of  $-250^{\circ}\text{C}$  with a spiral heater made from Nichrome wire. Providing photooxidation products are

not subject to thermal decomposition at such moderate temperatures or upon contact with the heater coil, heating the undiluted reservoir gas (or source) could avoid the need to reduce the number density of water molecules in the source, and hence, of analyte molecules as well. At the very least, the detection limit would be decreased by the inverse of the dilution ratio for which sensitivity is maximized using our flow system.

To further decrease the detection limit a greater number of ions must enter the mass analyzer for a given concentration of benzaldehyde in the source. To accomplish this a greater fraction of the ions formed in the source must exit through the first orifice into the CID region. Surrounding the corona needle with a metal sleeve maintained at the corona tip potential and insulated from the API body would prevent ions from striking the cylindrical walls of the corona region; more ions would be directed toward the first orifice.

Should more ions enter the CID region steps may be necessary to ensure a greater number of ions also enters the mass analyzer. A twenty-five fold increase in the corona current resulted in only a 40% increase of the total ion current for the mass spectra obtained (Chapter IV). If spreading of the ion beam in the CID region due to electrostatic repulsion between the ions is responsible for this observation, the addition of a lens between the orifices could direct more ions through the second orifice. Caldecourt (43) observed a twenty-fold increase by doing so; an attempt early in our development of the API source to duplicate his configuration did not result in such an increase. Experiments using a circular aperture lens in the CID region

over ranges of potential and location along the ion beam axis should be performed to determine if sensitivity can be enhanced. Feedthroughs are available in the source block and source-housing flange for this purpose.

#### V.3.f) Standard Addition

After irradiating 10 ppm of H<sub>8</sub>-toluene in the reservoir for 23.3 hr, two standard additions of 200 ppb of benzaldehyde in m-xylene were made to provide an estimate of the benzaldehyde concentration. The m/z 107 signals after 200 and 400 ppb additions of benzaldehyde provided estimates of 99 and 89 ppb for the concentration of benzaldehyde in the reservoir. Correcting for the 15% dilution of all flask contents prior to these standard additions, these estimates correspond to 116 and 105 ppb of benzaldehyde in the absence of dilution. At the large reservoir gas/diluent ratio (1:8) used in this experiment, the concentration of benzaldehyde in the source was 11-55 ppb for 0-400 ppb additions of benzaldehyde, a concentration range well within the responsive region observed at a higher relative humidity (Figure V.1).

A theoretical estimate of the benzaldehyde concentration expected in the reservoir after 23.2 hrs of irradiation, in the absence of dilution, is made in Appendix D for comparison. The good agreement between the theoretical and standard addition estimates of the benzaldehyde concentration (0.15 ppm vs 0.116 and 0.105 ppm) indicates standard additions are feasible for quantitation of products in the reservoir. Adsorption of benzaldehyde on the reservoir and gas line surfaces may account for most of the difference between these values. As noted

above, a flow through system would eliminate this source of error.

Possible photolysis of benzaldehyde, ignored in the above calculation, would also decrease the benzaldehyde concentration in the reservoir, but uncertainty remains as to its importance (5).

### V.3.g) Optimal Toluene Concentration

The greatest toluene concentration that avoids saturation by photooxidation products should be used to maximize the concentrations, and hence, the detectability, of minority products. This optimum initial concentration of toluene will depend on the sample gas dilution ratio. The dilution of reservoir contents occurring over time would allow a higher initial concentration of toluene to be used, since many hours of irradiation are necessary before the sum of the ion signals from products is maximized.

We have generally used an initial toluene concentration of 10 ppm in the reservoir, a CID potential of 28 V, and a dilution ratio of 1:8 by dry zero air for the sample gas. This 5.3-fold greater dilution than under the conditions used to collect data for Figure V.1 should shift the dynamic range by about the same factor; the saturation limit would be -8 ppm. Providing the yield of protonatable products never exceeds 80% during an irradiation experiment, this concentration will not cause saturation. Because cresol, a non-protonatable product when using water as the chemical ionization reagent, is produced with a yield of -20% (9) and because CO and CO<sub>2</sub> are important non-protonatable products, an 80% yield of protonated ions may not be produced. The 200 and 400 ppb standard additions of benzaldehyde provided reasonably similar estimates



of the benzaldehyde concentration in the flask after 23.3 hrs of irradiation indicating saturation was not a problem. Hence, starting with 10 ppm of toluene does not cause saturation under these operating conditions. The optimum initial toluene concentration may be significantly higher than 10 ppm and must be found experimentally for these or any other operating conditions.

#### V.4. CONCLUSIONS

The response curve for benzaldehyde displayed a dynamic range of two decades and standard additions of benzaldehyde after a long irradiation period provided reasonable estimates of the benzaldehyde concentration in the reaction vessel. Hence, quantitation of components in a simulated atmosphere by standard additions is feasible with our system. Direct vapor injection into the sample gas could provide a more linear response curve.

The appearance of the response curve for an analyte in a mixture of ionizable compounds could differ from that observed in their absence; simulated atmospheres should be investigated for this possibility. In addition, saturation will occur at a lower concentration of the analyte due to consumption of primary reagent ions and of precursor ions by the other components.

## CHAPTER VI

APPLICATION OF MEDIUM RESOLUTION APIMS TO  
TOLUENE PHOTOOXIDATION STUDIES

## VI.1. INTRODUCTION

At a given nominal mass, medium resolution generally permits separation of multiple peaks having different molecular formulae. Multiple peaks due to contaminant, reactant, product, isotopic, hydrated, or fragmented ions are observed at many nominal masses. Determination of an exact mass for each separated peak provides a molecular formula for each ion. Changes in ion abundances when the CID potential is varied then permit molecular, hydrated, and fragmented ions to be differentiated.

Two  $m/z$  ratios for which more than one product having different molecular formulae had been identified in past toluene photooxidation experiments were targeted for study to determine if these products were artifacts of the concentration or separation procedures used. If present in the gas phase, medium resolution would permit exact mass assignment to the peaks and provide confirmation for their production during toluene photooxidation.

## VI.2. EXPERIMENTAL SECTION

### VI.2.a) Test Atmosphere and Sample Gas

The test atmosphere contained 10 ppm of H<sub>8</sub>-toluene and 10 ppm of NO<sub>x</sub> in zero air having a nominal relative humidity of 58% (Chapter III). A CID voltage of 28 V was used unless otherwise specified with a reservoir gas:dry zero air dilution ratio of 1:8. These conditions provided good sensitivity, minimized the abundances of hydrated ions while avoiding excessive fragmentation of molecular ions, and minimized dilution of the reservoir contents over time.

Addition of CO to the sample stream using a flow meter could not be made due to the failure of an electrical component in the flow meter immediately prior to the experiment. A syringe drive system was used instead to supply 0.3 cm<sup>3</sup> min<sup>-1</sup> of pure CO; this corresponded to 1.3% of the 23 cm<sup>3</sup> min<sup>-1</sup> flow through the API source and flow system vent (Chapter III). Even with this CO supply, the m/z 107 peak was slightly larger than the m/z 92 peak before irradiation; increasing the syringe drive rate did not diminish it. Because the dynamic range determination for benzaldehyde (Chapter V) in which 6 ppm of benzaldehyde was present in the reservoir at the end of the experiment was performed the day before, a small amount of benzaldehyde still present in the flow system was probably contaminating the sample gas. This contaminant is a toluene photooxidation product but should not have interfered with qualitative observations of peak growth for other products.

### VI.2.b) Mass Spectrometer Operation

The entrance slit was narrowed to transmit one-third of the open slit signal; then the exit slit was set to provide half of the remaining signal. This provided a resolution of  $\sim 2,800$  with a  $< 1\%$  valley while retaining one-sixth of the maximum ion signal (Chapter II). To maximize sensitivity, the second most sensitive range of the electron multiplier amplifier was used (the most sensitive range was judged to be too noisy).

To determine exact masses, the KVE scan mode of the instrument was used. The magnet current is held constant while the accelerating voltage is reduced from an initial value of 6 kV to provide a linear scan starting at low mass. To provide this scanning capability it was necessary to use the VG 7070's power supply to provide the accelerating potential and half-plate potentials in place of the independent 10 kV power supply; no arcing problem accompanied this substitution. The much greater reproducibility obtained versus scans for which the magnet current is varied allows the data from numerous scans to be summed without major peak dislocations. Twenty-five scans recorded at 10 sec/mass decade were summed to smooth noise fluctuations relative to single mass spectra taken at a slower scan rate; this practice may degrade the resolution slightly. Raw data was collected, i.e. the data acquisition system was not used to centroid the peaks and display line spectra.

Mass spectra were recorded after irradiation times in the range of 0 to 1322 minutes. Two scan ranges were used, 73-93 and 89-111 Daltons.

Because the  $m/z$  97 and 99 peaks were the primary focus of this experiment, eight summed spectra were recorded after 0, 20, 66, 91, 191, 300, 1100, and 1322 minutes of irradiation for the higher mass range, while only four summed spectra were recorded for the lower range after 0, 1142, 1147, and 1313 minutes of irradiation. Figure VI.1 displays one of the higher range spectra and two  $m/z$  ratios for which the time (x) axis has been expanded.

The CID voltage was reduced to 19 V for the 1142 minute spectrum to look for hydrated ion peaks; less disaggregation causes such peaks to grow relative to non-hydrated peaks. Alternatively, for the 91 minute spectrum the CID potential was increased to 37 V; in this case, greater disaggregation causes such peaks to shrink relative to non-hydrated ion peaks.

Exact mass assignments were made using the  $m/z$  73, 92, and 107 peaks due to a hydrated proton ( $(\text{H}(\text{H}_2\text{O})_4)^+$ ), toluene ( $(\text{C}_7\text{H}_8)^+$ ), and protonated benzaldehyde ( $(\text{C}_7\text{H}_7\text{O})^+$ ) respectively for calibration; the first two peaks were used to calibrate the lower mass range, the latter two  $m/z$  peaks were used to calibrate the summed spectra for the higher mass range. Standard deviations of the exact masses were calculated for the spectra taken after irradiation had begun (up to seven spectra for the higher mass range, depending on which spectrum first displayed the peak, and three spectra for the lower range). The exact mass errors reported are  $\pm$  two standard deviations.

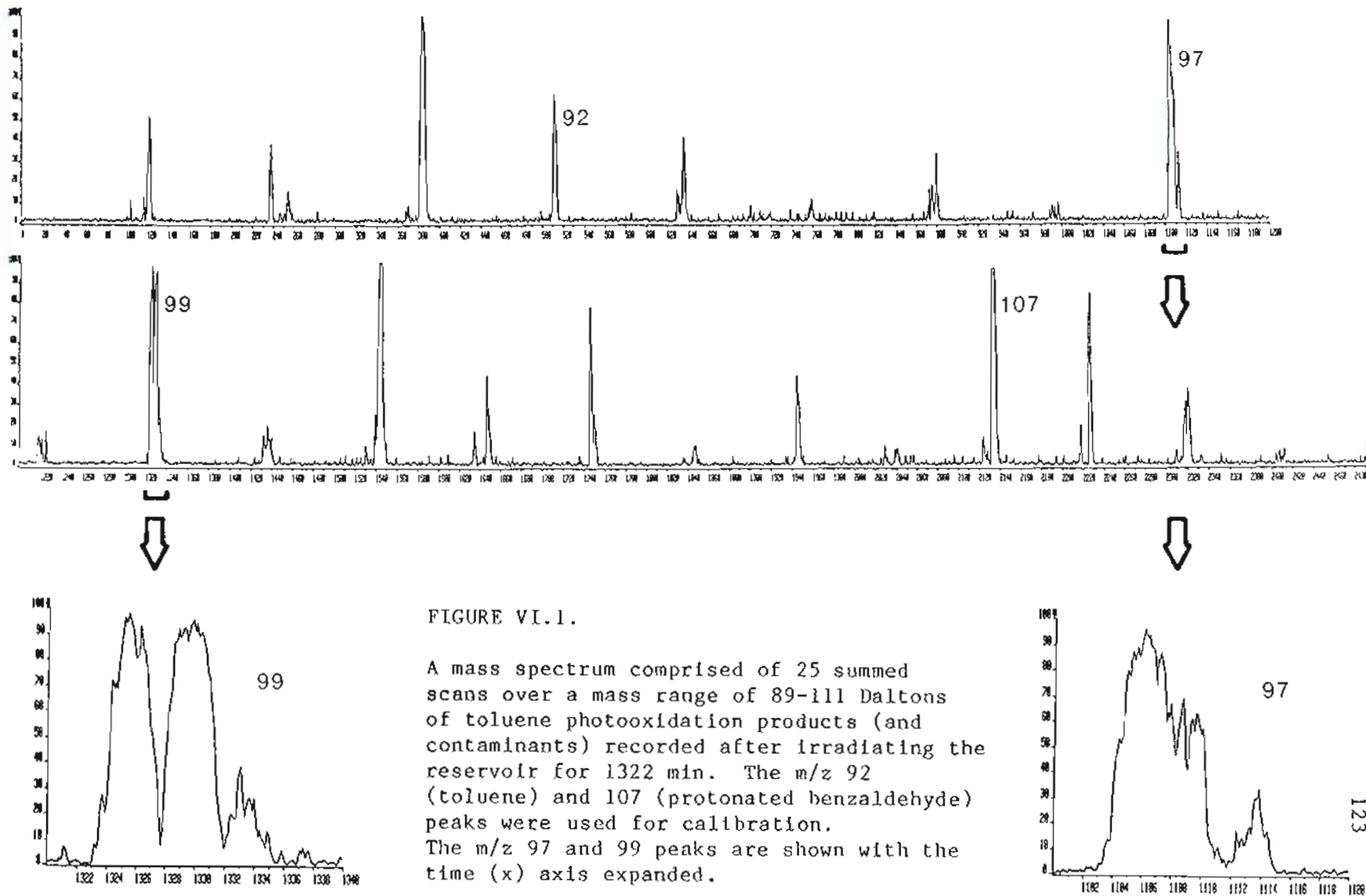


FIGURE VI.1.

A mass spectrum comprised of 25 summed scans over a mass range of 89-111 Daltons of toluene photooxidation products (and contaminants) recorded after irradiating the reservoir for 1322 min. The  $m/z$  92 (toluene) and 107 (protonated benzaldehyde) peaks were used for calibration. The  $m/z$  97 and 99 peaks are shown with the time (x) axis expanded.

### VI.3. RESULTS AND DISCUSSION

#### VI.3.a) Toluene Photooxidation Products Found in Past Studies

O'Brien et al. (19) irradiated for 24-30 hr, a 22 L flask containing zero air having a relative humidity of 50% to which up to 10 ppm of  $\text{NO}_x$  and up to 10 ppm of toluene, methyl deuterated toluene, or perdeuterated toluene had been added. They rinsed the flask with dichloromethane to collect the products, evaporated this solvent to a small volume to concentrate the products, and then inserted a glass vial containing 10% of the concentrate into a triple quadrupole mass spectrometer with a direct probe. Positive chemical ionization by  $\text{CH}_5^+$  ions generated from methane produced  $\text{M}+\text{H}^+$  ions from toluene and both aromatic and ring fragmentation products. Daughter ions observed by tandem mass spectrometry from the  $\text{H}_8^-$ ,  $\text{D}_3^-$ , and  $\text{D}_8^-$ -toluenes provided evidence that the  $\text{M}+\text{H}^+$  product peak at  $m/z$  97 was due to protonated 5-oxo-1,3-hexadiene ( $\text{C}_6\text{H}_9\text{O}^+$ ). The exact mass of this ion is 97.0653 Daltons.

Shepson et al. (14) irradiated for 10 minutes, a test atmosphere of dry air containing 7 ppm of toluene, 5 ppm of NO, and 9 ppm of methyl nitrite that was added to increase the OH concentration induced by irradiation. They determined the photooxidation products of toluene with gas chromatography - electron impact mass spectrometry after first collecting and concentrating them in a cold trap. Two products with a molecular weight of 96 Daltons were found, furfural ( $\text{M}+\text{H}^+ = \text{C}_5\text{H}_5\text{O}_2^+$ ; exact mass = 97.0290 Daltons) and an unknown compound that was assigned the same molecular formula based on the abundance of the molecular ion containing one  $^{13}\text{C}$  atom. Because the electron impact mass spectrum of

this compound was similar to the daughter ion spectrum for the O'Brien group's compound, they may have been the same.

O'Brien et al. also identified 4-oxo-2-pentenal ( $M+H^+ = C_5H_7O_2^+$ ; exact mass = 99.0446 Daltons) as a product, while Shepson et al. found a compound of the same molecular formula, 3,4-dioxo-1-pentene. Bandow et al. (15) reacted 4 ppm of toluene and 0.7-3.0 ppm  $NO_x$  in dry air and irradiated the mixtures for 217 min. They employed long-path fourier transform infrared absorption spectroscopy to study the contents of the reservoir in situ. After subtracting contributions by several products from a composite infrared spectrum, they identified maleic anhydride ( $M+H^+ = C_4H_3O_3^+$ ; exact mass = 99.0082 Daltons) as a product from the difference spectrum.

### VI.3.b) Medium Resolution API Mass Spectra of Toluene Photooxidation Products

The mass spectra in Figure VI.2 display multiple peaks observed at  $m/z$  97 after the irradiation times cited above. The x axis displays time units; the corresponding masses increase from left to right. A shift toward lower time units occurred for spectrum VI.2.f, resulting perhaps, from a slightly different magnet current during this scan. Because exact masses in each spectrum are determined relative to two standard peaks within that spectrum, this time scale shift is not important.

The peak at the extreme right is a background peak; no growth is observed during irradiation. The extreme left peak, however, clearly grows very early during the irradiation, while the middle peak grows



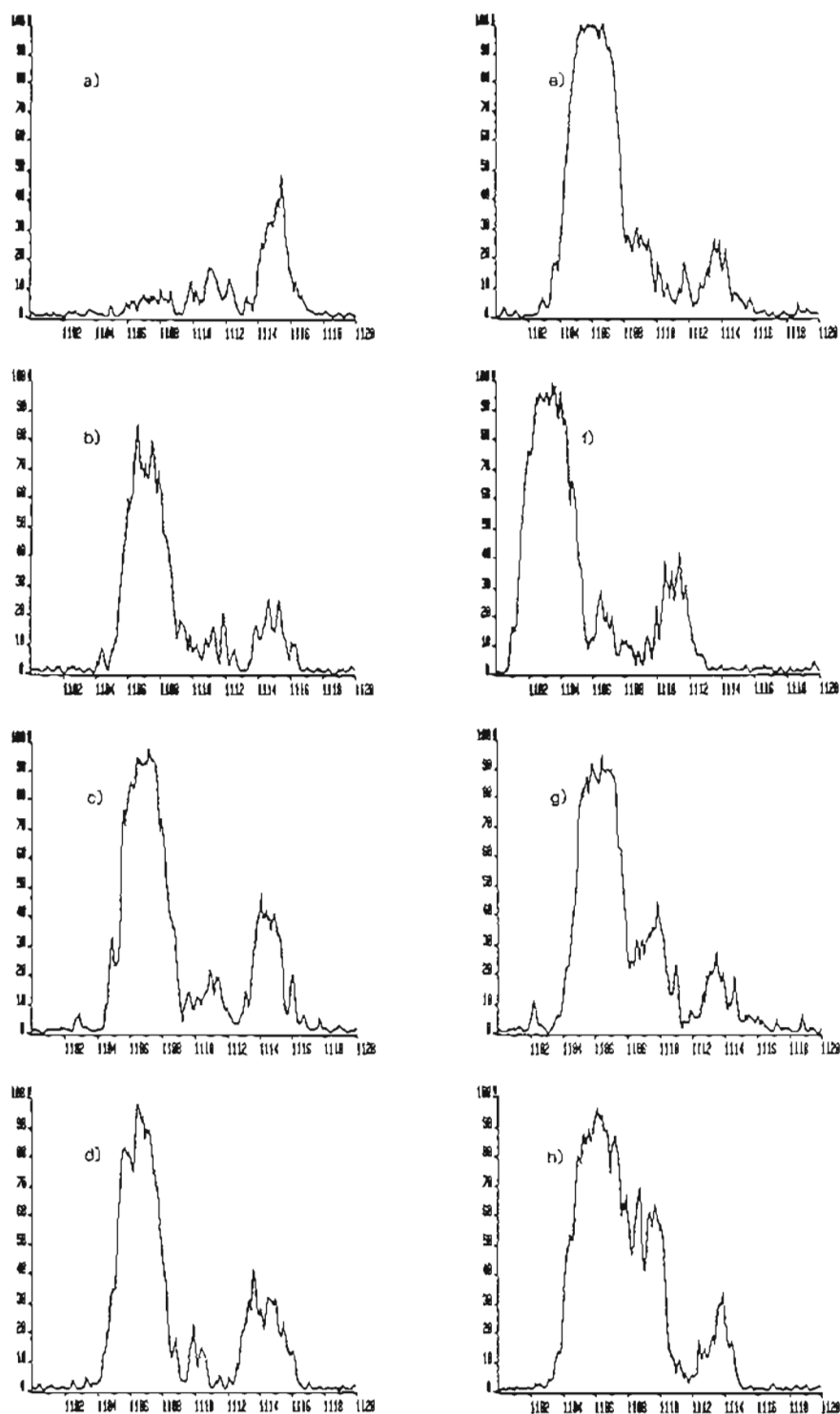


FIGURE VI.2. Mass spectra recorded at  $m/z$  97 after irradiating the reservoir for a) 0 min, b) 20 min, c) 66 min, d) 91 min, e) 191 min, f) 300 min, g) 1100 min, and h) 1322 min. The CID potential was 28 V for a)-c) and e)-h); 37 V for d).

more gradually; this behavior suggests these peaks are due to products of toluene photooxidation. The exact masses for these two peaks were determined to be  $97.0290 \pm 0.0028$  Daltons (extreme left peak) and  $97.0564 \pm 0.0108$  Daltons (middle peak). The exact mass for the less intense peak was determined from the last four spectra, the only spectra in which this peak was observable above the middle background peak. Not surprisingly, the precision for the exact mass determination of this peak is poorer than for the intense peak which appeared in all seven spectra recorded during irradiation. The exact mass of the left peak agrees very well with the mass of the protonated ion of furfural. The exact mass of the middle peak agrees within two standard deviations with the mass of protonated 5-oxo-1,3-hexadiene. Interference from the much larger peak to its left may have shifted this peak's maximum to the left.

Multiple peaks also appear in the mass spectra recorded after the same irradiation times at  $m/z$  99 in Figure VI.3. The extreme right peak shows little or no growth and is a contaminant peak. The exact masses of the two peaks showing substantial growth are  $99.0079 \pm 0.0020$  Daltons (left peak) and  $99.0447 \pm 0.0014$  Daltons (middle peak). These values agree very well with the masses of the protonated ions of maleic anhydride and 4-oxo-2-pentenal or 3,4-dioxo-1-pentene respectively.

These spectra provide evidence that the compounds found in the previous studies were present in the gas phase before concentration or separation steps were performed.

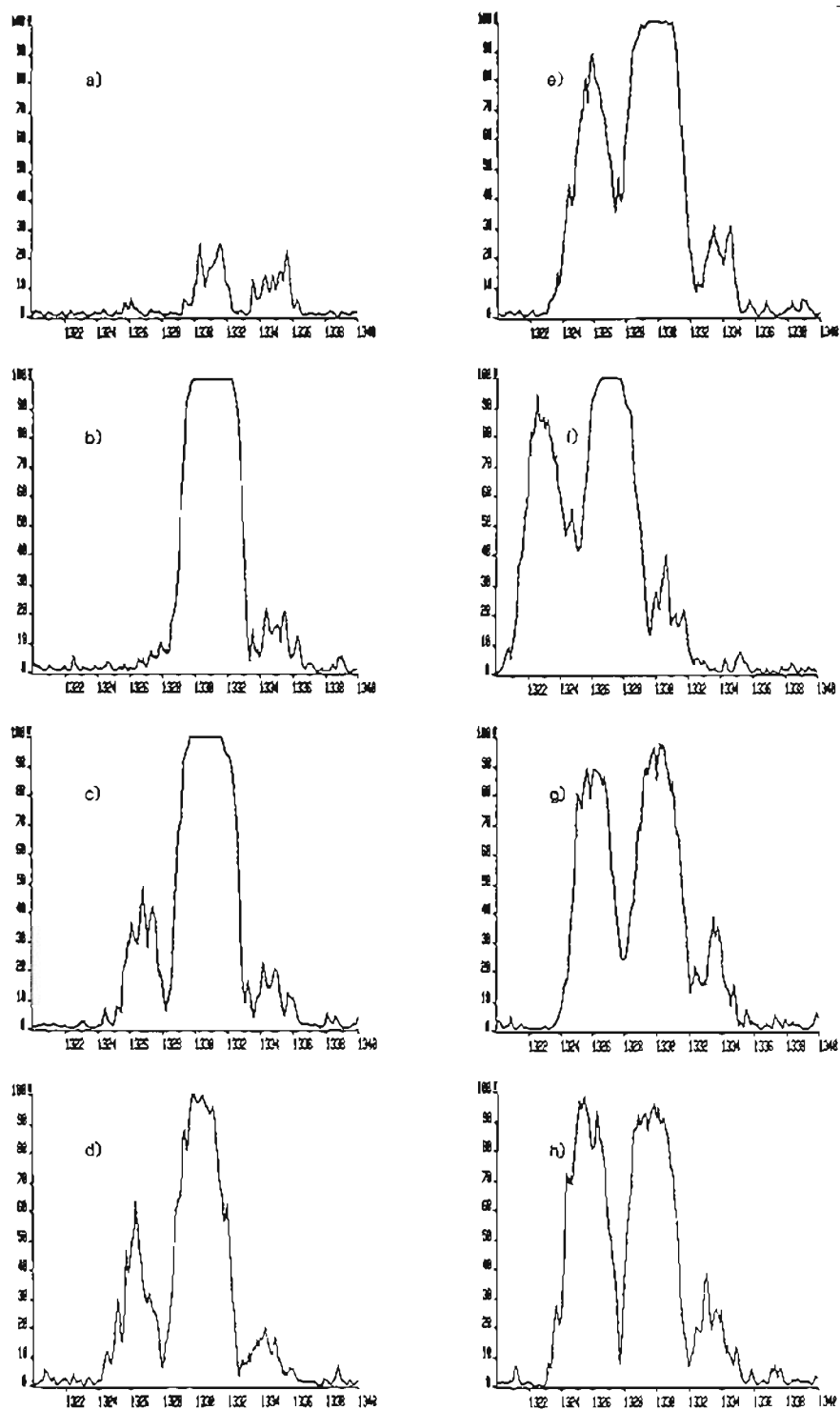


FIGURE VI.3. Mass spectra recorded at  $m/z$  99 after irradiating the reservoir for a) 0 min, b) 20 min, c) 66 min, d) 91 min, e) 191 min, f) 300 min, g) 1100 min, and h) 1322 min. The CID potential was 28 V for a)-c) and e)-h); 37 V for d).

### VI.3.c) Desorption vs Product Generation

The extremely rapid growth of peaks at  $m/z$  97 and 99 after only 20 minutes of irradiation causes suspicion that these peaks may arise from desorption of contaminants from the reservoir walls or of photooxidation products generated in previous experiments from the unheated portion of the gas line between the reservoir and heated section of the line. Desorption could occur once the sixteen 40 watt black lights are turned on; the temperature within the flask rises several Celsius degrees despite the airflow about the flask generated by a 160 cfm fan. Continued growth in the largest  $m/z$  97 peak through an irradiation time of 191 min provides evidence that one or more gas phase products are also responsible for some of the peak area. For the largest  $m/z$  99 peak, however, gradual shrinkage after 20 min of irradiation is observed. Hence, the growth of ion peaks with time provides evidence for the presence of compounds in the gas phase having the molecular formulae of 5-oxo-1,3-hexadiene, one or both of the Shepson group's compounds with a molecular formula of  $C_5H_4O_2$ , and maleic anhydride. The lack of observable peak growth due to massive interference from a desorbed compound prevents any conclusion concerning the presence or absence of 4-oxo-2-pentenal and 3,4-dioxo-1-pentene from being made.

### VI.3.d) Peak Separation in Kinetic Studies

These spectra (Figures VI.2 and VI.3) illustrate the importance of peak separation for kinetic studies. Different products will be generated from toluene and consumed by OH attack or photolysis at

different rates. In future experiments the increase and eventual decrease in areas of each of the multiple peaks with irradiation time could be followed using medium resolution; were only unit resolution available, a composite signal would be observed, which could not be interpreted.

#### VI.3.e) Identification of Hydrated Ions

Figure VI.4 displays mass spectra for  $m/z$  85 after 0, 1142, 1147, and 1313 minutes of irradiation. (A different software parameter for the zero time spectrum accounts for the different time units for this spectrum). Only the extreme left peak displayed significant growth. Its exact mass was determined to be  $85.0239 \pm 0.0072$  Daltons; that for the  $M+H^+$  ion of butenedial, identified as a toluene photooxidation product by both the Shepson and O'Brien groups (14,23), is 85.0290 Daltons. The lack of spectra for short irradiation times prevents conclusions from being made as to whether this peak is due to products or contaminants.

A peak at  $m/z$  103 grew in Figure VI.5 over the eight irradiation times available for the higher mass range. The molecular formula for this peak was found to be  $C_4H_7O_3^+$  ( $103.0401 \pm 0.0015$  vs 103.0395 Daltons) which could arise from either monohydrated butenedial or from hydroxy-3-oxobutanal, a compound identified by Dumdei et al. (23). The spectrum taken with an applied CID potential of 37 V (Figure VI.5.d) shows substantial shrinkage in the peak area which indicates that a hydrated ion is most responsible for this peak. Non-hydrated peaks did not show shrinkage (e.g.,  $m/z$  97 and 99 in Figures VI.2.d and VI.3.d)

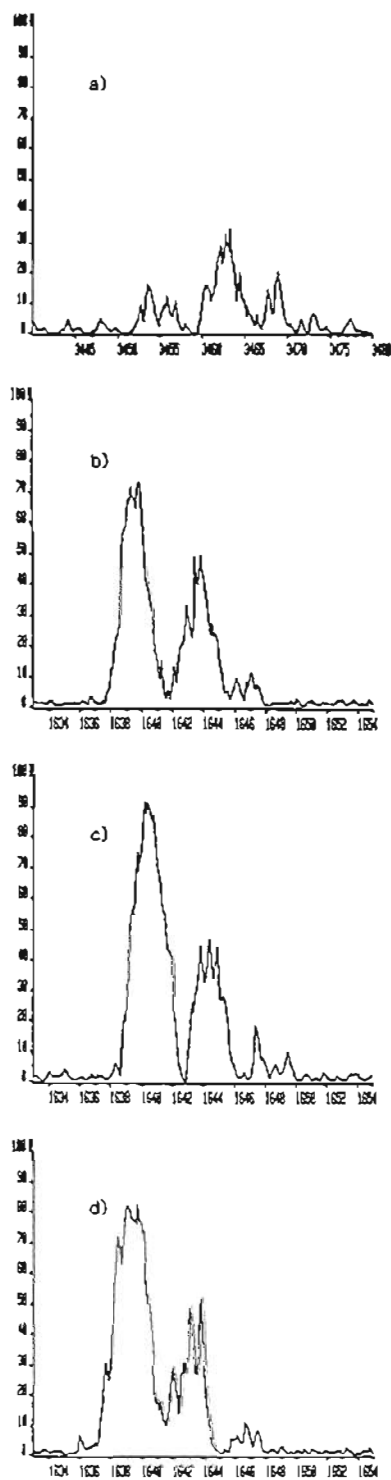


FIGURE VI.4. Mass spectra recorded at  $m/z$  85 after irradiating the reservoir for a) 0 min, b) 1142 min, c) 1147 min, and d) 1313 min. The CID potential was 28 V for a), c), and d); 19 V for b).

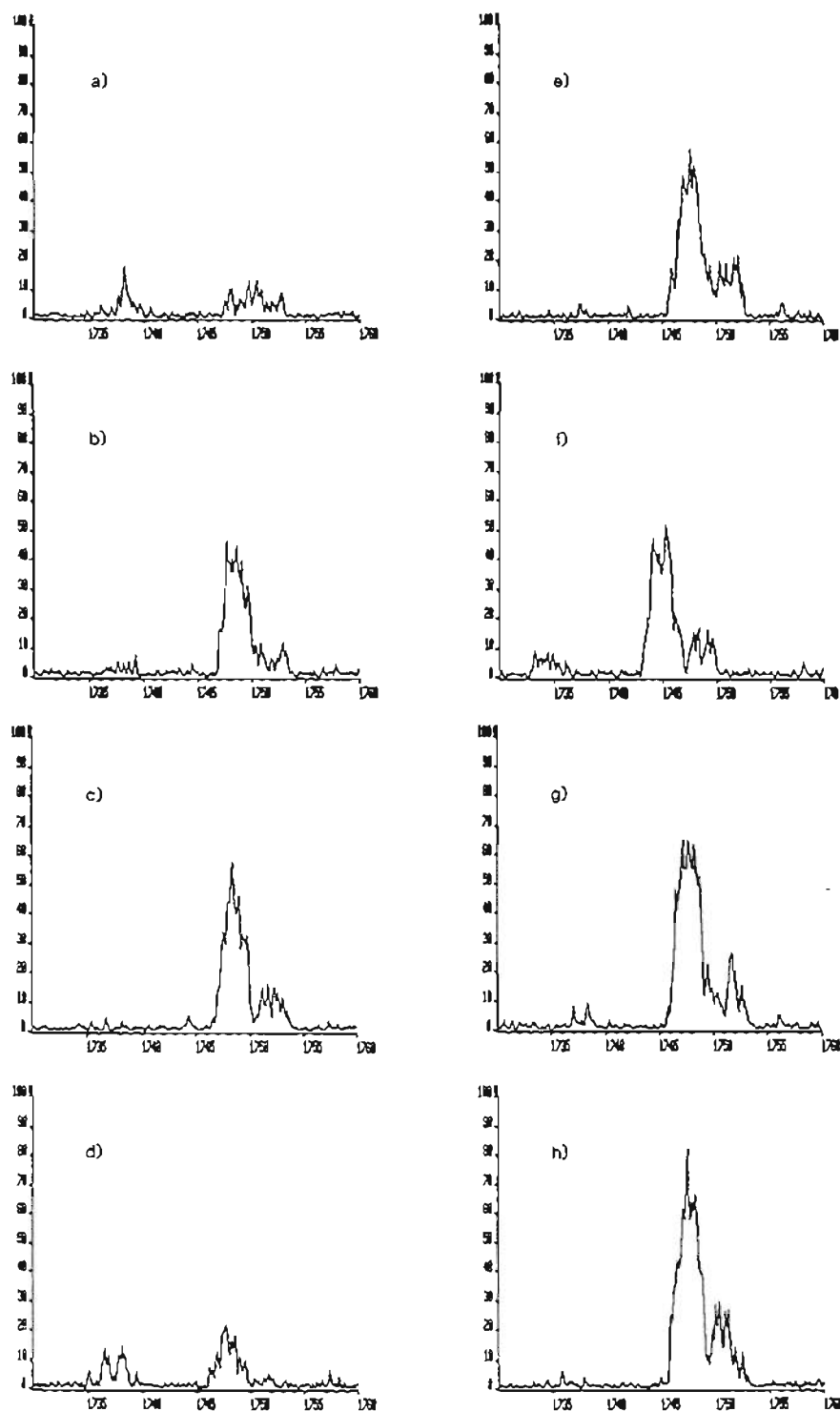


FIGURE VI.5. Mass spectra recorded at  $m/z$  103 after irradiating the reservoir for a) 0 min, b) 20 min, c) 66 min, d) 91 min, e) 191 min, f) 300 min, g) 1100 min, and h) 1322 min. The CID potential was 28 V for a)-c) and e)-h); 37 V for d).

since the CID potential was not high enough to induce significant fragmentation. In addition, the small peak to the right of the large peak also appears to be due to a hydrated ion, while the very minor peak to the left of these peaks does not. The two hydrated ions correspond to the two  $m/z$  85 peaks in Figure VI.4. The rapid growth seen after only 20 minutes for the largest  $m/z$  103 peak indicates that it, as well as the bare  $m/z$  85 ion, could be due in part to a contaminant with the same molecular formula as butenedial outgassed from the reservoir with heating. The continued growth in area of the  $m/z$  103 peak suggests the  $m/z$  85 ion is partly due to a photooxidation product of toluene.

#### VI.3.f) Peak Separation in Daughter Ion Studies

These examples illustrate the power of medium resolution API mass spectrometry for separating isobaric peaks present at trace levels in a gas mixture as well as the prevalence of multiple peaks; within the range recorded, most nominal masses displayed two or more peaks (Figure VI.1). Ideally, one would like to produce a daughter ion spectrum for each separated parent ion, since the molecular formula alone does not divulge the structure of an ion. The link scan capability of the VG 7070E-HF instrument is insufficient to accomplish this due to the inefficiency of daughter ion collection (< 1%) inherent with such instruments. Triple quadrupole instruments have ion collection efficiencies up to 65% (56) but only unit resolution for both the parent and daughter ions; isobaric parent ions cannot be separated (57). Prior separation by chromatographic techniques introduces the possibility of



sample alteration by chemical reaction. Perhaps the ideal instrument for studying atmospheric reactions would be our instrument with a double quadrupole attached after the exit slit. With this commercially available addition (58) the instrument would provide sufficient resolution to separate most isobaric parent ions. Deacceleration before collision in the first quadrupole would assure efficient daughter ion focusing into the second quadrupole, which would provide the daughter ion spectra.

#### VI.3.g) Deuterated toluene

Molecular formulae determined with medium resolution can often correspond to more than one isomer. Inducing fragmentation of molecular ions by increasing the CID potential when studying a mixture of compounds is not usually helpful for distinguishing between isomers; it can be impossible to correlate the fragments with their parent ions. Structural information about products from molecular formulae alone can be gained, however, by performing irradiation experiments using deuterated toluenes. For example, using methyl deuterated toluene, the  $m/z$  103 peak would again appear if due to monohydrated butenedial or a contaminant, but any ion abundance due to hydroxy-3-oxobutanal would shift to  $m/z$  106. Similarly, if 2-pentene-1,4,-dione contributes to the large  $m/z$  99 peak, use of  $D_3$ -toluene would shift its protonated ion peak to  $m/z$  102. To confirm the identity of a peak attributed to a toluene photooxidation product in the mass spectrum obtained using any of the toluenes, peaks must be found at the appropriate exact masses in the spectra recorded using the other toluenes to rule out contamination or

other interferences as the source of the peak. When a product peak generated from one toluene is overlapped by other peaks, the corresponding product peak generated from the other toluenes will usually be shifted to a  $m/z$  ratio with less interference for one or both of the other toluenes. In addition to the methyldeuterated ( $D_3$ ) and perdeuterated ( $D_8$ ) toluenes used by the O'Brien group, ring deuterated ( $D_5$ ) toluene is commercially available (59) and would provide another set of even numbered  $m/z$  ratios for toluene photooxidation products.

#### VI.3.h) Other Possible Product Peaks

Table VI.1 lists the exact masses for products identified by the three aforementioned groups over a  $m/z$  range of 73-111 Daltons. Peaks that grew during irradiation corresponding to the protonated ions for these compounds are indicated. A possible additional product is included in the table ( $m/z$  89). Correlation with medium resolution peaks from future experiments using deuterated toluenes would confirm or refute its production from toluene.

#### VI.3.i) Products Not Detected

No peaks for phenol or cresols were observed. The yield for cresols should be ~20% (9). Dumdei et al. were able to detect these products using chemical ionization mass spectrometry with  $CH_5^+$  as their protonating agent;  $M+H^+$  ions were obtained. Hydrated protons are weaker protonating agents; toluene, o-cresol, and, most likely, phenol form charge transfer ions ( $M^+$ ) and display much lower sensitivity than

TABLE VI.1. Observations of peak areas for toluene photooxidation products identified by the Shepson, Bandow, and O'Brien groups. The m/z 89 product has not been reported before.

Molecular Formula	(M <sup>+</sup> or MH <sup>+</sup> )	m/z	Reference	Observation
Methyl glyoxal	C <sub>3</sub> H <sub>5</sub> O <sub>2</sub> <sup>+</sup>	73.0290	14,15,23	no peak
2-methyl furan	C <sub>5</sub> H <sub>7</sub> O <sup>+</sup>	83.0497	14	peak growth 83.0427 ± 0.0126
Butenedial	C <sub>4</sub> H <sub>5</sub> O <sub>2</sub> <sup>+</sup>	85.0290	14,23	peak growth 85.0239 ± 0.0072
3,4-dioxo-1-butene			14	
Hydroxy-3-oxobutene	C <sub>4</sub> H <sub>7</sub> O <sub>2</sub> <sup>+</sup>	87.0446	23	peak growth 87.0424 ± 0.0048
?	C <sub>4</sub> H <sub>9</sub> O <sub>2</sub> <sup>+</sup>	89.0603	-	peak growth 89.0622 ± 0.0048
Phenol	C <sub>6</sub> H <sub>6</sub> O <sup>+</sup>	94.0419	23	no peak
Furfural	C <sub>5</sub> H <sub>5</sub> O <sub>2</sub> <sup>+</sup>	97.0290	14	peak growth 97.0286 ± 0.0022
?			14	
5-oxo-1,3-hexadiene	C <sub>6</sub> H <sub>9</sub> O <sup>+</sup>	97.0653	23	peak growth 97.0564 ± 0.0108
maleic anhydride	C <sub>4</sub> H <sub>3</sub> O <sub>3</sub> <sup>+</sup>	99.0082	15	peak growth 99.0080 ± 0.0022
4-oxo-2-pentenal	C <sub>5</sub> H <sub>7</sub> O <sub>2</sub> <sup>+</sup>	99.0446	23	contaminant 99.0447 ± 0.0015
3,4-dioxo-1-pentene			14	
Hydroxybutenedial	C <sub>4</sub> H <sub>5</sub> O <sub>3</sub> <sup>+</sup>	101.0239	23	weak growth 101.0217 ± 0.0040
Hydroxy-3-oxobutanal	C <sub>4</sub> H <sub>7</sub> O <sub>3</sub> <sup>+</sup>	103.0395	23	peak growth 103.0401 ± 0.0015
Benzaldehyde	C <sub>7</sub> H <sub>7</sub> O <sup>+</sup>	107.0497	14,15,23	contaminant calib. standard
Cresol	C <sub>7</sub> H <sub>8</sub> O <sup>+</sup>	108.0575	14,15,23	no peak

readily protonated species. Aromatic compounds not containing an aldehyde or nitro group have not been detected at the concentrations generated from toluene during irradiation in the API mode using water as the chemical reagent. This is fortunate for kinetic studies; otherwise the ion signal from toluene would consume the primary reagent ions and ion signals from photooxidation products would not be observable before the bulk of the toluene was oxidized.

Methyl glyoxal has been found in experiments in which the reaction vessel was rinsed with solvent to collect reaction products (13,14,23, 60) and has also been observed in situ using optical spectroscopy (15,20,21). Both types of experiments strongly sample any compounds adsorbed on the reaction vessel surface. Despite reported methyl glyoxal yields of ~15% (13,15,20,21), methyl glyoxal was not detected in this experiment or in a preliminary experiment in which a D<sub>3</sub>-toluene-NO<sub>x</sub>-zero air mixture with the same concentrations of constituents was irradiated and the spectra recorded using baseline resolution.

In the majority of the earlier experiments (13,14,20,21,60) methylnitrite was added to the test atmosphere to greatly increase the OH radical concentration; this procedure correspondingly diminishes the importance of photolysis of methyl glyoxal. In the troposphere photolysis consumes 8 times as much methyl glyoxal as OH radical attack (22). Bandow et al. (15), however, reported a methyl glyoxal yield of 14% without using methylnitrite. Photolysis would be expected to be important in the Bandow group's experiment and a depressed yield of methyl glyoxal would be anticipated. Their result could be rationalized if most of the methyl glyoxal formed is adsorbed onto the reservoir

surfaces and if in the adsorbed state it is stabilized against photolysis.

Using our batch system the concentration of methyl glyoxal reaching the API source could be increased about 5-fold to enhance sensitivity by decreasing the dilution ratio from 1:8 to 1:1.5. In addition, a larger initial toluene concentration, short of causing saturation, would increase the gas phase concentration of methyl glyoxal and the likelihood of its detection. But ultimately, using a flow through system (54,55) to overcome the effect of adsorption on the gas phase concentrations of products would provide the greatest probability for detection of methyl glyoxal.

#### VI.3.j) Adsorption

Although acetic acid, a very polar product, provided a strong ion signal in preliminary experiments performed with baseline resolution, adsorption on the reservoir walls and flow system of polar compounds, such as those listed as toluene products by Dumdei et al. (23), may greatly reduce the amounts of polar products delivered to the instrument and render them undetectable.

Evidence for the presence of adsorbed compounds was provided when the reservoir was heated by turning off the cooling fan after several hours of irradiation in a preliminary experiment at baseline resolution. Peaks having the same nominal mass as ions expected from several of the polar compounds found by the Dumdei group grew within several minutes. This type of experiment should be repeated at medium resolution using  $H_8^-$  and deuterated toluenes to determine if the peaks that grow are due

to products rather than to contaminants.

### VI.3.k) Differentiating Classes of Photooxidation Products

Observation of variations in peak areas with changes in the CID potential permit different types of ions to be distinguished (Chapter III). During the deuterated and non-deuterated toluene experiments the CID potential should be varied and trends in the product peaks observed to determine if different classes of products behave similarly. For example, at lower CID potentials the ratio of the peak area of a monohydrate to that of the bare, protonated molecular ion ( $A_m/A_b$ ) may be greater for compounds containing an OH group. A significant monohydrate ion peak was observed for acetic acid at  $m/z$  82 in methyldeuterated toluene spectra (Figure IV.7). Monohydrate peaks may also appear for alcohols desorbed from the heated reservoir walls, but with lower  $A_m/A_b$  ratios at a given CID potential. These ratios might be smaller yet for compounds containing only carbonyl groups.

At higher CID potentials these three distinct classes of products could show different susceptibilities to fragmentation; the relative declines in peak areas as the CID potential is increased for these three classes could help assign an unknown product to one of these groups.

Knowledge of such class related differences gained in the toluene photooxidation experiments would be especially helpful when studying compounds for which deuterated analogs are not available.

## CHAPTER VII

## CONCLUSIONS

A corona discharge, atmospheric pressure ionization source for a VG 7070E-HF mass spectrometer was successfully designed, built, and characterized. The resulting API mass spectrometer provides medium resolution (4,800, 10% valley), which is necessary to separate and assign exact masses to multiple peaks at the same nominal mass arising from numerous components in a gas mixture. Sensitivity sufficient to determine molecular formulae of components in simulated atmospheres, directly, without concentration or separation steps, was demonstrated for test atmospheres containing 10 ppm of toluene.

Under optimum conditions positive ionization of trace constituents that have greater proton affinities than water in the gas phase is essentially complete. Under typical atmospheric conditions, however, ionization is incomplete and large numbers of hydrated analyte ions are also formed. The diminished signal of each component is thereby dispersed into several peaks having different  $m/z$  ratios; this complicates interpretation of mass spectra recorded for gas mixtures and further decreases sensitivity for each compound. Sensitivity for analytes is increased and formation of hydrated ions is suppressed by reducing the number density of water molecules in the API source. This is accomplished by reducing the relative humidity of the sample gas or by reducing the pressure in the corona discharge region.

Disaggregation of remaining hydrated ions that enter the differentially pumped region is induced by applying a small potential across this region. Excessive potentials, however, cause significant fragmentation of molecular analyte ions, again complicating the spectra and diminishing sensitivity. Fortunately, at least for the compounds studied, dehydration is accomplished before fragmentation becomes important.

The sensitivity for protonatable analytes is determined by both the availability of hydrated protons small enough to protonate the analytes and by the number density of analyte molecules in the sample stream. Hence, the dilution ratio at which maximum sensitivity occurs for a given test atmosphere depends on the concentration of protonatable molecules in the reservoir. In practice the number density of water molecules is adjusted to maximize sensitivity, then the CID potential is varied to distinguish between hydrated, fragmented, and molecular ions.

Sensitivity for toluene, ionized by charge transfer rather than by protonation, is > 200 times lower than for benzaldehyde and, presumably, for other photooxidation products. This permits photooxidation products to be detected before a large fraction of the toluene is consumed. Photooxidation of toluene is initiated by OH radical attack in the troposphere or in a reaction vessel. Because OH radicals are formed during the sequences of ion-molecule reactions that produce hydrated protons in the source, spurious products are formed in the API source, which interfere with determination of the products formed in the reaction vessel. This interference must be substantially



reduced before quantitative observations of product yields as a function of irradiation time can be made.

Three strategies suppress this interference: 1) using the smallest sustainable corona discharge current; 2) adding CO to the sample gas to scavenge OH radicals in the source; and 3) modestly increasing the flow rate through the corona region. The increased flow was only moderately effective in suppressing spurious product formation in the source but enhanced substantially the signal-to-noise ratio.

A dynamic range of two decades was demonstrated; both major and minor products should be observable simultaneously in photooxidation studies of various organic compounds. The detection limit for benzaldehyde under optimal source conditions was 8 ppb in the reservoir. Assuming other compounds containing the carbonyl or hydroxyl groups have similar detection limits, most photooxidation products of toluene should be detectable using an initial toluene concentration of 10 ppm in the reservoir.

Evidence confirming the production in the reaction vessel of several toluene photooxidation products observed in past studies was provided by the medium resolution capability of the API mass spectrometer. Multiple peaks were resolved at most nominal masses; exact masses assigned to several separated peaks corresponded precisely to the molecular formulae of the products found previously.

Molecular formulae alone seldom identify a compound, but use of deuterated analogs of organic compounds could permit structural information to be obtained for products without resort to tandem mass spectrometry in future experiments. Use of deuterated compounds could

also distinguish between products and contaminants; the  $m/z$  ratio of peaks due to products formed from completely deuterated organic reactants would change, while contaminant related  $m/z$  ratios would not.

After performing deuterated toluene studies, the instrument could be used to identify photooxidation products of other organic compounds for which incomplete carbon balances have been observed. These experiments could be performed with the batch system currently in place by heating the flask after several hours of irradiation to desorb products adhering to the reaction vessel walls. Later kinetic experiments, in which the production and consumption of products could be followed with irradiation time, would require construction and testing of a flow through system.

The additional knowledge about the removal mechanisms of these compounds provided by product identification and reaction rates determined from kinetic studies would permit better atmospheric models to be formulated.

## APPENDIX A

## DISCHARGE SUPPRESSION SYSTEM

The following describes the design and operation of the discharge suppression system that was built to prevent arcing to the grounded pump when the API source is operated at its full accelerating potential. This section has been accepted for publication by Review of Scientific Instruments as an Application Note.

Atmospheric pressure ionization (API) mass spectrometry is used to study trace constituents in air without sample concentration or separation prior to analysis (25). Before we constructed our source, API mass spectrometry had generally been limited to quadrupole instruments that, at best, provide only unit resolution (24,25,61). High performance, magnetic sector mass spectrometers operate with source potentials in the kilovolt range where arcing between an API source and grounded surfaces along connecting gas lines can disrupt operation, damage electronic components, and expose human operators to the hazards of a high voltage shock.

The specific problems associated with electrical discharges through gas lines connected to a chemical ionization (CI) source in a high resolution mass spectrometer are known (62); they relate in all but one respect to the circumstances associated with using an API source in such an instrument, the exception being that the throughput of gas in the main pumping line of an API source is about 1,000 times greater than

that in the sample introduction line of a CI source. We have devised an electrical discharge suppression system for a medium throughput (~2 L/s) pumping line that overcomes this problem. Our discharge suppression system has permitted us to operate a VG 7070E-HF mass spectrometer in an API mode at a resolution of 4,800 (10% valley) at  $m/z$  92 (Chapter II); this capability has, for example, already allowed us to assign molecular formulae to at least two, previously unresolvable photooxidation products of toluene generated in an irradiated smog chamber (Chapter VI).

Figure A.1 is a schematic diagram of a corona discharge API source. The corona region, where ions are formed, is normally at atmospheric pressure, and the differentially pumped region, the so-called collisionally induced dissociation (CID) region, separating the corona region from the mass analyzer is maintained at -1 Torr. Therefore, during operation, the pressure within the pumping line falls from -1 Torr in the CID region to -0.05 Torr at the head of the pump. As in the case of CI, the conditions along such a gas line are ideal for glow discharges, particularly in the pressure range 0.1-0.3 Torr (62).

The conditions under which gases in the pressure range of  $10^{-2}$  to 1 Torr conduct electricity have been characterized (63-65). Such discharges are avalanche phenomena; their initiation occurs in accordance with Paschen's law, which states that the breakdown potential,  $V_B$ , of a gas between two electrodes is a function of the product of the gas pressure and the electrode separation (64). Accordingly, for a given pressure and voltage,  $V$ , glow discharges can be suppressed by maintaining enough separation between the conducting

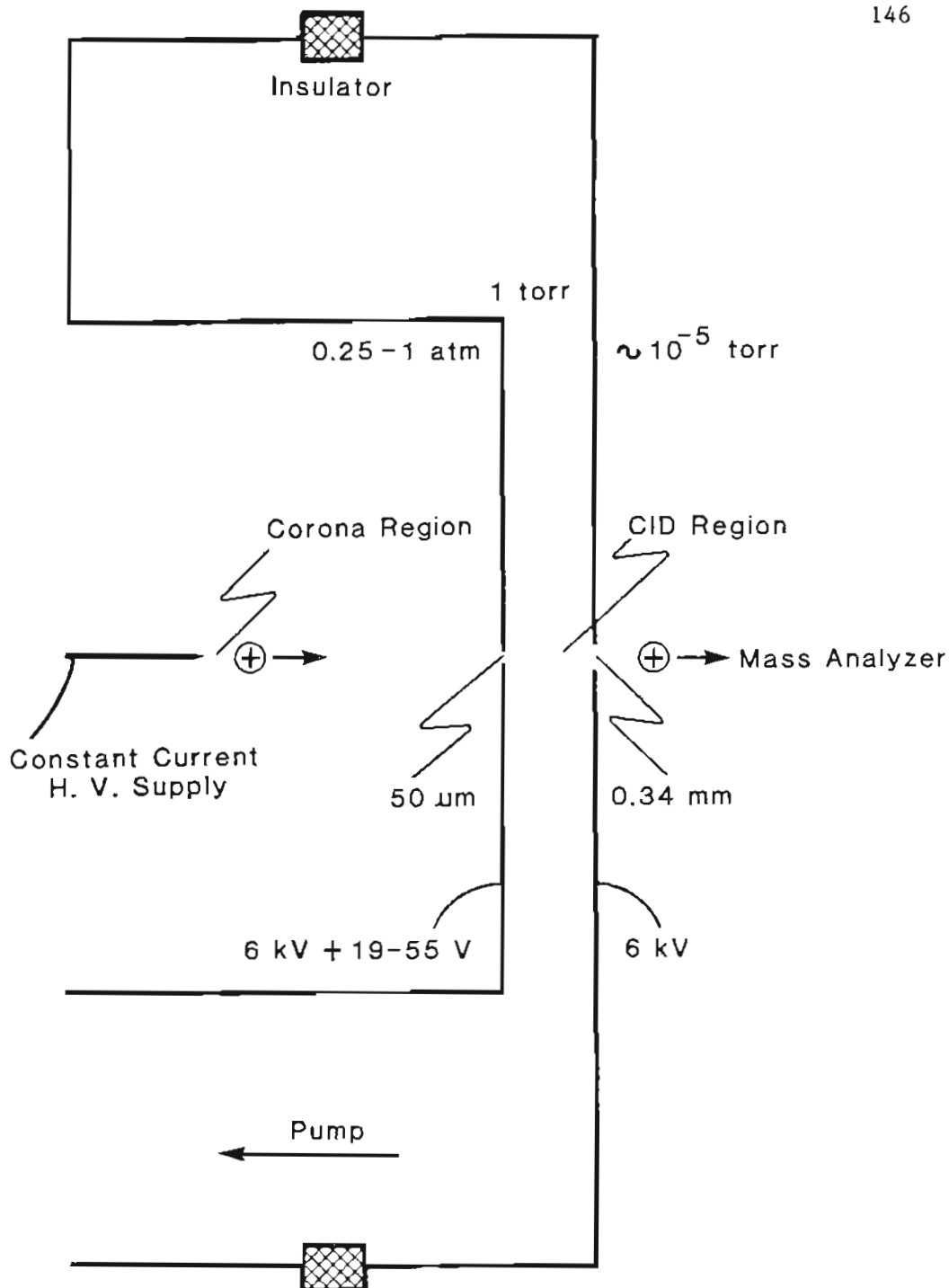


Figure A.1. Simplified drawing of the API source illustrating the locations of the corona and collisionally induced dissociation (CID) regions and of the apertures between those regions and the mass analyzer. Typical pressures within each region and typical potentials applied to the aperture electrodes are also indicated.

elements in the gas volume to ensure that  $V_B > V$ . In practice, discrete insulating or resistive elements have been used to spread the drop in voltage over a series of stages that alternate with field free regions where charge neutralization can occur (62,65).

Initially, we based the design of our discharge suppression system solely on the proven concept of controlling the voltage gradient. However, with a voltage gradient device alone we still observed sporadic arcing at 6 kV when the pressure in any region of the assembly was near 0.1 Torr. To eliminate this arcing, we altered our design 1) to increase the gas pressure in the voltage gradient region and thereby, in accordance with Paschen's law, raise  $V_B$  and 2) to localize the pressure gradient in a region where the voltage is at ground potential and there is no electric field to initiate and sustain a discharge. A schematic of our final design is shown in Figure A.2 along with a graphic depiction of the system's operating principle.

Physically, the system consists of 16 ft of 3 in. i.d. PVC tubing, which is folded back on itself by means of a U-bend in the middle, with a total of 94 circular, stainless steel screens (60 mesh, 73% transparent) uniformly distributed (1 1/2 in. apart) along the two, straight sections of pipe. The screen-discs are electrically separated by a 1 M $\Omega$  resistance that actually consists of three, parallel 3 M $\Omega$  resistors spaced evenly around the circumference of a 1 5/8 in. diameter circle (11/16 in. from the inner surface of the PVC tubing); three resistors are used instead of one to give the assembly mechanical rigidity. The resistor-screen stages force the voltage gradient along the length of the pumping line to be uniform (~64 V per 1 1/2 in. stage

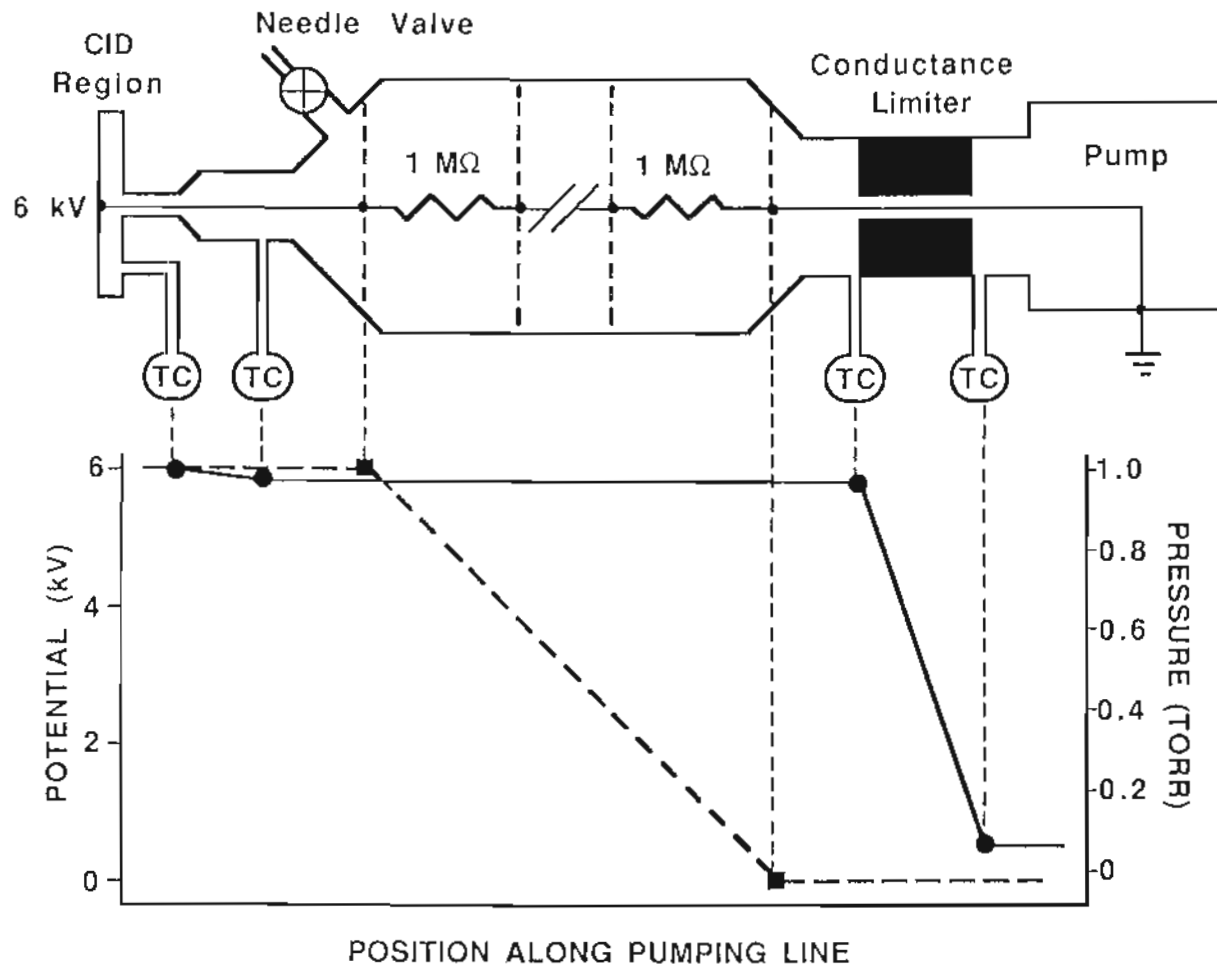


Figure A.2. Schematic diagram of the discharge suppression system. The plots illustrate how the system separates the potential (dashed) and pressure (solid) gradients along the pumping line to achieve discharge suppression.

at 6 kV). The pressure along the voltage gradient is maintained nearly constant at 1 Torr by bleeding air through a needle valve located in the pumping line at a point between where it exits the mass spectrometer and where the resistor-screen assembly begins and by placing a conductance limiting tube, 0.2 in. i.d. and 1.5 in. long, in the line just before it reaches the rotary pump. The pressure gradient is primarily limited to the flow limiter. The large diameter pipe and the highly transparent screens in the voltage gradient region constitute a high conductance line; hence, the conductance of the entire system is essentially equal to that of the flow limiter, namely  $\sim 2$  L/s (66).

Using an Al plug in place of the connection to the API source and a gas pressure of 1 Torr at the plug end, we tested our discharge suppression system up to  $\pm 15$  kV. With the plug at either +15 kV or -15 kV, sporadic arcing was observed for periods of up to 45 sec after turning on the high voltage supply, but thereafter, no electrical breakdown was detected. Therefore, our system could be employed with double focusing mass spectrometers using accelerating voltages at least as high as 10 kV.

We believe our present, prototype discharge suppression device is built very conservatively and that a more compact system containing fewer stages in a shorter, smaller diameter pipe would be just as effective. Such a device might allow higher accelerating voltages to be used with other types of ion sources currently limited by arcing at pressures  $> 0.1$  Torr (67).



## APPENDIX B

## DILUTION CORRECTION CALCULATION

Dilution by the carrier gas (dry zero air) lowers both the relative humidity of the reservoir gas and the concentrations of reactants and products in the flask. To calculate this dilution as a function of time, an exponential dilution equation is derived in the following text.

Assume that for limited flows ( $\sim 2-20 \text{ cm}^3 \text{ min}^{-1}$ ) over a short time span (1 min) gas having the average concentration of components in the flask is driven toward the API source. This assumption is not unreasonable since the ends of the inlet and output lines are well separated (Figure III.1). Then the average concentration of flask components after one minute is:

$$[x]_1 = [x]_0 \times (12,000 / (12,000 + FT)) \quad (12)$$

where  $[x]_1$  is the average concentration of any component in the flask gas after 1 minute of flow;  $[x]_0$  is the initial concentration of  $x$  before the flow began;  $F$  is the flow in  $\text{cm}^3 \text{ min}^{-1}$ ;  $T$  is the flow duration, 1 minute; and 12,000 is the flask volume in  $\text{cm}^3$ .

After additional minutes of flow,  $[x]_2$ ,  $[x]_3$ , ...  $[x]_n$  are similarly given by:

$$[x]_2 = [x]_1 \times (12,000/(12,000 + FT)) \quad (13)$$

$$[x]_3 = [x]_2 \times (12,000/(12,000 + FT)) \quad (14)$$

⋮

$$[x]_n = [x]_{n-1} \times (12,000/(12,000 + FT)) \quad (15)$$

Substituting for  $[x]_1$  in equation 13 from equation 12:

$$[x]_2 = [x]_0 \times (12,000/(12,000 + FT))^2 \quad (16)$$

Similarly, the right side of equation 16 can be substituted into equation 14 for  $[x]_2$  and the exponent will again be incremented.

Hence, continuing these substitutions for any number of minutes,  $t$ :

$$[x]_t = [x]_0 \times (12,000/(12,000 + FT))^t \quad (17)$$

Dividing the numerator and denominator of the fraction by 12,000 simplifies this expression:

$$[x]_t = [x]_0 \times (1/(1 + FT/12,000))^t \quad (18)$$

This equation was used to make all dilution corrections.

## APPENDIX C

COMMENTS ON THE VOLUME OF AND REACTIONS WITHIN THE  
OH ENRICHED REGION

## C.1. Before Addition of Scavenger Gas

$N_2^+$  and  $O_2^+$  ions are formed within 0.005 cm (68) of the tip, which has a hemispherical appearance when magnified. The volume adjacent to the tip where these ions are formed ( $V$ ) may be approximated by the volume between two hemispheres equal to  $2/3 \times \pi \times (r_2^3 - r_1^3)$  where,  $r_1$  is the needle tip radius (0.009 cm) and  $r_2 = r_1 + 0.005$  cm. Hence,  $V = 4.2 \times 10^{-6} \text{ cm}^3$ .

OH radicals are then formed by consecutive reactions within and outside this volume. Using the integrated rate equation from Laidler (69) appropriate to reaction 1, the time required for 90% of the  $N_2^+$  ions to react to form  $N_4^+$  ions is calculable.

$$t = \{1/(2b_o + a_o) \times (1/a - 1/a_o) + 1/(2b_o - a_o)^2 \times \ln(b_o a/a_o b)\}/k \quad (19)$$

where  $a_o = [N_2]_o = 0.8 \times 2.46E19 \text{ molecules/cm}^3$ ;  $a = a_o$ ;  $b_o = [N_2^+]_o$ ; and  $b = 0.1 \times b_o$ . The ion formation rate is  $i_c/e$  where  $i_c$  is the corona current and  $e$  is the charge of an electron. Using the ion drift velocity,  $2 \times 10^4 \text{ cm sec}^{-1}$ , estimated from reference 70 across our tip-to-orifice distance for a corona voltage of 2.5 kV,  $2.5 \times 10^{-7} \text{ sec}$  is the time necessary for an  $N_4^+$  ion to travel 0.005 cm. The number of ions formed during this time divided by the ion formation volume

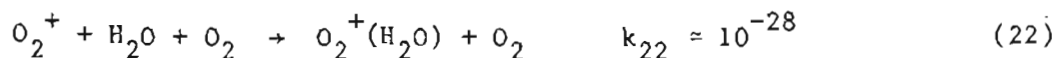
provides an estimate of the average ion concentration within this region:  $b_o = [N_2^+] = (2.5E-7 \text{ sec} \times 0.2E-6 \text{ coul/sec}) / (1.6E-19 \text{ coul/ion} \times 4.2E-6 \text{ cm}^3) = 7.4 \times 10^{10} \text{ ions/cm}^3$ . Using equation 19,  $t$  is calculated to be  $7 \times 10^{-11} \text{ sec}$  for 90% conversion of  $N_2^+$  to  $N_4^+$ . Hence, this process may be regarded as instantaneous.

The appropriate integrated rate equation for reaction 2 from Laidler (69) is:

$$t = \{1/(b_o - a_o) \times \ln(a_o(b_o - x)/b_o(a_o - x))\}/k \quad (20)$$

where  $a_o = [N_4^+]_o \approx 7.4E10 \text{ ions/cm}^3$ ;  $b_o = [H_2O]_o = 4.2E16 \text{ molecules/cm}^3$ ; and  $x$  is the amount of species  $a$  reacted  $= 0.9 \times a_o$ . Solving for  $t$ ,  $t = 3 \times 10^{-8} \text{ sec}$ . Most of the OH is formed through two  $O_2^+$  pathways after  $N_4^+$  clusters transfer charge to  $O_2$  molecules. Since the concentration of  $O_2$  is over  $10^2$  times greater than that of  $H_2O$ , this reaction should occur much faster than reaction 2, on the order of  $10^{-10} \text{ sec}$ . Compared to the following reactions, this process is also instantaneous.

$O_2^+$  also forms a cluster ion or reacts with a water molecule (34):



Using equation 19 and assuming all positive ions were  $O_2^+$  ions,  $4 \times 10^{-8} \text{ sec}$  would be required to convert 90% of the  $O_2^+$  ions to  $O_4^+$  clusters via reaction 21. If  $N_2$  could serve as the third body in this reaction, less time would be required. The rate of reaction 22 is 0.3-3.2 times that of reaction 21 over a range of relative humidity of 6-58%.

$O_4^+$  clusters also react with water to form the  $O_2^+(H_2O)$  ion (34):



Using equation 20, the time required for 90% of the  $O_4^+$  to react, assuming all positive ions are  $O_4^+$  cluster ions, would be  $4 \times 10^{-8}$  sec.

Once  $O_2^+(H_2O)$  is available the predominant reactions are with water to produce larger hydrated  $O_2^+$  ions. At each stage of hydration, some react to produce an OH radical and a hydrated proton - but even simple calculations of the type used so far are not possible. Because the direct formation of  $O_2^+(H_2O)$  from  $O_2^+$  and  $H_2O$  without the intervening  $O_4^+$  cluster formation is also important, and because reactions 21 and 22 do not await the completion of each preceding reaction to begin, summing the times calculated above suggests  $O_2^+(H_2O)$  formation should be essentially complete after  $< 10^{-7}$  sec. Assuming all of the OH radicals have been formed after  $10^{-6}$  sec, a very crude estimate of the volume in which the OH radicals are formed can be made. After  $10^{-6}$  sec the ions have traveled -0.02 cm away from the needle tip; hence, all OH radicals should be formed within 0.025 cm of the tip. The volume adjacent to the tip bounded by two hemispheres of radii 0.009 cm, the tip radius, and 0.034 cm, the tip radius plus the limit of ion travel before all of the OH radicals are formed, is  $2/3 \times \pi \times (0.034^3 - 0.009^3) = 8.1 \times 10^{-5} \text{ cm}^3$ .

Hydrated protons react according to reactions 4-6 while continuing to travel rapidly toward the surrounding walls. The OH radicals, however, are not accelerated by the electric field. The average steady state concentration of OH radicals within this volume will also depend upon chemical, flow, and diffusion processes; the source term must be

balanced by loss terms.

For any volume element, a mass balance can be described:

$$0 = \text{source or flow in of OH} + \text{regeneration of OH} - \text{consumption of OH} \\ - \text{flow out of OH} - \text{diffusion out of OH} \quad (24)$$

Diffusion determines whether there is a very small OH enriched volume, a completely homogeneous distribution of neutral species within the corona region volume established after numerous wall collisions, or some intermediate situation. The simple treatment above establishes an upper limit for the volume in which OH radicals are formed and ignores the inhomogeneous distribution of species produced by consecutive reactions, illustrated in Figure IV.4. This limiting volume can be used, however, to model the small OH enriched volume extreme.

The OH source term for this volume is approximately equal to the corona current divided by the charge of an electron and by the formation volume ( $i_c/eV$ ).

The consumption term has several components arising from the chemical reactions listed in Table C.1. Reactions with toluene, NO, NO<sub>2</sub>, and H<sub>2</sub>O<sub>2</sub> (formed in reaction T1) are first order, while the OH self-consumption reactions are second order in [OH]. Products from toluene-OH reactions in the source also compete for OH radicals to an extent dependent upon their yields, rate constants, and mode of ionization.

The NO added to the reservoir reacts with O<sub>2</sub> to form NO<sub>2</sub>, which is necessary to generate OH radicals in the reaction vessel when it is irradiated (9):

TABLE C.1. Rate constants for OH attack of various compounds at a temperature of 298°K, a temperature not much different from that in the corona region when using a 0.2  $\mu$ A corona current. The concentration of third bodies, [M], is that at atmospheric pressure and is included in the second order rate constants. The factors are the ratio of each competing OH reaction rate constant to that of toluene.

	<u>Reaction</u>	<u>k(298°K)</u>	<u>Factor(298°K)</u>	<u>Reference</u>
T1)	$2\text{OH} + \text{M} \rightarrow \text{H}_2\text{O}_2 + \text{M}$	$3.9 \times 10^{-12}$	f(V)	71
T2)	$2\text{OH} \rightarrow \text{H}_2\text{O} + \text{O}$	$1.9 \times 10^{-12}$	f(V)	71
T3)	$\text{OH} + \text{H}_2\text{O}_2 \rightarrow \text{H}_2\text{O} + \text{HO}_2$	$1.7 \times 10^{-12}$	0.27	71
T4)	$\text{OH} + \text{HO}_2 \rightarrow \text{H}_2\text{O} + \text{O}_2$	$1.1 \times 10^{-10}$	17	71
T5)	$\text{OH} + \text{NO} + \text{M} \rightarrow \text{HONO} + \text{M}$	$4.8 \times 10^{-12}$	0.75	71
T6)	$\text{OH} + \text{tol} \rightarrow \text{products}$	$6.4 \times 10^{-12}$	1.0	5
T7)	$\text{OH} + \text{NO}_2 + \text{M} \rightarrow \text{HNO}_3 + \text{M}$	$1.1 \times 10^{-11}$	1.7	71
T8)	$\text{OH} + \text{C}_6\text{H}_5\text{CHO} \rightarrow \text{products}$	$1.3 \times 10^{-11}$	2.0	6
T9)	$\text{OH} + \text{o-cresol} \rightarrow \text{products}$	$4.7 \times 10^{-11}$	7.3	6
T10)	$\text{CO} + \text{OH} \rightarrow \text{CO}_2 + \text{H}$	$2.4 \times 10^{-13}$	0.038	71



Using a rate constant of  $1.9 \times 10^{-38} \text{ cm}^6 \text{ molecule}^{-2} \text{ sec}^{-2}$  (6) and integrated rate equation 20, 90% of the NO was converted to  $\text{NO}_2$  before gas from the reaction vessel was sampled and the spectrum in Figure IV.1.1.b recorded.

The regeneration term arises from the  $\text{HO}_2$  produced in reaction T3. The  $\text{HO}_2$  produced in reaction T3 can react with NO to regenerate OH or with OH or  $\text{NO}_2$  to produce stable products (71):



$\text{HO}_2$  reacts much slower (10) with toluene than does OH and does not generate significant amounts of spurious products.

The flow out of OH in radicals/sec is  $[\text{OH}]_{\text{ss}}V/t_r$  where  $[\text{OH}]_{\text{ss}}$  is the average steady state concentration of OH radicals in V, the OH enriched volume, and  $t_r$  is the residence time within this volume. A rough estimate of this time is made by dividing the flow through the API source by the cross sectional area of the corona region to obtain a linear velocity along the tip to orifice axis. The width of the enriched region divided by this velocity is used to estimate the residence time.

The diffusion term depends on the concentration gradient across the volume's outer boundary, which is unknown. Hence, a simplified equation ignoring diffusion, inhomogeneities in concentrations within the OH



enriched volume, OH attack on spurious products, and wall losses for the complete diffusion extreme, but useful to establish the relative importance of self-consumption reactions and to determine if significant consumption of OH by toluene occurs, was derived:

$$[\text{OH}]_{\text{ss}} = (i_{\text{c}}/eV + k_{26}[\text{HO}_2]_{\text{ss}}[\text{NO}]_{\text{ss}}) / (k_{\text{T6}}[\text{tol}]_{\text{ss}} + k_{\text{T5}}[\text{NO}]_{\text{ss}} + k_{\text{T7}}[\text{NO}_2]_{\text{ss}} + k_{\text{T3}}[\text{H}_2\text{O}_2]_{\text{ss}} + (k_{\text{T1}} + k_{\text{T2}})[\text{OH}]_{\text{ss}} + 1/t_{\text{r}}) \quad (29)$$

Equations for each of the steady state concentrations in this equation must be derived from the steady state rate equations for reactions that produce or consume each species before  $[\text{OH}]_{\text{ss}}$  can be estimated. For toluene, NO, or  $\text{NO}_2$ :

$$[\text{x}]_{\text{ss}} = [\text{x}]_{\text{o}} / (1 + k_{\text{x}}[\text{OH}]_{\text{ss}}t_{\text{r}}) \quad (30)$$

where  $[\text{x}]_{\text{o}}$  is the bulk flow of x entering the API source,  $k_{\text{x}}$  is the reaction rate constant for OH attack, and  $t_{\text{r}}$  is the residence time. Diffusion of x into the enriched volume has been ignored. The corresponding expression for  $[\text{H}_2\text{O}_2]_{\text{ss}}$  formed by reaction T1 and consumed by reaction T3 is:

$$[\text{H}_2\text{O}_2]_{\text{ss}} = k_{\text{T1}}[\text{OH}]_{\text{ss}}^2 / (1/t_{\text{r}} + k_{\text{T3}}[\text{OH}]_{\text{ss}}) \quad (31)$$

Algebraic manipulation of the steady state rate equations for reactions 26-28 and T3 yields the following equation for  $[\text{HO}_2]_{\text{ss}}$ :

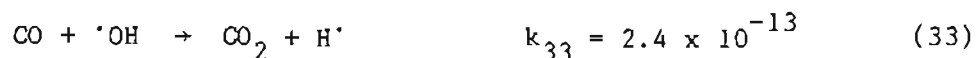
$$[\text{HO}_2]_{\text{ss}} = k_{\text{T3}}[\text{OH}]_{\text{ss}}[\text{H}_2\text{O}_2]_{\text{ss}} / (k_{26}[\text{NO}]_{\text{ss}} + k_{27}[\text{OH}]_{\text{ss}} + k_{28}[\text{NO}_2]_{\text{ss}} + 1/t_{\text{r}}) \quad (32)$$

After first substituting the expressions for the steady state concentrations of  $\text{H}_2\text{O}_2$ ,  $\text{NO}$ , and  $\text{NO}_2$  into equation 32, the expressions for  $[\text{tol}]_{\text{ss}}$ ,  $[\text{NO}]_{\text{ss}}$ ,  $[\text{NO}_2]_{\text{ss}}$ ,  $[\text{H}_2\text{O}_2]_{\text{ss}}$ , and  $[\text{HO}_2]_{\text{ss}}$  are substituted into equation 29 to provide an equation with  $[\text{OH}]_{\text{ss}}$  as the only unknown. Iterative calculation provides an average value for  $[\text{OH}]_{\text{ss}}$  within the OH enriched region.

Assuming no diffusion and complete diffusion of all neutral species, the calculated average  $[\text{OH}]_{\text{ss}}$  values are  $4.0 \times 10^{13}$  and  $5.3 \times 10^9$  radicals/cm<sup>3</sup> respectively. Table C.2 lists the calculated percentages of OH radicals consumed by the consumption terms in equation 29. Since the flow out terms account for < 4% of the OH loss from the very small volume and for 0.14% loss out of the API source assuming complete diffusion, nearly all of the OH radicals are consumed within the corona region.

### C.2. After Addition of CO

The regeneration term included in equation 29 must be modified when CO is added to the sample stream since one of the products of OH attack on CO is H:



H quickly reacts with the 20%  $\text{O}_2$  present in the reaction volume to form  $\text{HO}_2$  (71):



This additional source of  $\text{HO}_2$  will increase the importance of the OH regeneration term and an additional term must be added to the numerator

TABLE C.2. Percentages of OH radicals consumed by self-consumption (reactions T1-T4), by toluene (reaction T6), by NO (reaction T5), by NO<sub>2</sub> (reaction T7), by flow of OH out of the enriched volume, and by CO (reaction T10) computed using the model in Appendix C. Percentages are listed with and without addition of 0.8% CO assuming no diffusion and complete diffusion, i.e. diffusion sufficient to yield homogeneous distributions of components within the corona region.

% OH consumed by:	Self-consumption	Toluene	NO	NO <sub>2</sub>	Flow out	CO
no diffusion:	92	2.0	0.20	1.8	3.5	0
no CO						
diffusion:	0.009	39	3.0	58	0.14	0
no diffusion:	0.005	0.27	0.02	0.38	0.03	99
0.8% CO						
diffusion:	8E-7	0.32	0.02	0.49	0.001	99

in equation 32:  $k_{34}[H]_{ss}[O_2]_o$ . The high concentration of  $O_2$  entering the source,  $[O_2]_o$ , has been substituted for  $[O_2]_{ss}$  in this term.  $[H]_{ss}$  is given by:

$$[H]_{ss} = k_{t10}[CO]_{ss}[OH]_{ss}/(k_{34}[O_2]_o + 1/\tau_r) \quad (35)$$

The modified regeneration term was used in equation 29 and an OH consumption term due to the added CO,  $k_{T10}[CO]_{ss}$ , was included in the denominator. The regeneration term increased from < 0.2% of the OH source term for both diffusion extremes before addition of CO to 22% and 60% without and with diffusion respectively after CO addition.

Table C.2 also lists calculated percentages of OH radicals lost to the consumption terms in equation 29 after addition of CO, without diffusion and with complete diffusion. OH self-consumption reactions are only important for the very small volume in the absence of CO. The large concentration of CO ensures that most of the OH is consumed by CO and that only a small decrease in the bulk CO concentration within the OH enriched region can occur, regardless of its dimensions. Addition of 0.8% CO lowered  $[OH]_{ss}$  100- and 80-fold for the no diffusion and complete diffusion cases respectively, and over 99% of the OH consumption was due to CO for both extremes of diffusion. This explains the suppression of spurious product formation observed.

Without diffusion and added CO,  $[tol]_{ss}$  falls to 5% of its bulk concentration within the OH enriched volume. If the toluene signal is generated after toluene molecules cross the OH enriched region, an observable reduction in its intensity should occur due to OH-toluene reactions. For complete diffusion, 39% consumption of OH radicals by

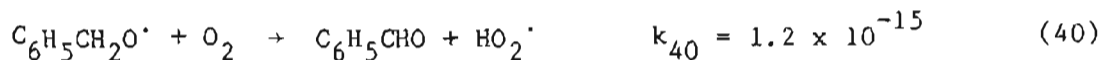
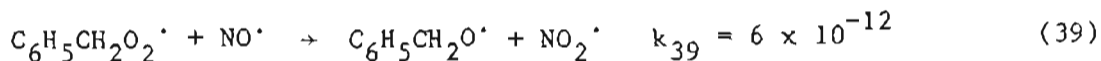
toluene would decrease the toluene concentration in the source by only 6%. Correcting the toluene signal in Figure IV.5.a (no CO added) relative to that in Figure IV.5.b (0.8% CO added) for differences in toluene dilution and total ion current indicated no observable decline in the toluene signal due to its consumption by OH chemistry. With 1.1 ppm of toluene entering the API source and with a 0.2  $\mu\text{A}$  corona current, this observation suggests that either diffusion is important or that most of the toluene undergoing charge transfer flows into the region of high precursor ion concentration without traversing the OH enriched region, i.e. by flowing along the needle toward the tip (from left to right in Figure IV.4). The decrease in the relative ion abundance for the toluene molecular ion in Figure IV.2 up to a corona current of 1  $\mu\text{A}$ , however, indicates the toluene signal is diminished by the presence of OH radicals; toluene cannot be reaching the corona tip without exposure to OH radicals. Therefore, diffusion must be important.

### C.3. After Enhancement of the Flow

For any primary spurious product, x, in the OH enriched region:

$$0 = \text{Production of } x - \text{Consumption of } x - \text{Flow out of } x \\ - \text{Diffusion out of } x \quad (36)$$

Choosing benzaldehyde as a specific example, the reaction sequence responsible for benzaldehyde production is (5,6):



Noting that reactions 38 and 40 occur very rapidly due to the high concentration of  $\text{O}_2$ , the following equation for the average steady state concentration of benzaldehyde in the OH enriched region was derived:

$$[\text{benz}]_{\text{ss}} = k_{39}k_{37}[\text{NO}]_{\text{ss}}[\text{tol}]_{\text{ss}}[\text{OH}]_{\text{ss}} / \{ (k_{39}[\text{NO}]_{\text{ss}} + 1/t_r) \times (\sum k_{\text{ion},n}[\text{H}(\text{H}_2\text{O})^+]_{\text{ss}} + k_{\text{T8}}[\text{OH}]_{\text{ss}} + 1/t_r) \} \quad (41)$$

Comparing this equation to previous equations, an additional consumption term appears in the denominator that arises from protonation of benzaldehyde within this region; only spurious products that are readily protonated will appear in the spectra. This summation term recognizes that the concentrations of protons associated with different numbers of water molecules and the rate constants for ionization of benzaldehyde by these hydrated protons can be different; the last two terms in the denominator correspond to consumption of benzaldehyde by OH radicals and flow of benzaldehyde out of the OH enriched region.

Table C.3 displays for both the low and high flows the calculated percentages of benzaldehyde lost by ionization and by OH attack within this small volume and by flow out of this volume assuming that no diffusion and complete diffusion of neutral species occurs. Also indicated are the average steady state concentrations of benzaldehyde within this volume.

TABLE C.3. Percentages of benzaldehyde consumed by ionization, by OH radical attack, and lost by flow from the OH enriched region for the normal and enhanced flow conditions assuming no diffusion and complete diffusion. The table entries were calculated using equation 29 to estimate  $[OH]_{SS}$  and equation 41 to determine  $[benz]_{SS}$ .  $1.8 \times 10^{-9} \text{ cm}^3 \text{ molecule}^{-1} \text{ sec}^{-1}$ , taken from reaction 3, was arbitrarily used for an average  $k_{ion}$ , while all of the ions in this region were assumed to be capable of protonating benzaldehyde.

Percentage consumed by:	Ionization	OH Radicals	Flow out	$[benz]_{SS}$	
No diffusion	Low flow:	6.2	91	2.4	$2.4 \times 10^9$
	High flow:	5.8	85	9.2	$6.6 \times 10^9$
Complete diffusion	Low flow:	13	10	77	$8.3 \times 10^{10}$
	High flow:	3.9	3.1	93	$2.4 \times 10^{10}$

For the no diffusion extreme, the benzaldehyde signal would be greater at the higher flow due primarily to the four times greater flow of toluene into the volume. Assuming the benzaldehyde which flows out of the OH formation volume is later ionized, the ratio of (high flow signal) / (low flow signal) for benzaldehyde would be 4.8,  $(6.6E9 \times (0.058 + 0.092)) / (2.4E9 \times (0.062 + 0.024))$ . Since the  $m/z$  107 signal decreased when the flow was increased to 34% of its initial value, the no diffusion case clearly does not apply.

For the complete diffusion extreme the flow out term refers to the corona region. The ratio of (high flow signal) / (low flow signal) for benzaldehyde would be 0.09,  $(2.4E10 \times 0.039) / (8.3E10 \times 0.13)$ . The complete diffusion extreme errs in the opposite direction, predicting too great a reduction in the benzaldehyde signal. Hence, diffusion is important and  $[OH]_{ss}$  decreases moving away from the tip. Therefore, an OH enriched region does exist.

An excellent technique for directly probing the dimensions and effective temperature of the OH enriched region would be laser induced fluorescence from OH radicals. The spacial resolution of this technique should be adequate to determine  $[OH]_{ss}$  near the corona tip. A bench top corona discharge mounted in glass tubing would provide optical access to the corona region. Such experiments should be performed in the future.

Differences in  $k_{37}$ ,  $k_{39}$ ,  $k_{10n}$ ,  $k_{T8}$ , and diffusion coefficients between benzaldehyde and other spurious products which might follow this same production sequence can cause major changes in the signal reduction expected. Hence, this simple model accounts for the observation that different spurious products display different signal reductions when the



flow is increased.

In addition, later generations of spurious products will be suppressed more effectively, since each precursor generation is suppressed in turn. Hence, the  $m/z$  102 ion formed from *o*-cresol, itself a spurious product, displayed the greatest suppression in Figure IV.6.b.

## APPENDIX D

CALCULATION OF THE BENZALDEHYDE CONCENTRATION AFTER 23.2 HRS OF  
IRRADIATION IN THE RESERVOIR

Cutting out and weighing the m/z 92 peaks from mass spectra recorded before the black lights were turned on and after 11.3 hr of irradiation indicated 55% (dilution corrected) of the toluene had been consumed. At the same rate of exponential decay for the toluene concentration, 71% would be consumed after 23.3 hr. This estimate agrees well with observations of O'Brien et al. (19) that 60-80% of the toluene is consumed after irradiation for 24-30 hr. The rate of disappearance of toluene is given by the following rate equation:

$$d[\text{tol}]/dt = k_{\text{tol}}[\text{OH}][\text{tol}] \quad (38)$$

Leone et al. found the OH concentration in the reservoir to be reasonably constant during the irradiation (9). Assuming a steady state concentration of OH radicals, let:

$$k' = k_{\text{tol}}[\text{OH}]_{\text{ss}} \quad (39)$$

Substituting  $k'$  for  $k_{\text{tol}}[\text{OH}]_{\text{ss}}$  in equation 38 and integrating:

$$[\text{tol}] = [\text{tol}]_0 e^{-k't} \quad (40)$$

$$k' = \ln([\text{tol}]_0/[\text{tol}])/t \quad (41)$$

For 71% consumption of  $[\text{tol}]_0$  after 23.2 hr,  $k' = 1.5 \times 10^{-5}/\text{sec}$ .

The net rate of production of benzaldehyde in the flask is given by:

$$d[\text{benz}]/dt = Yk'[\text{tol}] - k''[\text{benz}] \quad (42)$$

where  $k'' = k_{\text{benz}}[\text{OH}]_{\text{ss}}$  and  $Y$  (0.073) is the yield of benzaldehyde from toluene (72). Substituting for  $[\text{tol}]$  in equation 40 into equation 42:

$$d[\text{benz}]/dt = Yk'[\text{tol}]_0 e^{-k't} - k''[\text{benz}] \quad (43)$$

Integrating (73):

$$[\text{benz}] = Yk'[\text{tol}]_0 / (k'' - k') \times (e^{-k't} - e^{-k''t}) \quad (44)$$

In Table C.1,  $k_{\text{benz}} = 2.0 k_{\text{tol}}$  at room temperature; thus,  $k'' = 2.0 k'$  and:

$$[\text{benz}] = Yk'[\text{tol}]_0 / (1.0k') \times (e^{-k't} - e^{-2.0k't}) \quad (45)$$

$$[\text{benz}] = Y[\text{tol}]_0 \times (e^{-k't} - e^{-2.0k't}) \quad (46)$$

After 23.2 hr,  $[\text{benz}] = 0.15$  ppm.

BIBLIOGRAPHY

- (1) Hidy, G.M.; Mueller, P.K.; Grosjean, D.; Appel, B.R.; Wesolowski, J.J., Eds.; In The Character and Origins of Smog Aerosols; John Wiley: New York, 1980.
- (2) Changing Climate; Nat'l. Research Council Climate Research Committee; Nat'l. Academy Press: Washington, D.C., 1982.
- (3) Johnson, R.W.; Gordon, G.E., Eds. The Chemistry of Acid Rain; ACS: Washington, D.C., 1987.
- (4) Atmospheric Ozone; World Meteorol. Organ. Rep. No. 16; World Meteorological Organization: Geneva, 1985.
- (5) Atkinson, R.; Lloyd, A.C. J. Phys. Chem. Ref. Data 1984, 13, 315-444.
- (6) Atkinson, R.; Carter, W.P.L.; Darnall, K.R.; Winer, A.M.; Pitts, Jr., J.N. Int. J. Chem. Kinet. 1980, 12, 779-836.
- (7) Killus, J.P.; Whitten, G.Z. Atmos. Environ. 1982, 16, 1973-1988.
- (8) Leone, J.A.; Seinfeld, J.H. Int. J. Chem. Kinet. 1984, 16, 159-193.
- (9) Leone, J.A.; Flagan, R.C.; Grosjean, D.; Seinfeld, J.H. Int. J. Chem. Kinet. 1985, 17, 177-216.
- (10) O'Brien, R.J.; Green, P.J.; Doty, R.A.; Vanderzanden, J.W.; Easton, R.R.; Irwin, R.P. In Chemical and Biological Implications of Nitrogenous Air Pollutants; Grosjean, D., Ed.; Ann Arbor Science: Ann Arbor, MI, 1979; pp 189-210.
- (11) Grosjean, D.; Fung, K. JAPCA 1984, 34, 537-543.

- (12) Lonneman, W.A.; Kopczynski, S.L.; Darley, P.E.; Sutterfield, F.D.  
Environ. Sci. Technol. 1974, 8, 229-236.
- (13) Besemer A.C. Atmos. Environ. 1982, 16, 1599-1602.
- (14) Shepson, P.B.; Edney, E.O.; Corse, E.W. J. Phys. Chem. 1984, 88,  
4122-4126.
- (15) Bandow, H.; Washida, N.; Akimoto, H. Bull. Chem. Soc. Jpn. 1985,  
58, 2531-2540.
- (16) O'Brien, R.J.; Green, P.J.; Nguyen, N.L.; Doty, R.A.; Dumdei, B.E.  
Environ. Sci. Technol. 1983, 17, 183-186.
- (17) Kenley, R.A.; Davenport, J.E.; Hendry, D.G. J. Phys. Chem. 1981,  
85, 2740-2746.
- (18) Fung, K.; Grosjean, D. Anal. Chem. 1981, 53, 168-171.
- (19) O'Brien, R.J.; Dumdei, B.E.; Hummel S.V.; Yost, R.A. Anal. Chem.  
1984, 56, 1329-1335.
- (20) Tuazon, E.C.; MacLeod, H.; Atkinson, R.; Carter, W.P.L.  
Environ. Sci. & Tech. 1986, 20, 383-387.
- (21) Tuazon, E.C.; Atkinson, R.; MacLeod, H.; Biermann, H.W.;  
Winer, A.M.; Carter, W.P.L.; Pitts, Jr., J.N. Environ. Sci. & Tech.  
1984, 18, 981-984.
- (22) Plum, C.N.; Sanhueza, E.; Atkinson, R.; Carter, W.P.L.;  
Pitts, Jr., J.N. Environ. Sci. & Tech. 1983, 17, 479-484.
- (23) Dumdei, B.E.; O'Brien, R.J. Nature 1984, 311, 248-250.
- (24) Lane, D.A.; Thomson, B.A.; Lovett, A.M.; Reid, N.M. Adv. Mass  
Spectrom., Vol. 8B; Heyden: London, 1980; pp 1480-1489.

- (25) Reid, N.M.; French, J.B.; Buckley, J.A.; Lane, D.A.; Lovett, A.M.; Rosenblatt, G. In Proceedings, 4th Joint Conference on Sensing Environmental Pollutants; ACS: Washington, D.C., 1978; pp 594-600.
- (26) McKeown, M.; Siegel, M.W. Amer. Lab. Nov., 1975, 89-99.
- (27) Mitchum, R.K.; Korfmacher, W.A. Anal. Chem. 1983, 55, 1485A-1499A.
- (28) Proctor, C.J.; Todd, J.F.J. Org. Mass Spectrom. 1983, 18, 509-516.
- (29) Horning, E.C.; Carroll, D.I.; Dzidic, I.; Haegele, K.D.; Horning, M.G.; Stillwell, R.N. In Adv. in Mass Spectrom. in Biochem. and Medicine, Vol. I; Frigerio A., Castagnoli, N., Eds.; Spectrum Publications: Holliswood, N.Y., 1976; pp 1-16.
- (30) Sakairi, M.; Kambara, H. Mass Spectrom. 1983, 31, 87-95.
- (31) Covey, T.R.; Lee, E.D.; Bruins, A.P.; Henion, J.D. Anal. Chem. 1986, 58, 1451A-1461A.
- (32) Good, A.; Durden, D.A.; Kebarle, P. J. Chem. Phys. 1970, 52, 212-221.
- (33) Sunner, J.; Nicol, G.; Kebarle, P.; Anal. Chem. (In Press).
- (34) Good, A.; Durden, D.A.; Kebarle, P. J. Chem. Phys. 1970, 52, 222-229.
- (35) Sunner, J.; Ikonomou, M.G.; Kebarle, P.; Anal. Chem. (In Press).
- (36) Kebarle, P.; Searles, S.K.; Zolla, A.; Scarborough, J.; Arshadi, M. JACS 1967, 89, 6393-6399.
- (37) Shahin, M.M. J. Chem. Phys. 1966, 45, 2600-2605.
- (38) Kambara, H.; Kanomata, I. Int. J. Mass Spectrom. & Ion Phys. 1977, 25, 129-136.
- (39) Yinon, J.; Boettger, H.G. Vacuum 1976, 26, 159-161.
- (40) Kambara, H.; Kanomata, I. Anal. Chem. 1977, 49, 270-275.

- (41) VG Analytical 7000E Instruction Manual, Section 6.8, 1984.
- (42) Carroll, D.I.; Dzidic, I.; Stillwell, R.N.; Haegele, K.D.;  
Horning, E.C. Anal. Chem. 1975, 47, 2369-2373.
- (43) Caldecourt, V.J.; Zakett, D.; Tou, J.C. Int. J. Mass Spectrom. Ion  
Phys. 1983, 49, 233-251.
- (44) Dzidic, I.; Carroll, D.I.; Stilwell, R.N.; Horning, E.C.  
Anal. Chem. 1976, 48, 1763-1768.
- (45) Futrell, J.H.; Wojcik, L.G. Rev. Sci. Instrum. 1971, 42, 244-251.
- (46) McLafferty, F.W. Interpretation of Mass Spectra, 3rd ed.;  
Univ. Sci. Books: Mill Valley, CA, 1980; pp 15-30.
- (47) Siegel, M.W.; Fite, W.L. J. Phys. Chem. 1976, 80, 2871-2881.
- (48) Kinter, M.T.; Bursey, M.M. J. Am. Chem. Soc. 1986, 108, 1797-1801.
- (49) Weast, R.C.; Ed. Handbook of Chemistry and Physics, 68th ed.;  
CRC Press: Boca Raton, Fla., 1987.
- (50) Woolsey, G.A.; Ijumba, N.M.; Farish, O.J. Phys. D: Appl. Phys.  
1986, 19, 2135-2146.
- (51) Douglas, N.G.; Falconer, I.S.; Lowke, J.J. J. Phys. D: Appl. Phys.  
1982, 15, 665-668.
- (52) Perry, R.A.; Atkinson, R.; Pitts, Jr., J.N. J. Phys. Chem. 1977,  
81, 296-304.
- (53) Kambara, H.; Mitsui, Y.; Kanomata, I. Anal. Chem. 1979, 51,  
1447-1452.
- (54) Besemer, A.C.; Nieboer, H. Atmos. Environ. 1985, 19, 507-513.
- (55) Shepson, P.B.; Kleindienst, T.E.; Edney, E.O.; Namie, G.R.;  
Pittman, J.H.; Cupitt, L.T.; Claxton, L.D. Environ. Sci. Technol.  
1985, 19, 249-255.

- (56) Yost, R.A.; Fetterolf, D.D. Mass Spectrom. Rev. 1983, 2, 1-45.
- (57) McDowall, M.A.; Merren, T.O.; Smith, D.C.; Swain, D. Amer. Lab. 1987, March, 75-88.
- (58) VG Analytical Ltd., Floats Rd., Wythenshawe, Manchester, England.
- (59) MSD Isotopes, Merck Frosst Canada Inc., Montreal.
- (60) Nojima, K.; Fukaya, K.; Fukui, S.; Kanno S. Chemosphere 1974, 5, 247-252.
- (61) Lovett, A.M.; Reid, N.M.; Buckley, J.A.; French, J.B.; Cameron, D.M. Biomed. Mass Spectrom. 1979, 6, 91-97.
- (62) Futrell, J.H.; Wojcik, L.G. Rev. Sci. Instrum. 1971, 42, 244-251.
- (63) Penning, F.M. Electrical Discharges In Gases; Macmillan: New York, 1957.
- (64) Hemenway, C.L.; Henry, R.W.; Caulton, M. Physical Electronics; John Wiley: New York, 1962; pp 168-200.
- (65) Thomas, D.; Talbert, W.L. USAEC Report IS-1012; Ames, Iowa; 1964.
- (66) Dushman, S. Scientific Foundations of Vacuum Technique, 2nd ed.; Lafferty, J.M., Ed.; John Wiley: New York, 1962; pp 80-117.
- (67) Rosen, R.T.; Hartman, T.G. Vestec Thermospray Newsletter 1987, 3, 1.
- (68) Sigmond, R.S. In Electrical Breakdown of Gases; Meek, J.M., Craggs, J.D., Eds.; John Wiley: New York, 1978, p 361.
- (69) Laidler, K.J. Chemical Kinetics, 2nd ed., McGraw-Hill: New York, 1965, p 1-30.
- (70) McDaniel, E.W. Collision Phenomena In Ionized Gases; John Wiley: New York, 1964; p 476.



- (71) DeMore, W.B.; Molina, M.J.; Watson, R.T.; Golden, D.M.;  
Hampson, R.F.; Kurylo, M.J.; Howard, C.J.; Ravishankara, A.R.  
Chemical Kinetics and Photochemical Data for Use in Stratospheric  
Modeling; Jet Propulsion Laboratory: Pasadena, CA, 1983.
- (72) Atkinson, R.; Carter, W.P.L.; Winer, A.M. J. Phys. Chem. 1983, 87,  
1605-1610.
- (73) Daniels, F.; Alberty, R.A. Physical Chemistry, 3rd ed.;  
John Wiley: New York, 1966; p 336.

## VITAE

Andrew H. Grange was born in Jersey City, New Jersey on December 15, 1946. Within a year his family moved to Livingston, N.J. where he attended public elementary school until the age of 9 years. Schooling through high school was completed (1964) in Washington Township near Pittsburgh, Pennsylvania.

Starting college at Juniata College in Huntingdon, Pa. in September, 1964, the author earned his B.S. degree in Chemistry in June, 1968.

After working at U.S. Steel's research facility in Monroeville, Pa. over the summer of 1968, A. Grange reluctantly joined the U.S. Army. Most of the following 2 years, 9 months, and 2 days was spent doing clinical bacteriology.

The author started graduate school at the University of Wisconsin in Madison in July, 1971. After 6 years of good academic progress A. Grange left graduate school to start a small business partnership in upstate New York. Dairy farming was interesting, often fun, but exhausting and not profitable. The author sold his interest in the farm in December, 1982 and headed west to the Oregon country.

Times were hard for the unemployed; those with an unorthodox past need not apply at all. Hence, in September, 1983, the author again started graduate school at Oregon Graduate Center with single-minded determination to earn a Ph.D. degree in about 4 years. In February, 1988, the author defended his dissertation.

A. Grange has accepted a position (to begin March 21, 1988) with Lockheed Engineering and Management Services Company as a Senior Scientist in the Environmental Chemistry Department in Las Vegas, Nevada. Lockheed performs analytical work and develops analytical methods under contract from the US EPA, which owns the facility. The work is funded by the Superfund Amendments and Reauthorization Act (SARA) and the Resource Conservation and Recovery Act (RCRA).

## CURRICULUM VITAE

Andrew H. Grange

Education and  
Employment

B.S. Chemistry, 1968, Juniata College, Huntingdon, PA.  
US Army, Clinical Bacteriology, 9/68 - 6/71.  
Graduate Studies, Analytical Chemistry, Univ. of  
Wisconsin - Madison, 7/71 - 9/77.  
Private Partnership, Dairy Farm, 10/77 - 1/83.  
Ph.D. Environmental Science, Oregon Graduate Center,  
Anticipated in first quarter of 1988.

Honors and  
Memberships

One of seven winners of the 1987 graduate student  
research in environmental science competition;  
invited to present the paper on Aug. 31 at the  
national ACS meeting.  
Elected president of Madison chapter of Alpha Chi  
Sigma (chemical fraternity).  
Member: Amer. Chem. Soc.; Amer. Soc. for Mass  
Spectrometry.

Research  
Experience

Analytical Chemistry: Instrument Design and  
Development, Atmospheric Pressure Ionization Mass  
Spectrometry, Multi-cathode Photoionization  
Chamber.  
Atmospheric Chemistry: Photooxidation of Aromatic  
Compounds.

Publications

"A Medium Resolution API Mass Spectrometer" - Review  
of **Scientific Instruments** (in press).  
"Discharge Suppression System for a Double Focusing,  
API Mass Spectrometer" - **Review of Scientific  
Instruments** (in press).  
"Differentiating Molecular, Cluster, and Fragment Ions  
in APIMS" - To be submitted to **Analytical  
Chemistry**, 1988.  
"Suppression of Spurious Product Formation in an API  
Source" - To be submitted to **Environ. Science and  
Technology**, 1988.  
"Separation of Photooxidation Products of Toluene by  
Medium Resolution APIMS" - To be submitted to  
**Rapid Communications in Mass Spectrom.**, 1988.

Presentations

- "A Medium Resolution API Mass Spectrometer" - Amer. Soc. for Mass Spectrom., Denver, 5/26/87.
- "Manipulation of API Source Operating Conditions to Simplify Mass Spectra, Maximize Sensitivity, and Differentiate Between Molecular, Cluster, and Fragment Ions" - NW regional ACS meeting, Bellingham, WA, 6/19/87.
- "Differentiating Molecular, Cluster, and Fragment Ions in APIMS" - National ACS meeting, New Orleans, LA, 8/31/87.
- "Separation of Photooxidation Products of Toluene by Medium Resolution APIMS" - To be presented at ASMS, San Francisco, June, 1988.